DOKUZ EYLÜL UNIVERSITY
GRADUATE SCHOOL OF NATURAL AND APPLIED SCIENCES

MATHEMATICAL MODELING OF A THERMALLY COUPLED FUEL CELL AND METAL HYDRIDE HYDROGEN STORAGE TANK SYSTEM

by
Sera Ayten ÇETİNKAYA

August, 2024
İZMİR

MATHEMATICAL MODELING OF A THERMALLY COUPLED FUEL CELL AND METAL HYDRIDE HYDROGEN STORAGE TANK SYSTEM

A Thesis Submitted to the
Graduate School of Natural and Applied Sciences of Dokuz Eylül University
In Partial Fulfillment of the Requirements for Master of Science in
Department of Mechanical Engineering, Thermodynamics Program

by
Sera Ayten ÇETİNKAYA

August, 2024
İZMİR

M.Sc THESIS EXAMINATION RESULT FORM

We have read the thesis entitled "**MATHEMATICAL MODELING OF A THERMALLY COUPLED FUEL CELL AND METAL HYDRIDE HYDROGEN STORAGE TANK SYSTEM**" completed by **SERA AYTEN ÇETİNKAYA** under supervision of **PROF.DR. CAN ÖZGÜR ÇOLPAN** and **ASSOC.PROF.DR. MEHMET AKİF EZAN** and we certify that in our opinion it is fully adequate, in scope and in quality, as a thesis for the degree of Master of Science.

Prof. Dr. Can Özgür ÇOLPAN	Assoc. Prof. Dr. Mehmet Akif EZAN
Supervisor	Supervisor
Prof. Dr. Aytunç EREK	Prof. Dr. Alpaslan TURGUT
Jury Member	Jury Member

Prof. Dr. Arif HEPBAŞLI

Jury Member

Prof. Dr. Okan FISTIKOGLU

Director

Graduate School of Natural and Applied Sciences

ACKNOWLEDGMENT

The author wishes to express deep gratitude to her supervisors Prof. Dr. Can Özgür ÇOLPAN and Assoc. Prof. Dr. Mehmet Akif EZAN for their invaluable supervision, advice, encouragement, support, and insight throughout the research process.

The author wishes to express her special thanks to Dr. Yağmur NALBANT ATAK, Dr. Süleyman Aykut KORKMAZ, and Assoc. Prof. Dr. Mustafa Umut KARAOĞLAN for their valuable contributions to this thesis.

The author acknowledges the support provided by the 2535 Program of the Scientific and Technological Research Council of Turkey (TUBITAK) with project number 220N405 for providing financial support during her M.Sc. study.

The author acknowledges the support provided by Dokuz Eylul University's Scientific Research Projects with the project number 2020.KB.MLT.012 and FBA-2023-2996 for providing financial support during her M.Sc. study.

The author wishes to express special thanks to her dear friends Cemil KUZU, Beyza DURSUN, and Tacettin DİŞLİ for their support during this thesis.

The author gratefully thanks her mother, Sema ÇETİNKAYA, her father, Osman ÇETİNKAYA, and her sister, Ela Naz ÇETİNKAYA, for their invaluable support and always being with her.

Sera Ayten ÇETİNKAYA

MATHEMATICAL MODELING OF A THERMALLY COUPLED FUEL CELL AND METAL HYDRIDE HYDROGEN STORAGE TANK SYSTEM

ABSTRACT

This study examines a metal hydride tank's (MH) behavior through passive and active thermal management methods. A detailed one-dimensional axis-symmetric mathematical model of the metal hydride tank was developed using MATLAB. After validating the absorption and desorption processes of the metal hydride model, the melting physics of the phase change material (PCM) was included in the model. In the first part of the thesis, PCM was wrapped on the external surface of the metal hydride tank to investigate passive thermal management during the absorption process. Parametric simulations were carried out to examine the variations in hydride weight fraction, tank temperature, PCM liquid fraction, and PCM melting rate under various design and operational conditions during the absorption process. The second part of the thesis investigates the thermal coupling of a fuel cell with a metal hydride tank to extend a vehicle's driving range. The objective is to evaluate the impact of active thermal management by transferring waste heat from the fuel cell to the tanks on analysis duration and tank performance. The integrated system model was developed in the MATLAB-Simulink environment and the power demand characteristics of the fuel cell were defined in the model. This study considers four scenarios: thermally coupled and decoupled fuel cell-MH tank integrated systems and systems with temperature and hydrogen flow controllers. Parametric analyses were conducted to evaluate the effects of tank geometries, ambient temperatures, and convective heat transfer coefficients on the tank temperatures and ranges of the vehicle. Compared to Scenario-1, it was observed that the analysis times for Scenarios 2, 3, and 4 increased by 16%, 126%, and 190%, respectively, and that the hydrogen flow controller had a more significant impact on the system's range than the exhaust air from the fuel cell.

Keywords: Hydrogen energy, hydrogen storage, metal hydride, fuel cell, thermal management

ISIL OLARAK BİRLEŞTİRİLMİŞ YAKIT PİLİ VE METAL HİDRİT HİDROJEN DEPOLAMA TANKI SİSTEMİNİN MATEMATİKSEL MODELLENMESİ

ÖZ

Bu çalışma, metal hidrür tankının pasif ve aktif termal yönetim metotlarını incelemek için iki yaklaşım kullanmaktadır. Metal hidrür tankının detaylı bir eksenel simetrik matematiksel modeli MATLAB kullanılarak geliştirilmiştir. Metal hidrür modelinin absorbsiyon ve desorpsiyon süreçleri doğrulandıktan sonra, faz değişim malzemesinin (FDM) erime fiziği modele dahil edilmiştir. Tezin ilk bölümünde, absorpsiyon süreci sırasında pasif termal yönetimi incelemek için FDM, metal hidrür tankının dış yüzeyine sarılmıştır. Absorpsiyon süreci sırasında hidrür ağırlık oranı, tank sıcaklığı, FDM sıvı oranı ve FDM erime hızındaki değişiklikleri incelemek için parametrik simülasyonlar gerçekleştirilmiştir. Tezin ikinci bölümü, bir aracın menzilini uzatmak için yakıt hücresinin bir metal hidrür tankı ile termal olarak birleştirilmesini incelemektedir. Amacı, yakıt hücresinden tanka atık ısının transfer edilmesiyle aktif termal yönetimin etkisini analiz süresi ve tank performansı üzerinde değerlendirmektir. Entegre sistem modeli MATLAB-Simulink ortamında geliştirilmiş olup, yakıt hücresinin güç talep karakteristikleri modele dahil edilmiştir. Bu çalışmada dört senaryo ele alınmıştır: termal olarak bağlı ve bağımsız MH tankı/yakıt hücresi entegre sistemleri ile sıcaklık ve hidrojen akış kontrolcüsüne sahip sistemler. Tank geometrilerinin, çevre sıcaklıklarının ve taşınım ısı transfer katsayılarının tank sıcaklıkları ve aracın menzilleri üzerindeki etkilerini değerlendirmek için parametrik analizler yapılmıştır. Senaryo-1 ile karşılaştırıldığında sırasıyla Senaryo-2, 3 ve 4'ün analiz sürelerinde %16, %126 ve %190'lık bir artış olduğu ve hidrojen akış kontrolcüsünün, sistemin menzili üzerinde yakıt hücresinin atık ısısından daha önemli bir etkiye sahip olduğu gözlemlenmiştir.

Anahtar Kelimeler: Hidrojen enerjisi, hidrojen depolama, metal hidrür, yakıt pili, termal yönetim

CONTENTS

Page

M.Sc THESIS EXAMINATION RESULT FORM ii
ACKNOWLEDGMENT iii
ABSTRACT iv
ÖZ v
CONTENTS vi
LIST OF FIGURES viii
LIST OF TABLES xiii

CHAPTER ONE - INTRODUCTION 1

1.1. Introduction 1
1.2. Motivation 3
1.3. Objectives 3
1.4. Outline of the Thesis 4

CHAPTER TWO - BACKGROUND AND LITERATURE SURVEY 6

2.1. Introduction to the Hydrogen Storage and Metal Hydrides 6
2.2. Introduction to the Fuel Cells 9
2.3. Literature Survey 12
2.3.1. Passive Thermal Management 12
2.3.2. Active Thermal Management 13
2.3.3. Thermal Coupling of MH Tanks and PEM Fuel Cells during the Discharge Process 16

CHAPTER THREE - METHODOLOGY 22

3.1. Overview of the Methodology 22
3.2. Governing Equations for Mathematical Models 24
3.2.1. Model Reductions and Assumptions 24
3.2.2. Solution Method 25
3.2.3. Modeling of Metal Hydride Hydrogen Storage Tank 25

3.2.4. Modeling of Phase Change Material 30
3.2.5. Modeling of PEM Fuel Cell Characteristics..... 33
3.2.6. Modeling of Fuel Cell Exhaust Air Temperature..... 35
3.2.7. Modeling of Temperature Controller 37
3.2.8. Modeling of Hydrogen Flow Rate Controller Algorithm..... 38
3.3. Model Verifications..... 39
3.3.1. Verification of Metal Hydride Absorption/Desorption Behaviour.. 40
3.3.2. Verification of Fuel Cell Exhaust Heat Characteristics..... 41

CHAPTER FOUR - RESULTS AND DISCUSSION 42

4.1. A Case Study: Stand-Alone MH/PCM Charging System..... 42
4.2. Investigation on Thermally Coupled FC-MH System 51
4.2.1. Investigation of Heat Transfer Coefficient for Different Cases 53
4.2.2. Investigation of Ambient Temperature for Different Cases..... 57
4.2.3. Effect of Number of Tanks on Driving Durations..... 61
4.2.4. Effect of Fuel Cell Exhaust Heat..... 63
4.2.5. Effect of PID Temperature Controller and Different Air Set Temperature..... 64
4.2.6. Comparisons of the Scenarios 67

CHAPTER FIVE - CONCLUSIONS 71

REFERENCES.....74

APPENDICES.....83

Appendix-1: Nomenclature..... 83

LIST OF FIGURES

Page

Figure 2.1 Energy densities and volumetric capacities for physical and chemical hydrogen storage methods (modified from Hassan, Ramadan, Saleh & Hissesl (2021)) 7
Figure 2.2 Schematic of the process of the metal hydride tank 8
Figure 2.3 Thermal management methods for the MH tanks 9
Figure 2.4 Schematic of the PEMFC 10
Figure 2.5 A typical energy flow diagram in a PEMFC (Modified from Bvumbe et al., (2016)) 11
Figure 2.6 Active thermal management between a PEM fuel cell and an MH tank using (a) fan, (b) heat transfer fluid (Modified from Nguyen & Shabani (2020)), and (c) fan and heat transfer fluid (Modified from Zhu, Ait-Amirat, N'Diaye & Djerdir (2019)) 17
Figure 3.1 (a) Scenario-1 without thermal coupling and controller, (b) Scenario-2 with thermal coupling and without controller, (c) Scenario-3 without thermal coupling and with controller, and (d) Scenario-4 with thermal coupling and controller 23
Figure 3.2 (a) Schematic of MH tank model, and (b) 3D view of the model **(**taken from Disli, Cetinkaya, Ezan & Colpan, 2023) 26
Figure 3.3 Simulink model for the gas and solid density in the MH tank 27
Figure 3.4 Simulink model for the kinetic reactions and equilibrium pressure 28
Figure 3.5 Simulink model for the energy balance equation 29
Figure 3.6 Overall Simulink model for the MH tank 30
Figure 3.7 (a) Schematic of PCM integrated MH tank model, and (b) 3D view of the model (taken from Disli et al., 2023) 31
Figure 3.8 Polarization curve of the H2000 PEM fuel cell (Horizon Educational-H2000, 2024) 33
Figure 3.9 Changes in hydrogen flow rate under system power of the H2000 PEM fuel cell (Horizon Educational-H2000, 2024) 34
Figure 3.10 Changes in system power under fuel cell current of the H2000 PEM Fuel Cell (Horizon Educational-H2000, 2024) 34

Figure 3.11 Change of excess air expelled from the cathode side of the fuel cell under power for fuel cell..... 37
Figure 3.12 (a) Temperature controller subsystem (1-Fuel cell exhaust heat model, 2-PID controller) and (b) PID controller subsystem..... 38
Figure 3.13 Flow chart for control algorithm for H_2 flow controller..... 39
Figure 3.14 Absorption model verification with Tong et al. (Tong et al., 2019) (a) temperature and (b) weight fraction 40
Figure 3.15. Desorption model verification with Tong et al. (2021) (a) tank temperature and (b) hydrogen mass in the hydride 40
Figure 3.16 Fuel cell temperature characteristic model verification with Cano et al. (2014)..... 41
Figure 4.1 Under the MH radius of 2.5 cm and an inlet pressure of 8 bar, the time-dependent (a) hydride weight fraction, (b) PCM liquid fraction, (c) MH temperature, and (d) PCM temperature at different PCM thicknesses and melting temperatures. 43
Figure 4.2 Under the MH radius of 2.5 cm and an inlet pressure of 12 bar, the time-dependent (a) hydride weight fraction, (b) PCM liquid fraction, (c) MH temperature, and (d) PCM temperature at different PCM thicknesses and melting temperatures 44
Figure 4.3 Under the MH radius of 5 cm and an inlet pressure of 12 bar, the time-dependent (a) hydride weight fraction, (b) PCM liquid fraction, (c) MH temperature, and (d) PCM temperature at different PCM thicknesses and melting temperatures 44
Figure 4.4 The percentage of hydrogen in the tank under different pressure and PCM thickness conditions for an MH radius of 2.5 cm..... 45
Figure 4.5 The percentage of hydrogen in the tank under different pressure and PCM thickness conditions for an MH radius of 5 cm..... 45
Figure 4.6 Under an 8 bar inlet pressure, the time-dependent changes in (a) tank temperature and its expanded view at different PCM thicknesses and melting temperatures, (b) hydride weight fraction, and (c) PCM liquid fraction..... 46

Figure 4.7 Under a 10 bar inlet pressure, the time-dependent changes in (a) tank temperature and its expanded view, (b) hydride weight fraction, and (c) PCM liquid fraction at different PCM thicknesses and melting temperatures. 47
Figure 4.8 Under a 12 bar inlet pressure, the time-dependent changes in (a) tank temperature and its expanded view, (b) hydride weight fraction, and (c) PCM liquid fraction at different PCM thicknesses and melting temperatures. 48
Figure 4.9 Under different pressure values, the changes in (a) hydride weight fraction and (b) PCM liquid fraction as a function of PCM melting temperature and PCM thickness 49
Figure 4.10 For the optimal PCM thickness and melting temperature values, the time-dependent changes in (a) weight fraction and (b) liquid fraction 50
Figure 4.11 The driving cycle's speed-time graph 52
Figure 4.12 Comparative power-time graph for the fuel cell and battery 53
Figure 4.13 Power-time graph for the fuel cell 53
Figure 4.14 Under fixed H_2 amount, 25°C ambient temperature, and different convection coefficients for Case-1 (a) MH tank temperatures and (b) tank pressure 54
Figure 4.15 Under fixed H_2 amount, 25°C ambient temperature, and different convection coefficients for Case-2 (a) MH tank temperatures and (b) tank pressure 54
Figure 4.16 Under fixed H_2 amount, 25°C ambient temperature, and different convection coefficients for Case-3 (a) MH tank temperatures and (b) tank pressure 55
Figure 4.17 Under fixed tank number, 25 °C ambient temperature, and different convection coefficients for Case-1 (a) MH tank temperatures and (b) tank pressure 56
Figure 4.18 Under fixed tank number, 25 °C ambient temperature, and different convection coefficients for Case-2 (a) MH tank temperatures and (b) tank pressure 56

Figure 4.19 Under fixed tank number, 25 °C ambient temperature, and different convection coefficients for Case-3 (a) MH tank temperatures and (b) tank pressure 56
Figure 4.20 Under fixed H_2 amount, different ambient temperatures, and 100 W/m^{2}K convection coefficient for Case-3 (a) MH tank temperatures and (b) tank pressure 57
Figure 4.21 Under fixed H_2 amount, different ambient temperatures, and 100 W/m^{2}K convection coefficient for Case-3 (a) MH tank temperatures and (b) tank pressure 58
Figure 4.22 Under fixed H_2 amount, different ambient temperatures, and 100 W/m^{2}K convection coefficient for Case-3 (a) MH tank temperatures and (b) tank pressure 58
Figure 4.23 Under fixed tank number (3 tanks), different ambient temperatures, and 100 W/m^{2}K convection coefficient for Case-1 (a) MH tank temperatures and (b) tank pressure 59
Figure 4.24 Under fixed tank number (3 tanks), different ambient temperatures, and 100 W/m^{2}K convection coefficient for Case-2 (a) MH tank temperatures and (b) tank pressure 59
Figure 4.25 Under fixed tank number (3 tanks), different ambient temperatures, and 100 W/m^{2}K convection coefficient for Case-3 (a) MH tank temperatures and (b) tank pressure 59
Figure 4.26 Under fixed tank number (3 tanks), different ambient temperatures, and a convection coefficient of 100 W/m^{2}K for Case-4 (a) MH tank temperatures and (a) tank pressure 60
Figure 4.27 Under fixed tank number (3 tanks), different ambient temperatures, and a convection coefficient of 100 W/m^{2}K for Case-5 (a) MH tank temperatures and (a) tank pressure 61
Figure 4.28 Driving duration under different tank numbers at Case-2 and 10 W/m^{2}K heat transfer coefficient 61
Figure 4.29 Driving duration under different tank numbers at Case-2 and 100 W/m^{2}K heat transfer coefficient 62

Figure 4.30 Driving duration under different tank numbers at Case-2 and 1000 W/m^{2}K heat transfer coefficient 62
Figure 4.31 Comparative results between Scenario-1 and Scenario-2 at 25°C ambient temperature and 9 tanks 63
Figure 4.32 Comparative results between Scenario-1 and Scenario-2 (a) MH tank temperatures and (b) tank pressures at 25°C ambient temperature and 9 tanks 64
Figure 4.33 Change of (a) MH tank temperature and (b) tank pressure under different air set temperatures at 25°C ambient temperature and 3 tank number 65
Figure 4.34 Change of (a) MH tank temperature and (b) tank pressure under different air set temperatures at 25°C ambient temperature and 12 tank number 65
Figure 4.35 Changes of fuel cell exhaust air temperature with temperature controller under different air set temperatures and 3 tank numbers at 25°C ambient temperature 66
Figure 4.36 Under PID controller at air set temperature of 50°C and 3 number of tanks, (a) fuel cell exhaust air temperature and (b) power required by the heater (T_{amb}=25°C) 66
Figure 4.37 Comparison of the amounts of hydrogen used by different scenarios 69
Figure 4.38 Comparison of driving durations of different scenarios 69
Figure 4.39 Comparison of driving durations for Sc-1, Sc-2, Sc-3, and Sc-4 70

LIST OF TABLES

Page

Table 2.1 The advantages and disadvantages of the thermal management methods . 15
Table 2.2 Thermal integration methods for fuel cell with MH tanks 20
Table 3.1 Thermophysical properties of MH Tank (Tong et al., 2019) 30
Table 3.2 Thermophysical properties of PCM (Tong et al., 2019) 33
Table 3.3 H2000 PEM fuel cell specifications (Horizon Educational-H2000, 2024) 34
Table 3.4 H1000-XP PEM fuel cell specifications (Horizon Educational-H1000XP, 2024) 41
Table 4.1 The design and operating parameters used for the analyses 42
Table 4.2 Optimization results for different MH radius and inlet pressures 49
Table 4.3 The values at the end of 3600 s for the optimum PCM thickness and PCM melting temperature 51
Table 4.4 Specification of the cases 52
Table 4.5 Operating parameters for different scenarios 67

CHAPTER ONE
INTRODUCTION

1.1. Introduction

In the face of environmental problems arising as a result of the increase in the use of fossil fuels due to advancing technology and the growing global population, governments are attempting to expand the use of renewable energy resources by enacting various legislation. The Paris Agreement, which came into force in 2016, has been accepted by many governments. The long-term goal of this agreement is to keep the global temperature ascending to 1.5°C over pre-industrial levels. The usage of renewable energy resources and clean energy carriers has expanded in the nations that have signed the treaty, and numerous new job possibilities have appeared in this sector. These countries have also established different legislation to reduce pollution generation.

In addition to having an adverse effect on the environment, emissions from burning fossil fuels seriously impair human health. Air and water resources polluted due to the use of fossil fuels cause respiratory disorders, chronic lung diseases, and high cancer risks in humans (Dincer & Ezan, 2023). Dincer & Ezan (2023) stated that this group was the most affected by the disease during the COVID-19 pandemic. Fossil fuel consumption has detrimental consequences on human health in addition to the environment. Within the framework of all these problems, renewable and low-emission energy sources and energy carriers have begun to attract attention in recent years. In this new and emerging sector, hydrogen has claimed its position by garnering interest due to its high gravimetric density and status as a clean energy carrier.

Hydrogen holds great potential for the future of clean energy. Produced with renewable energy sources and functioning as a zero-emission energy carrier, hydrogen emerges as an eco-friendly alternative. In pursuit of reducing carbon emissions from fossil fuel combustion, hydrogen plays an essential role in energy transportation and storage. As an energy carrier, hydrogen facilitates the transfer and transformation of energy from one source to another. For instance, energy generated from sustainable resources like solar and wind can be used to produce hydrogen, thereby stabilizing

energy supply fluctuations. Moreover, hydrogen combustion or its use in fuel cells produces only water vapor and minimizes environmental impacts.

Hydrogen has broad and diverse applications. Fuel cell vehicles stand out in the transportation sector with their long-range and rapid refueling capabilities. They offer significant advantages over fossil fuels, especially heavy-duty transport and long-distance travel. Hydrogen is extensively used in the chemical industry for the manufacturing of ammonia, metallurgical processes, and refineries. Also, hydrogen is considered an energy storage solution for electricity grids in the energy sector. Examples of hydrogen storage technologies that can be used to combine sustainable energy resources and enhance energy supply security are metal hydrides, compressed gas, and liquid hydrogen (Yue et al., 2021).

Hydrogen will play a crucial role in future energy systems due to its flexibility as an energy carrier and its environmentally friendly attributes. Hydrogen enhances the effective use of sustainable energy resources and can lessen the environmental impact of fossil fuels due to its diverse applications and forms of storage. Its contributions to ensuring energy supply security and establishing sustainable energy infrastructure highlight the importance of investments and research in hydrogen technologies as vital steps towards achieving a clean and sustainable energy future (Ishaq, Dıncer & Crawford, 2022).

In this thesis, a detailed mathematical model of the metal hydride hydrogen tank was first developed, and the charging performance was examined by performing parametric analyses under passive thermal management. Then, the fuel cell-metal hydride (FC-MH) tank integrated system was designed and mathematically modeled for use in vehicles, houses, or energy-requiring applications. In this system, the role of active management strategies was systematically examined by thermally coupling the metal hydride with the fuel cell to optimize the temperature variations of the tank during the discharge period.

1.2. Motivation

This thesis focuses on the mathematical modeling of the metal hydride tank to *(i)* examine its absorption and desorption behavior, *(ii)* analyze the transient behavior of the metal hydride tank under passive and active thermal management strategies, and *(iii)* establish a system design for integrated systems by thermally coupling it with a fuel cell. The principal motivations of the thesis are as follows.

- Studies in the literature show that liquids are mainly used as heat transfer fluids in thermally coupled FC-MH tank systems. This thesis fills the gaps in the literature regarding the use of air as a heat transfer fluid, specifically focusing on the use of fuel cell exhaust air as a heat transfer carrier.
- To adjust the metal hydride tank's temperature, both passive and active methods have been employed. Still, in systems where more than one tank is used, a controller has not been used to ensure that the tanks operate sequentially and thus ensure that the temperatures of all tanks do not change simultaneously. This thesis systematically investigates different control schemes and discusses the cons and pros.

1.3. Objectives

The main goal of the thesis is to develop a simplified mathematical model for usage in integrated systems by creating a Simulink model of a thermally coupled fuel cell-metal hydride tank system. A detailed one-dimensional (1D) mathematical sub-model of the MH has been created within the system model to analyze the conditions under which the metal hydride tank efficiently supplies the hydrogen flow required for the fuel cell to generate power under specific driving cycles.

A hydrogen flow controller is also designed to enable the tanks to operate sequentially and enhance the driving range of the integrated FC-MH system. The ultimate goal is to improve the operational range by ensuring tank temperatures decrease sequentially during operation. This facilitates increased temperatures in inactive tanks due to the controller's actions when one tank is active. Furthermore, the

absorption behavior of a stand-alone MH tank is also examined with and without passive thermal management strategies by incorporating a Phase Change Material (PCM) into the 1D metal hydride tank model.

Hydrogen weight fraction and PCM liquid fraction values were calculated for different values of PCM thickness (1 cm to 5 cm) and PCM melting temperature (27°C to 35°C) under different cases where MH radius (2.5, 3, 4, and 5 cm) and inlet pressure (8, 10, 12 bar) change. PCM thickness and melting temperature values have been optimized for cases where the weight fraction and liquid fraction are maximum for all cases. Parametric analyses were conducted to determine the boundary conditions of the FC-MH tank system by varying tank geometries, the number of tanks (3, 6, 9, 12), ambient temperature values (15°C to 45°C), convective heat transfer coefficients (10, 50, 100, 500, 1000, and 2000 W/m²K), and air set temperature values (50°C to 70°C).

1.4. Outline of the Thesis

In Chapter Two, general information about hydrogen storage methods, MH tanks, and fuel cells is provided. A detailed literature review is conducted on the active and passive management of MH tanks and the thermal management strategies of the integrated fuel cell-MH tank systems.

In Chapter Three, the mathematical models of the MH/PCM system and the FC-MH tank system are presented. The model development process and the assumptions used for each sub-system are elaborated. The accuracy and reliability of the models are evaluated by comparing them with existing models in the literature.

In Chapter Four, parametric analyses are conducted for the passive thermal management and absorption process of the MH/PCM tank system. The purpose of these analyses is to assess the MH tank's performance. The results demonstrate the behavior of the system under different operating conditions and highlight potential areas for improvement. After that, parametric and comparative analyses of the FC-MH tank system are conducted under different cases and scenarios. Assessing the functionality and interactions between the FC-MH system and its many components

is the aim of these analyses. The analysis results provide important insights for system optimization and integrated solutions.

In Chapter Five, the main findings and results of the study are summarized. The analyses conducted for the MH/PCM and FC-MH tank systems are discussed in terms of their impact on energy efficiency and application areas. Additionally, suggestions for future studies and developing these systems are provided.

CHAPTER TWO
BACKGROUND AND LITERATURE SURVEY

2.1. Introduction to the Hydrogen Storage and Metal Hydrides

Hydrogen is the lightest element in the universe, having the maximum gravimetric energy density. The production of hydrogen with zero emission via the use of hydrogen in fuel cells to produce energy with almost zero emissions has attracted the attention of many sectors. One of the biggest challenges of light, odorless, and easily ignitable hydrogen is its storage. Various hydrogen storage technologies are on the market. Well-known techniques include compressed gas storage (Woodfield Monde &Takano, 2008), cryo-compressed storage (Aceves et al., 2010), liquid hydrogen storage (Ahluwalia & Peng, 2008), storage in metal hydrides (MHs) (Ahluwalia, 2007; Raju & Kumar, 2011; Raju & Kumar, 2012; Lozano, Eigen, Keller, Dornheim & Bormann, 2009), physisorption in cryo-adsorbents (Ahluwalia & Peng, 2009; Bénard & Chahine, 2001; Kumar, Raju & Senthil Kumar, 2012), complex MHs (Johnson, Jorgensen & Dedrick, 2011; Ley, Meggouh & Moury, Peinecke & Felderhoff, 2015), and chemical storage (Galli, De Francesco, Monteleone, Oronzio & Pozio, 2010). Due to its quick filling and comparatively small weight, compressed gas hydrogen storage is increasingly favored in commercial fuel cell systems. Currently, the hydrogen storage pressure in high-pressure tanks used in fuel cell systems is mostly 35 or 70 MPa. Even though storing hydrogen in liquid or cryo-compressed form yields a higher density and is more compact than storing it as a pressurized gas, operating at extremely low temperatures (e.g., -253 ℃) is challenging (Valenti, 2016). Storing hydrogen in the solid state is more advantageous than compressed gas and liquid storage in terms of volumetric energy density. Since hydrogen is stored chemically in the solid-state state, the storage pressure is much lower (10-30 bar), which makes it more attractive than compressed gas storage in terms of safety. Storage of hydrogen with metal hydrides is the most widely used solid-state hydrogen storage method. Figure 2.1 shows the energy densities and volumetric capacities for chemical and physical hydrogen storage methods. A Comparison between the physical and chemical storage methods shows that chemical storage methods can store more hydrogen in the same volume. However, in chemical storage methods, hydrogen is stored chemically, and the endothermic or

exothermic nature of these reactions during charging and discharging requires thermal management to obtain hydrogen at the desired flow rate.

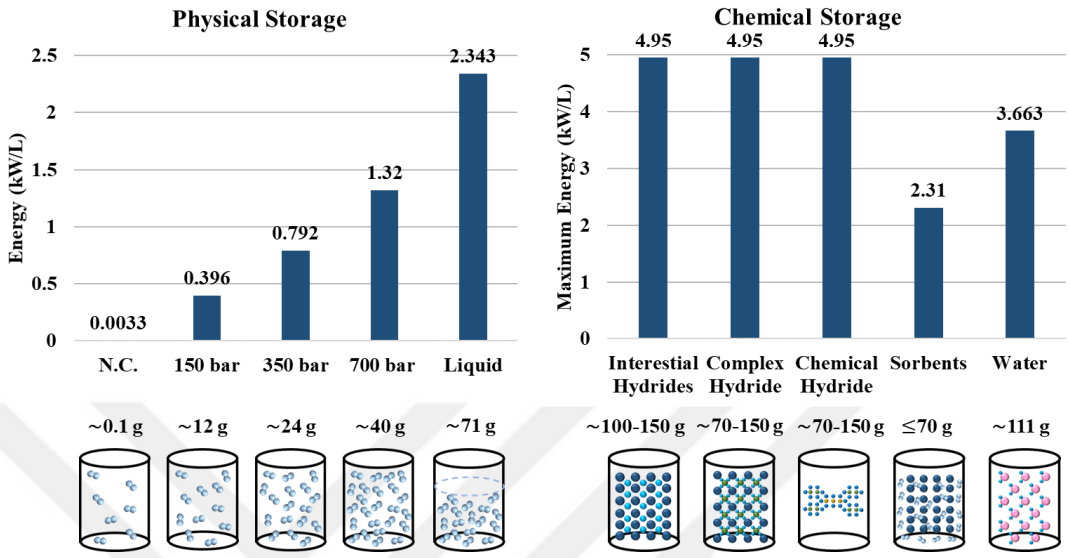

Figure 2.1 Energy densities and volumetric capacities for physical and chemical hydrogen storage methods (modified from Hassan, Ramadan, Saleh & Hissesl (2021))

Metal hydride tanks provide storage by taking advantage of the chemical properties of hydrogen. Hydrogen is bonded to the metal during hydrogen storage in the metal hydride tank (absorption). Heat is produced as a result of this exothermic process. The reverse of the process occurs when hydrogen is released from the metal hydride tank (desorption); this time, the reaction absorbs heat (Da Rosa & Ordóñez, 2021). The chemical reaction is given with the following Equation 2.1.

$$M + \frac{x}{2} H_2 \leftrightarrow MH_x + heat \tag{2.1}$$

As a result, temperature changes occur during the charging and discharging of the tank. The effect of temperature changes affects the hydrogen flow rate entering or leaving the tank, and thus, the duration of the charging or discharging process significantly depends on temperature variations. For this reason, thermal management in MH tanks is necessary for obtaining hydrogen at the desired flow rate and keeping

the charging/discharging in a short time. The schematic of the process between hydrogen, metal, and MH can be seen in Figure 2.2.

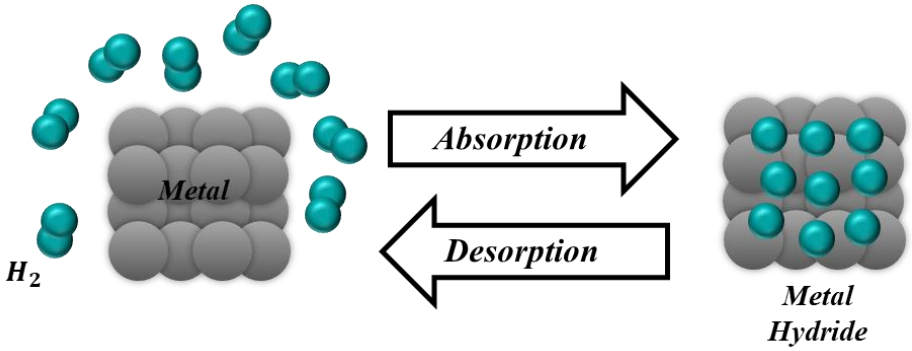

Figure 2.2 Schematic of the process of the metal hydride tank

Active and passive thermal management methods are the two basic categories into which metal hydride tank thermal management methods belong. In Figure 2.3, the main thermal management methods for the MH tanks are given. Fins, phase change materials (PCM), or high thermal conductivity materials can be added to the interior or exterior of the tank to manage temperature variations within the MH tanks passively. In contrast, active thermal management uses heat transfer fluids flowing through straight or helical pipes inside or outside the tank or utilizes exhaust gases from devices such as fuel cells (Cetinkaya, Disli, Soyturk, Kizilkan & Colpan 2022).

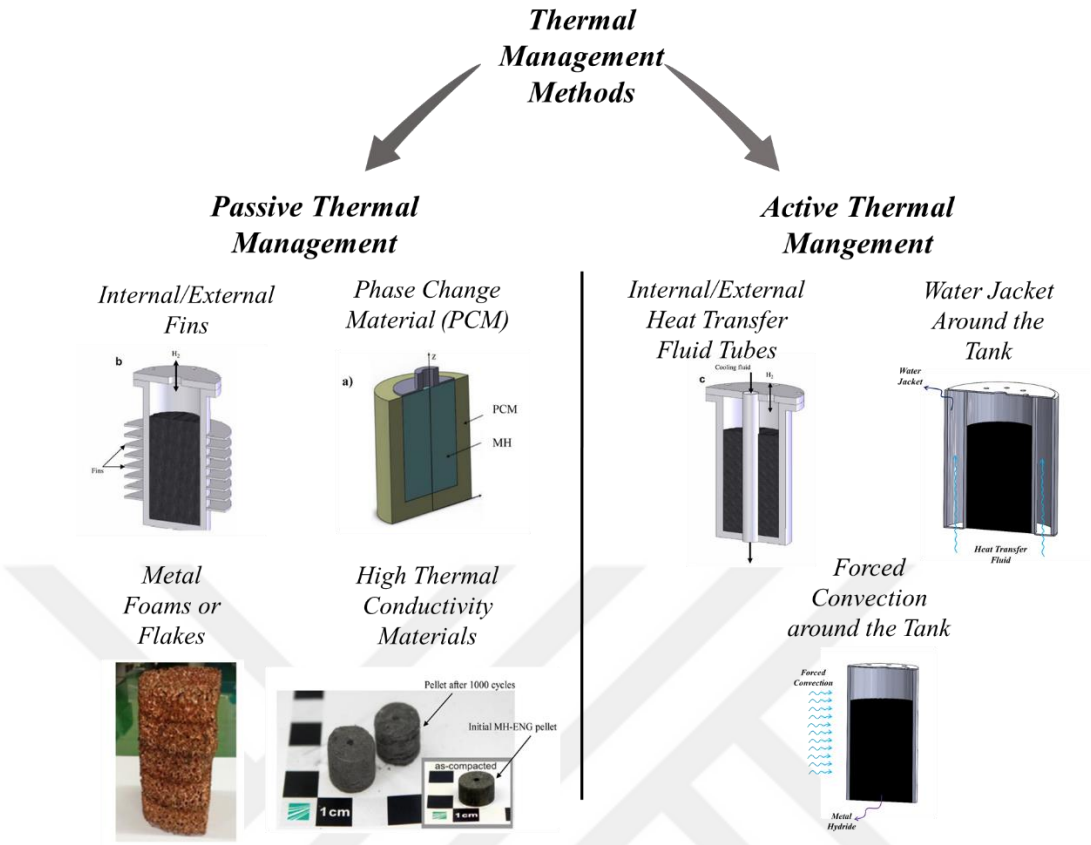

Figure 2.3 Thermal management methods for the MH tanks

2.2. Introduction to the Fuel Cells

Fuel cells are electrochemical energy conversion devices that generate electrical current with a low environmental effect and a high fuel cell efficiency through reduction and oxidation reactions. Depending on the electrolyte and fuel utilized, there are several distinct types of fuel cells, such as proton exchange membrane fuel cells (PEMFC), solid oxide fuel cells (SOFC), direct methanol fuel cells (DMFC), molten carbonate fuel cells (MCFC), Phosphoric Acid Fuel Cells (PAFC), and alkaline fuel cells (AFC) (Colpan, Nalbant & Ercelik, 2018). The most common type, PEMFC, typically uses hydrogen fuel and operates at low temperatures (60-80°C), making them suitable for portable electronics and vehicles. The PEM fuel cell stands out because it generates electricity with a higher energy density than other types. AFCs were among the first fuel cell types to be used, utilizing hydrogen and oxygen, and are often used in spacecraft; they are low-cost but sensitive to CO_2. SOFCs operate at high

temperatures (600-1000°C) and they can use a wide range of fuels (hydrogen, natural gas, biogas), making them ideal for large-scale power generation because of their high efficiency. MCFCs also work at high temperatures (600-700°C) and can use natural gas or biogas, which makes them suitable for large-scale applications like power plants. PAFCs operate at moderate temperatures (150-200°C) and are used for stationary power generation; they are durable and stable but have high initial costs. DMFCs use methanol and are typically suitable for portable electronic devices, similar to PEMFCs, but with the convenience of using liquid fuel. These types of fuel cells offer various advantages and disadvantages for different applications and fuel types, and the choice of which type to use depends on the specific requirements of the application and the type of fuel available (Colpan et al., 2018). The Anode, cathode, and overall chemical reactions are given in Equations (2.2), (2.3), and (2.4), respectively. Figure 2.4 displays the PEMFC schematic.

$$H_2 \rightarrow 2H^+ + +2e^- \tag{2.2}$$

$$^1/_2\, O_2 + 2H^+ + +2e^- \rightarrow H_2O \tag{2.3}$$

$$H_2 + {}^1/_2\, O_2 \rightarrow H_2O + Heat \tag{2.4}$$

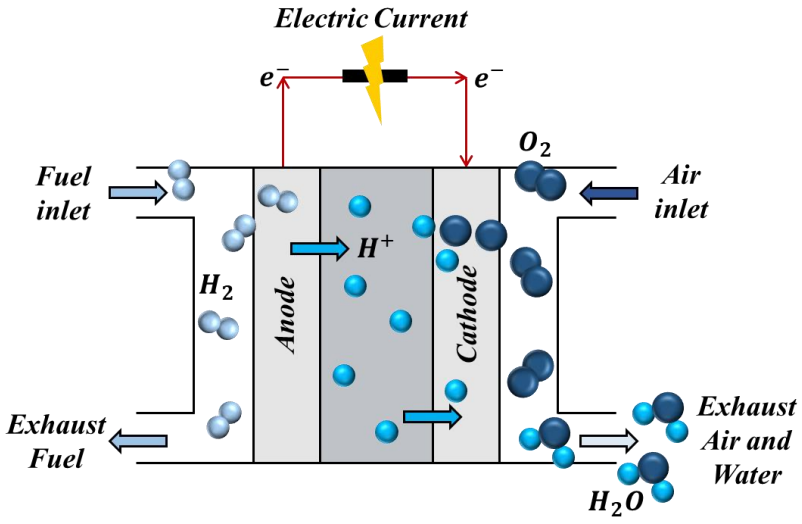

Figure 2.4 Schematic of the PEMFC

In FCs, heat is generated due to unavoidable entropy changes in the reaction and irreversibilities due to polarization. The heat generated can be found with the following equations considering the higher heating value (assumed that water is produced in liquid form), Equation (2.5), and lower heating value (assumed that water is produced in vapor form), Equation (2.6), of the hydrogen (Nguyen & Shabani 2020).

$$\dot{Q}_{HHV} = N_{cell} i_{cell} A_{cell} (1.48 - V_{cell}) \tag{2.5}$$

$$\dot{Q}_{LHV} = N_{cell} i_{cell} A_{cell} (1.25 - V_{cell}) \tag{2.6}$$

where N_{cell} is the number of cells, i_{cell} is the current density (A/cm^2), A_{cell} is the active area of the cell (cm^2) and V_{cell} is the output voltage of the cell (V). In order to keep the fuel cell operating properly and avoid damaging the membrane, the exhaust heat needs to be removed from the FC system. For this reason, different cooling systems such as edge cooling, air cooling, liquid cooling, or phase change cooling can be used. For small-size fuel cells (i.e., < 2 kW), simple cooling methods such as air cooling or heat pipes can be utilized. Liquid cooling methods are more suitable for PEMFCs with 5 kW and more power output (Nguyen & Shabani 2020). Approximately 30-40% of the heat generated by the FC is released as waste heat (Nguyen & Shabani 2021). An illustration of energy flow in a fuel cell is provided by the Sankey diagram in Figure 2.5 (Bvumbe et al., 2016; Shabani & Andrews, 2011).

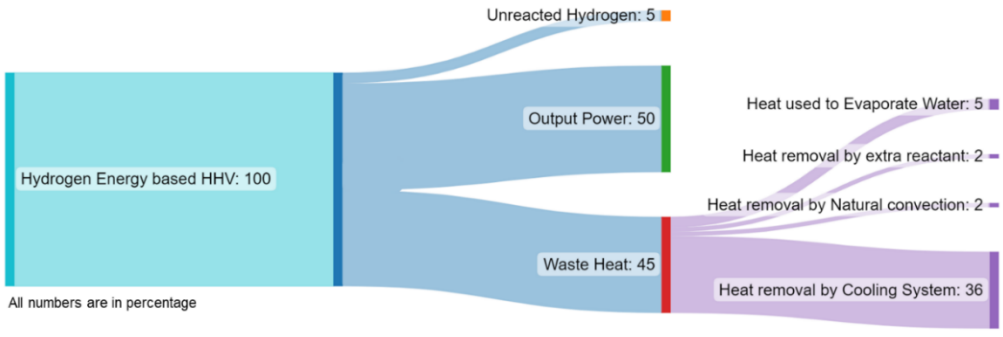

Figure 2.5 A typical energy flow diagram in a PEMFC (Modified from Bvumbe et al., (2016))

2.3. Literature Survey

In this section, the thermal management methods of MH tanks are explained to adjust the temperature changes in the tank due to the heat generated or absorbed during charging and discharging.

2.3.1. Passive Thermal Management

In passive thermal management, natural convection is the main heat transfer mechanism to adjust the tank's temperature. Different types of designs can be selected for MH tanks where natural convection is insufficient to increase heat transfer. By employing materials with high conductivity, fins can be added to the inner or outer surface of the MH tank, increasing heat transfer by expanding the heat transfer area. Fins can be integrated inside or outside the MH tank in different ways, such as horizontal (Bai, W.W. Yang, Zhang, F.S. Yang & Tang, 2020; Ferekh et al., 2015), longitudinal (Bai, W.W. Yang, Tang, Dai & F.S. Yang, 2022; Gupta & Sharma, 2021), tree-shaped (Bai et al., 2021), honeycomb (Afzal & Sharma, 2021; Corgnale, Hardy, Chahine & Cossement, 2018), or leaf-vein (Krishna, Pandey & Maiya, 2022). Nyamsi, Yang & Zhang (2012) optimized the analytical solution results they generated from a single fin by varying the fin thickness and radius to investigate the impact of fin structure on hydrogen storage. In order to validate the analytical work, they carried on to create a numerical model. As a result, they found that a 13% reduction in thermal resistance reduced charging time by 42%. Structures like flakes can be added to the fins to increase the surface area further. Singh, Maiya & Srinivasa Murthy (2017) experimented with the internal finned MH tank with and without cooper flakes to investigate the absorption effect of copper flakes. Consequently, they discovered that for the absorption capacity of 1.2 wt%, the copper flakes shortened the charging time by 11%.

The heat released from the reactions occurring in the Metal Hydride (MH) tank during absorption is stored by Phase Change Materials (PCMs), which help to prevent the tank from overheating. In the desorption process, PCMs provide the required heat to the tank. These characteristics make PCMs suitable for passive thermal management in MH tanks (Lewis & Chippar, 2021; Tong et al., 2021; Yao et al., 2020). El Mghari,

Huot & Xiao (2019) numerically investigated the absorption/desorption processes in an MH tank equipped with PCM. According to parametric studies, PCM thermal conductivity and latent heat significantly influence absorption and desorption rates. Alqahtani, Bamasag, Mellouli, Askri, and Phelan (2020) introduced a novel MH-PCM sandwich design that incorporates the MH tank with cascaded PCM beds. They examined heat transfer during the charging and discharging processes using PCMs with two different melting points. According to their research, the suggested MH-PCM sandwich design shortens charging and discharging times by 26% and 51%, respectively. Metal foams are also used to increase the thermal conductivity of MH tanks (El Mghari, Huot, Tong & Xiao, 2020; Ferekh et al., 2015). The impact of adding aluminum foam to metal hydride on mass and heat transport was examined numerically by Minko, Artemov & Yan'kov (2015). As a result, they observed that the aluminum foam accelerated mass and heat transfer. Compared to the condition without aluminum foam, they discovered that foam reduced the sorption time by half, but the volumetric capacity decreased by 9%. To improve thermal conductivity, high thermal conductivity materials can be added to metal powder, such as carbon or graphite. (Dieterich, Pohlmann, Bürger, Linder & Röntzsch, 2015). Nguyen & Shabani (2020) have explained more detailed information on this subject in their study. Zhu, Bao & Wu (2022) used expanded natural graphite (ENG) to increase heat transfer in the MH. As ENG decreases hydrogen density in compacted composites, they improve the ENG content to promote heat transfer for multilayer MH bed configurations. To improve the ENG distribution in the MH bed, they also proposed an optimization strategy based on the EDEP (Entransy Dissipation Extremum Principle). They then noticed that the use of ENG improved absorption. The EDEP-based optimized design outperformed a configuration with homogeneous ENG content in terms of the gravimetric exergy-output ratio by 15.33%, reaction time, and bed temperature dispersion consistency.

2.3.2. Active Thermal Management

Active thermal management, as opposed to passive thermal management, includes forced convection-based heat management methods. In active thermal management, heat exchanger systems can be integrated into the MH tank internally or externally.

Air or water can be utilized as cooling fluids to take out the heat that is released from the tank during the absorption process and replenish it with the heat needed for desorption. Several studies on active thermal management exist in the literature (Urunkar & Patil, 2020). Active thermal management can be achieved with a water jacket or coiled tubes integrated outside the MH tank or straight or spiral tubes running through the tank. Tong, Xiao, Yang, Bénard & Chahine (2019) investigated the thermal interaction in the MH tank by using different combinations of coiled tubes and straight pipes in their study. As a result, they found that the dual coiled-tube integrated heat exchanger effectively increased the MH tank's hydrogen storage efficiency. The tank temperature decreases more quickly during absorption, and the hydrogen storage time is reduced when an active thermal management method is used. Karmakar, Malik, Gupta & Sharma (2020) integrated a cooling tube inside the MH reactor and a water jacket on the outside. They experimentally investigated the amount of hydrogen stored for the following cases: *(i)* the system was only in natural convection, *(ii)* only the cooling tubes were active, and *(iii)* the cooling tubes and external water jacket were active together. Consequently, they noticed that the absorption and desorption performance were enhanced when the cooling tubes and an exterior water jacket were combined. Instead of using water as a heat transfer fluid, air is used in several papers published in the literature. Busqué, Torres, Grau, Roda & Husar (2017) compared natural and forced convection by using a fan in the experimental system they set up to investigate the absorption process of the MH tank and the effects of parameters. Therefore, the absorption rate constant, thermal conductivity, and activation energy are the main factors that influence absorption. An increase in porosity lowers the absorption rate, and the amount of hydrogen that is stored, but a faster absorption process necessitates a higher cooling level.

Several studies explore the thermal management of MH tanks by integrating active and passive methods (Tong et al., 2021; Pourpoint, Velagapudi, Mudawar, Zheng, & Fisher, 2010). Askri, Bensalah, Jemni, and Bennasrallah (2009) performed a mathematical analysis of the amount of time hydrogen could be stored in different configurations of MH tank models, such as a cylindrical tank, a cylindrical tank with fins on the outside, a cylindrical tank with a cooling fluid-filled concentric tube, and a cylindrical tank with fins on the concentric tube. Their results showed that utilizing a

cylindrical tank with a concentric tube fitted with fins resulted in a storage time that was almost 80% longer. Using active and passive management, Mellouli, Askri, Abhilash & Bennasrallah (2017) evaluated temperature variations mathematically when the absorption process in the MH tank over three distinct configurations that used only PCM (Case 1), PCM with straight tube (Case 2), and PCM with U-type tubes (Case 3). According to the results, the straight tube configuration used in Case 2 effectively removed 70% of the heat released during absorption from the system, resulting in a 94% reduction in storage time compared to Case 1. In Case 3, all the heat of the reaction was stored in the PCM, thus reducing the storage time by 72%. Using a water jacket and fins, Darzi, Afrouzi, Alizadeh, Shokri, and Farhadi (2017) examined the MH tank's temperature fluctuations during the absorption process. The effects of these parameters on the hydrogen filling amount were investigated using different temperatures, pressure, porosity, Reynolds number, and fin number. They concluded that the addition of a fin and water jacket greatly enhanced the absorption rate, whereas changes in supply pressure and temperature had little effect on it in the absence of a thermal management strategy. Afzal, N. Sharma, Gupta & P. Sharma (2022) designed a shell and tube-type reactor containing 7 MH tanks. They added 4 longitudinal fins in each MH tank. They investigated absorption and desorption processes under different operating parameters. The MH tank's performance was found to be promising for the absorption process when the supply pressure was raised to 35 bar. They claimed that raising the heat transfer fluid's temperature from 298 K to 308 K increased the desorption rate. In Table 2.1, the advantages and disadvantages of the thermal management of MHs are given.

Table 2.1 The advantages and disadvantages of the thermal management methods

Methods	Advantages	Disadvantages
Passive thermal management	✓ Simple to create ✓ Quiet operation as there are no mechanical parts ✓ Low costs	× Difficult to adjust the tank temperature to the required value × Poor heat removal capacity
Active thermal management	✓ Superior heat removal capacity ✓ Ability to adjust the tank temperature at the appropriate level regardless of the surroundings	× Requirement of more space as they contain mechanical components × The additional weight of the system components × High costs

2.3.3. Thermal Coupling of MH Tanks and PEM Fuel Cells during the Discharge Process

The waste heat produced by the fuel cell can be transferred to MH tanks via convection mechanisms to enhance the hydrogen desorption rate. As a result, while the fuel cell uses the hydrogen that the MH tank supplies to generate energy, the fuel cell's exhaust air may also be sent to the tank to give the necessary heating power. Using a fan or air blower, the fuel cell's exhaust air can be transported straight to the MH tank (see Figure 2.6a). MacDonald and Rowe (2006) studied three configurations (no heat transfer method, external fins around the MH tank, and annular MH tank design) to integrate the fuel cell for exhaust air removal mathematically. Their results showed that using fin and annular tube designs, MH tanks could efficiently provide the necessary hydrogen flow to the fuel cell. In contrast, configurations without thermal management methods were insufficient. Through experimental studies, Davids et al. (2016) thermally coupled a 130 W PEMFC and a 90 NL MH tank. They combined MH powder into a thermally expanded graphite, increased the heat transfer area of the MH tank by adding a fin, and used a fan to transport the exhaust air from the fuel cell to the MH tank to utilize the hydrogen in the tank to its fullest potential. As a result, when the fuel cell operated under 60, 100, and 120 W loads, it worked for 75, 41, and 35 minutes, respectively, and on average, more than 87% of the stored hydrogen was used at each load. Omrani, Nguyen & Shabani (2020) investigated experimentally the thermally coupled 2.5 kW open cathode PEMFC and nine 800 NL MH tanks. They tested if the MH tanks could supply the necessary hydrogen flow under various loads (500, 1000, 1500, and 2000 W) by sending the exhaust air from the PEMFC to the tanks. They concluded that, in the absence of thermal coupling between the fuel cell and the MH tank, the tanks can handle loads up to 500 kW without the need for thermal coupling. In additional studies, the fuel cell's exhaust air is directly used to accomplish thermal coupling between the fuel cell and the MH tank in the literature (Borzenka & Eronin, 2016; Liu et al., 2016).

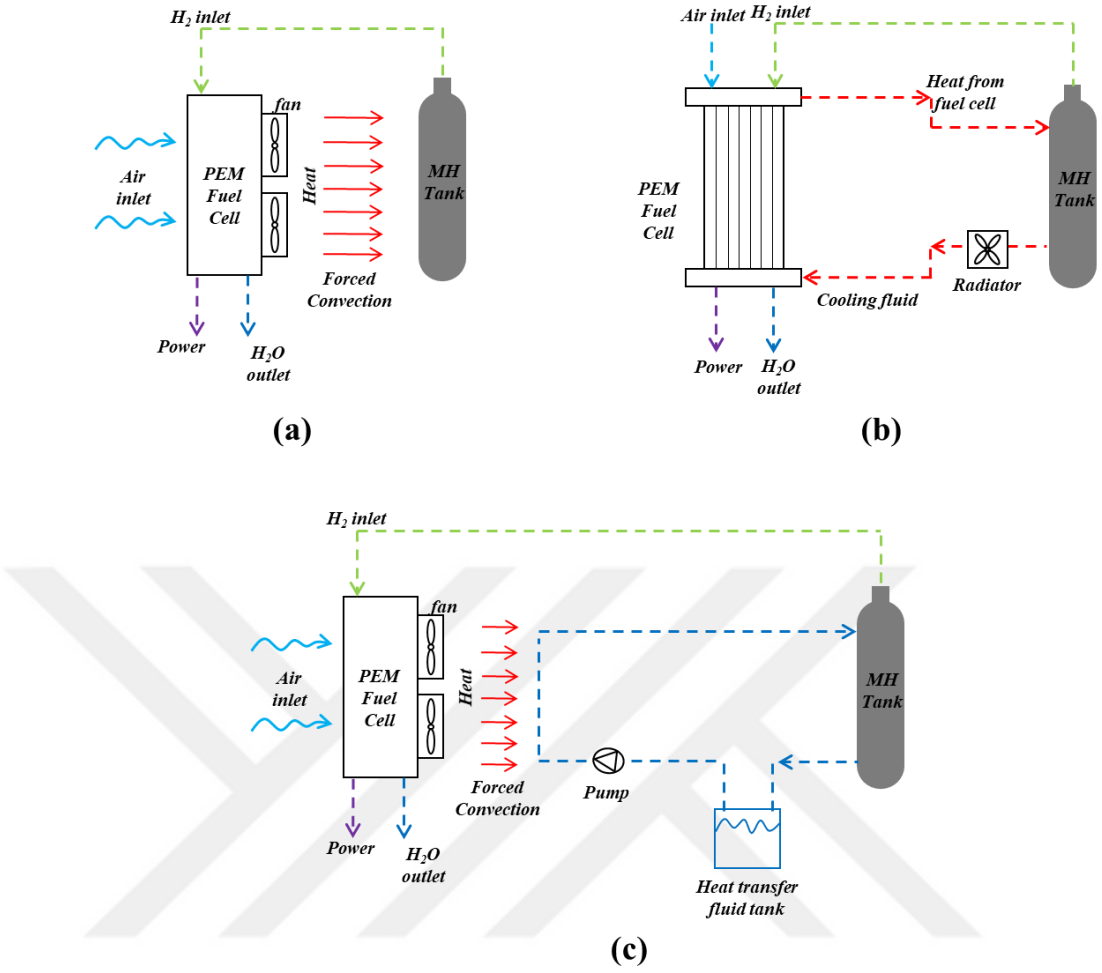

Figure 2.6 Active thermal management between a PEM fuel cell and an MH tank using (a) fan, (b) heat transfer fluid (Modified from Nguyen & Shabani (2020)), and (c) fan and heat transfer fluid (Modified from Zhu, Ait-Amirat, N'Diaye & Djerdir (2019))

In terms of their straightforward design and lightweight cooling components, air cooling systems are advantageous to liquid cooling systems. The disadvantage of air cooling systems is that they can remove less heat than liquid cooling systems because of the air's lower heat capacity. To complete the thermal coupling between the fuel cell and the MH tank, the system may also include a heat exchanger that uses the heat transfer fluid. The heat transfer fluid that receives the fuel cell's exhaust heat can be directed toward the MH tank to boost the flow rate of hydrogen during desorption. Urbanczyk et al. (2011) thermally coupled a high-temperature PEMFC and a sodium-alanate-based MH tank using heat transfer fluid. Evaluating the maximum hydrogen storage capacity in their studies, they produced three different tanks, analyzed them experimentally, and determined the best design. Chabane et al. (2019) proposed a

thermally coupled PEM fuel cell and MH tank using heat transfer fluid for use in vehicles. Consequently, they claimed that the fuel cell is unable to attain the operational temperature when the temperature needed for the hydrogen desorption of the MH tank is reached. The performance of a thermally connected MH with a 1.2 kW PEMFC was experimentally studied by Førde, Eriksen, Pettersen, Vie & Ulleberg (2011). As a result, they stated that the hydrogen flow required to obtain the desired flow from the fuel cell can be obtained by transmitting 25% of the cooling load of the fuel cell to the MH tank. The thermal coupling mechanism between the fuel cell and the MH tank for usage in transportation applications was mathematically investigated by Zhu et al. (2019). They transmitted the exhaust air from the fuel cell to the heat transfer fluid and the MH tanks using a thermal connection between the fuel cell and the tanks. They stated that the fuel cell system they developed had greater than 3% efficiency and greater than 10% fuel savings.

Some research employs passive thermal management techniques in addition to the fuel cell and MH tank's active coupling to transfer the fuel cell's exhaust air to the tank's interior. Tetuko, Shabani & Andrews (2016) mathematically combined 500 W PEMFC with MH tanks using heat pipes. At an ambient temperature of 25°C, the hydrogen flow rate supplied by MH tanks is 2.5 slpm, whereas the fuel cell needs a flow rate of 7.2 slpm to run at maximum power. They concluded that the MH tanks needed little less than 20% of the total cooling load of the stack at the highest power point to achieve the necessary 7.2 slpm hydrogen flow rate from the tanks at 35°C. Tetuko, Shabani, Omrani, Paul & Andrews (2018) thermally coupled a 130 W fuel cell and an 800 NL MH tank using a heat pipe experimentally and mathematically. They concluded that the fuel cell can run at 130 W, or 30% of its cooling load, using the 1.7 slpm hydrogen flow that the MH tank can provide.

Except for PEMFC, another type of fuel cell, SOFC, can be thermally coupled with an MH tank (Giap, Lee, Kim & Ahn, 2020; Delhomme et al., 2013). Yiotis, Kainourgiakis, Kosmidis, Charalambopoulou & Stubos (2014) investigated the thermal coupling potential between MH tank and SOFC based on the laws of thermodynamics. According to the results of their models, thermal coupling was found to be feasible for MHs with extremely high desorption enthalpies, which effectively

results in high fuel consumption rates in SOFC. In the work of Shao (2017), a system made up of a magnesium-based MH tank and a SOFC was examined using thermal analysis. They performed thermal coupling between the SOFC and MH tank by transferring exhaust heat from the SOFC to the tank. As a conclusion of thermal coupling, the system's electrical efficiency was 68.6%, and its thermal improvement was 13.4%. Table 2.2 lists the thermal management methods applied when the MH tank is employed in the fuel cell systems.

Table 2.2 Thermal integration methods for fuel cell with MH tanks

Investigator(s)	Fuel cell (FC)			Metal Hydride tank (MH)			Thermal integration method	Main objective of the study
	Type	Capacity	Cooling Subsystem	Hydride Bed Material	Capacity/ Volume	Cooling/Heating Subsystem		
McDonald & Rowe (2006)	PEMFC	1.2 kW	Air Cooling	AB_2 type MH	250 SL (~22 g hydrogen)	External fins and Annular tube	Active (Waste heat using fans)	To determine the MH design that provides the required hydrogen flow
Førde et al. (2009)	PEMFC	1.2 kW	Liquid cooling	$LaNi_5$	2900 NL (260 g hydrogen)	Internal fins with U-shape tubes	Active (Water circulation loop)	To improve the desorption rate and controlling the MH tank temperature
Urbanczyk et al. (2011)	HT-PEMFC	260 W	Liquid cooling	$NaAlH_4$	~	~	Active (Internal coiled tube with heat transfer fluid)	MH tank design that can charge/discharge the highest amount of hydrogen
Delhomme et al. (2013)	SOFC	1 kW	Air Cooling	MgH_2	1200 NL	~	Active (Waste steam circulation loop)	To improve the absorption/desorption rates and system efficiency
Tetuko et al. (2016)	PEMFC	500 W	Edge Cooling	$LaNi_5$	660 SL (~61 g hydrogen)	~	Passive (Waste heat using heat pipes)	To improve the hydrogen desorption rate
Davids et al. (2016)	PEMFC	130 W	Air Cooling	AB_2 type MH	90 NL	Internal fins and graphite	Active (Waste heat using fans)	To increase the desorption rate and the system efficiency
Borzenko et al. (2016)	PEMFC	2.5 Kw	Air Cooling	$La_{0.5}Nd_{0.5}Al_{0.1}Fe_{0.4}Co_{0.2}Ni_{4.3}$	~	~	Active (Waste heat using fans)	To improve the hydrogen desorption rate
Liu et al. (2016)	PEMFC	130 W	Air Cooling	$LaNi_5$	270 NL	~	Active (Waste heat using fans)	To improve the heat transfer integration
Gonzatti et al. (2016)	PEMFC	3 kW	Liquid cooling	$LaCeNi_5$	7000 L	Inner pipes	Active (Internal coiled tube with heat transfer fluid)	To improve the absorption/desorption rates and system efficiency

Shao (2017)	SOFC	~	Air Cooling	MgH_2	~	~	Active (Waste steam circulation loop)	To improve the system's electrical efficiency
Tetuko et al. (2018)	PEMFC	130 W	Edge Cooling	MmNiMnCo	800 NL (~72 g hydrogen)	~	Passive (Waste heat using heat pipes)	To improve the hydrogen desorption rate
Chabane et al. (2019)	PEMFC	500 W	Liquid cooling	FeTi	~	~	Active (Heat transfer liquid circulation loop)	To control the MH tank temperature and keep the fuel cell temperature at the operation temperature
Zhu et al. (2019)	PEMFC	1.1 kW	Air Cooling	unspecified	~	~	Active (Water circulation loop)	To improve and control the hydrogen flow rate
Kumar, Alam, Rakshit & Dutta (2019)	PEMFC	1 kW	Chiller cooling	$LaNi_5$	5000 L	External heating system	Active (Water circulation loop)	To improve the absorption/desorption rates and system efficiency
Omrani et al. (2020)	PEMFC	2.5 kW	Air Cooling	AB_5 type MH	800 NL (~79.2 g hydrogen)	~	Active (Waste heat using fans)	To improve the desorption rate and determine the optimum number of tanks
Giap et al. (2020)	SOFC	250 W	Liquid cooling	MgH_2	~	~	Active (Waste steam circulation loop)	To improve the absorption/desorption rates and system efficiency
Han et al. (2020)	PEMFC	50 W	Air cooling	AB_2 type MH	900 NL	~	Active (Waste heat using fans)	To improve the absorption/desorption rates and system efficiency

CHAPTER THREE
METHODOLOGY

3.1. Overview of the Methodology

The decrease in temperature of the metal hydride tank due to chemical reactions during the desorption process affects the charged/discharged hydrogen flow rate, making thermal management almost mandatory in system integration. In this thesis, firstly, the storage behavior of the stand-alone metal hydride tank under passive thermal management (using PCM) was examined as a case study, and secondly, the exhaust heat from the FC was supplied to MH tank to thermally couple these components in a system that was created.

For MH/PCM system, a mathematical model of a MH was developed, and a phase change material (PCM) model was incorporated, thereby forming the MH/PCM system. This model was designed to investigate the absorption characteristics of the tank under passive thermal management. Parametric analyses were conducted under various design and operating parameters. The study focused on identifying the conditions under which the MH tank performs optimally with passive thermal management. The best-case scenario for the hydride weight fraction was examined under optimal PCM thickness and melting temperature conditions.

For the FC-MH system, a detailed metal hydride tank model was developed to examine the performance of the MH tank in the system using different thermal management strategies. The system is tested for a small-scale hybrid fuel cell battery-powered vehicle. For a specific driving cycle, the power consumption of the vehicle is retrieved from the literature, and corresponding hydrogen demand, i.e., hydrogen flow rate, is determined from the datasheet of the fuel cell. The hydrogen demand of the fuel cell is supplied from the MH tank. Thermal coupling between the fuel cell and the metal hydride is achieved by directing the exhaust air from the fuel cell to the MH tanks. Four different scenarios were studied to examine the effect of thermal management on the temperature/pressure variations within the MH tank and the driving range: Scenario-1 (without thermal coupling and controller), Scenario-2 (with thermal coupling and without controller), Scenario-3 (without thermal coupling and

with controller), and Scenario-4 (with thermal coupling and controller). The schematics of the scenarios are illustrated in Figure 3.1.

In Scenario-1 (Figure 3.1a), hydrogen is supplied from the metal hydride tank to the fuel cell, and the FC and MH tanks are not thermally coupled. In Scenario-2 (Figure 3.1b), the exhaust air from the fuel cell is directed onto the MH tanks. In Scenario-3 (Figure 3.1c), a hydrogen flow controller that ensures the sequential operation of the tanks is designed. The effect of the hydrogen flow controller is examined in the case where the fuel cell and MH tank are not thermally coupled. Finally, in Scenario-4 (Figure 3.1d), the system where the fuel cell and MH tank are thermally coupled and the hydrogen flow controller is present is examined. For scenarios where the fuel cell and MH tank are thermally coupled, a temperature controller is designed to keep the temperature of the flow around the tanks constant, considering that an external heater is present in the system to maintain the predetermined temperature of the air discharged from the FC when the exhaust air from the fuel cell is insufficient. For Scenario-2 and Scenario-4, cases with and without the temperature controller are also examined.

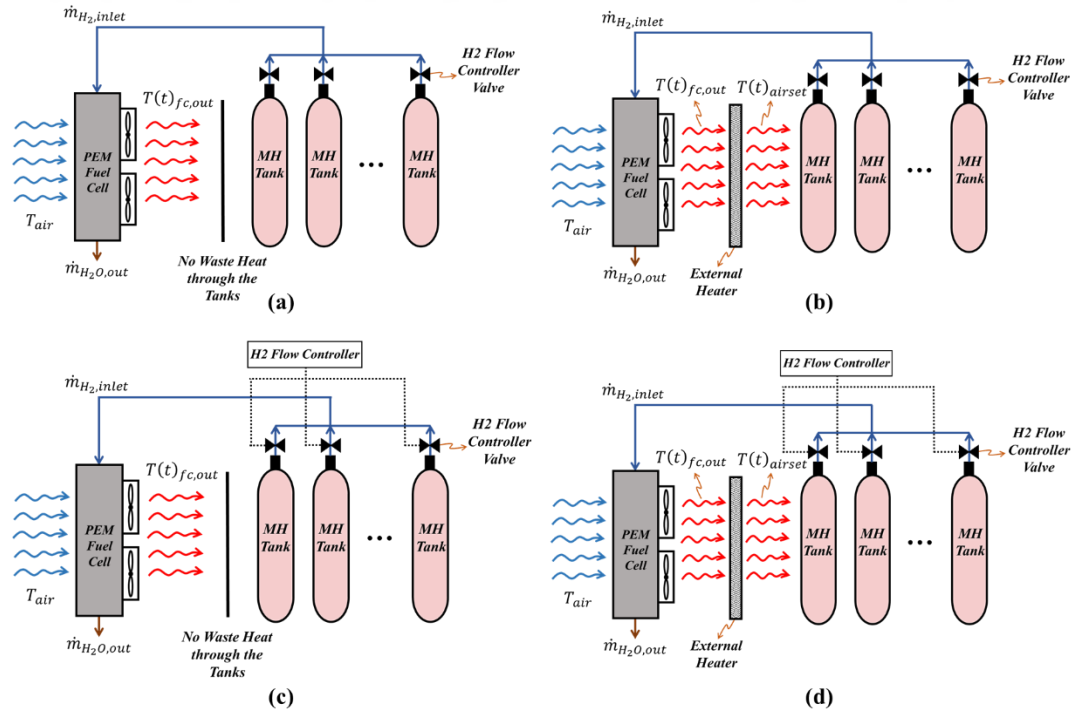

Figure 3.1 (a) Scenario-1 without thermal coupling and controller, (b) Scenario-2 with thermal coupling and without controller, (c) Scenario-3 without thermal coupling and with controller, and (d) Scenario-4 with thermal coupling and controller

This section explains in detail the mathematical models of the subsystems used in MH/PCM tank and FC-MH tank systems and the equations used for the models with the following subheadings. Finally, the validations of the models are given.

3.2. Governing Equations for Mathematical Models

In this section, model reductions and assumptions used for mathematical models are given, and the reduced governing equations of the models are provided.

3.2.1. Model Reductions and Assumptions

For the MH tank model, some simplifications were adopted according to the work of Ben Nasrallah & Jemni (1997). It is assumed that the hydrogen and metal are in thermal equilibrium, so a single energy equation represents the temperature variations within the tank. The spatial pressure variation within the tank was disregarded. In the PCT curve, the weight fraction change in the plateau region was considered constant. Thanks to the axis-symmetry nature of the 3D cylindrical tank, the geometry is reduced into a 1D axis-symmetric model. The following assumptions were also applied in the MH tank modeling (Disli et al., 2023; Ben Nasrallah & Jemni, 1997):

- The thermophysical properties of MH is constant.
- Radiation effects on the hydride bed are neglected.
- Hydrogen is treated as an ideal gas.
- Thermal equilibrium between the gas and solid phases in the hydride bed is valid.

The assumptions used for the MH/PCM model are given below.

- The thermophysical properties of PCM is constant.
- Heat conduction is considered in the PCM domain.

The assumptions used for the FC-MH integrated system are as follows;

- It is assumed that the fuel cell expels water in liquid form at its outlet, and the HHV (Higher Heating Value) is used to determine the exhaust heat of the fuel cell.
- In Scenario-1 and Scenario-2, analyses were conducted without thermal management between the MH tank and the fuel cell.
- It is assumed that the battery compensates for the load changes caused by the varying vehicle weight due to the changing number of tanks.
- The tank temperature is assumed to be a maximum of 65°C and a minimum of 5°C. When the tank temperature reaches these temperatures, the simulation is stopped (H2Planet, 2024).
- According to the safety conditions of the MH tank, a minimum hydrogen pressure of 0.5 bar must be supplied to the fuel cell (Horizon Educational-H2000, 2024). The tank stops supplying hydrogen for safety measures when the pressure drops below 0.5 bar.

3.2.2. Solution Method

For the MH/PCM tank model, a 1D axisymmetric model was developed in MATLAB software. An explicit scheme was used in the analysis with 0.01 seconds time step size. A total of 60 meshes were used: 20 for the MH domain and 40 for the PCM domain.

A 1D model was developed for the system-level model, which comprises MH tanks and a fuel cell, using MATLAB/Simulink software. In the Simulink model, 40 meshes were used for the MH domain. For Scenario-1 and Scenario-2, simulations were carried out using the ode3 (Bogacki-Shampine) method from MATLAB library with a time step size of 0.01 seconds. For Scenario-3 and Scenario-4, variable-step type and ode23t (Mod. Stiff/Trapezoidal) method from MATLAB library were used.

3.2.3. Modeling of Metal Hydride Hydrogen Storage Tank

A 1D axisymmetric mathematical model was established. Convection is defined on the lateral surface of the tank, and the bottom surface of the tank is assumed to be adiabatic. It is assumed that there is no contraction or expansion at the tank inlet, and

hydrogen is uniformly distributed in the tank. The schematic of the mathematical model of the metal hydride tank is given in Figure 3.2a, and the 3D view of the MH tank model is given in Figure 3.2b. The governing equations for MH model are given below.

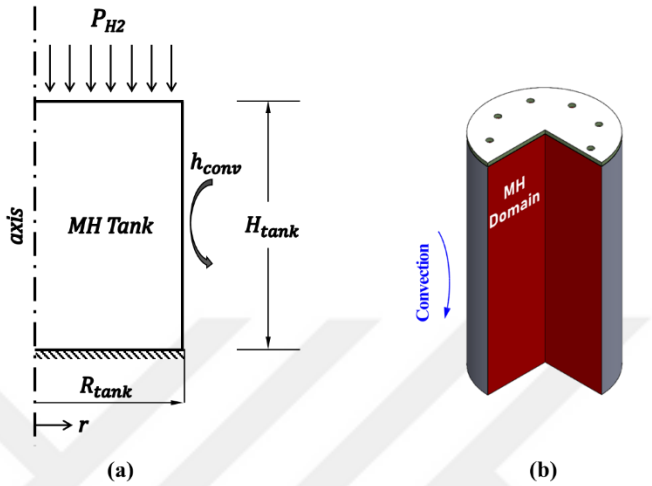

Figure 3.2 (a) Schematic of MH tank model, and (b) 3D view of the model (taken from Disli, Cetinkaya, Ezan & Colpan, 2023)

The hydrogen flow rate, which varies depending on the metal porosity used in the tank and the density of the metal and hydrogen, can be calculated from the mass balance between metal, hydrogen, and metal hydride as follows.

$$(1-\varepsilon)\frac{d\rho_{solid}}{dt} = \dot{m}'''_{H_2} \tag{3.1}$$

$$\varepsilon\frac{d\rho_{gas}}{dt} = -\dot{m}'''_{H_2} - \dot{m}'''_{out} \tag{3.2}$$

where ε is the porosity of the $LaNi_5$, ρ_{solid}, and ρ_{gas} are the density of metal and the hydrogen, respectively, $\dot{m}'''_{out}$ is the volumetric flow rate withdrawn from the tank. The Simulink model in which the gas and solid density in the tank is calculated using Equation (3.1) and Equation (3.2) is given in Figure 3.3.

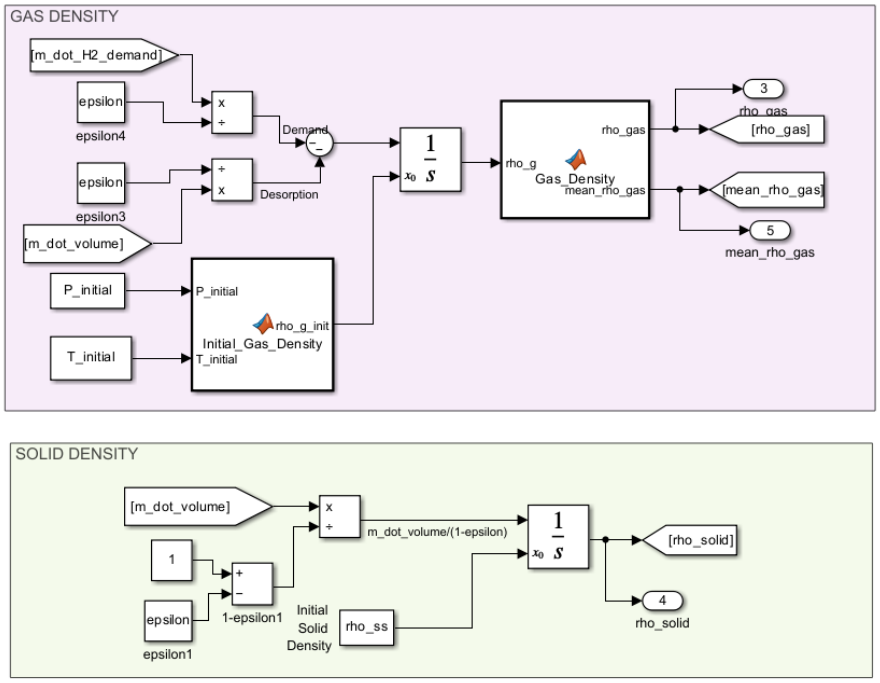

Figure 3.3 Simulink model for the gas and solid density in the MH tank

The flow rate of the hydrogen during the absorption (Eq. (3.3)) and desorption (Eq. (3.4)) process, $\dot{m}_{H_2}'''$, can be obtained from reaction kinetics as follows,

$$\dot{m}_{H_2}''' = C_a exp\left(-\frac{E_a}{RT}\right) ln\left(\frac{P}{P_{eq}}\right)[\rho_s^{sat} - \rho_s] \tag{3.3}$$

$$\dot{m}_{H_2}''' = C_d exp\left(-\frac{E_d}{RT}\right)\left(\frac{P_{eq} - P}{P_{eq}}\right)[\rho_s - \rho_{empty}] \tag{3.4}$$

where C_a and C_d are the time constant for the absorption and desorption process, respectively, E_a and E_d are the activation energy for the absorption and desorption process, respectively, R is the universal gas constant, T the MH tank temperature, P is the pressure inside the tank, ρ_s^{sat} is the saturated solid density, ρ_s is the solid density, ρ_{empty} is the density of empty tank. Equilibrium pressure is obtained by the Van't Hoff equation as follows.

$$P_{eq} = P_{ref} exp\left(A - \frac{B}{T}\right) \tag{3.5}$$

where P_{ref} is the reference pressure for the chemical reaction, A and B are the constants for the absorption and desorption process. The Simulink model of kinetic reactions in which the hydrogen flow rate is calculated using Equation (3.3) and Equation (3.4) and the Simulink model in which the equilibrium pressure is calculated using Equation (3.5) are given in Figure 3.4.

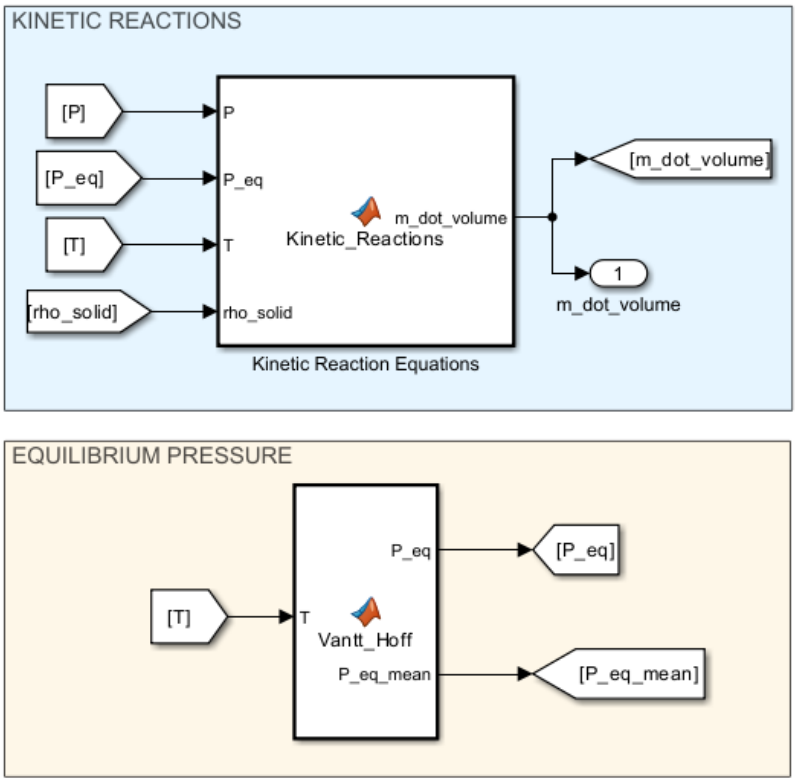

Figure 3.4 Simulink model for the kinetic reactions and equilibrium pressure

The temperature fluctuations inside the MH tank are calculated using the energy equation. The 1D energy balance equation is given as

$$(\rho c)_{eff}\frac{\partial T}{\partial t} = \frac{1}{r}\frac{\partial}{\partial r}\left[k_{eff} r \frac{\partial T}{\partial r}\right] + \dot{q}_{source} \tag{3.6}$$

where $(\rho c)_{eff}$ is the effective heat capacity, k_{eff} is the effective thermal conductivity and, $\dot{q}_{source}$ is the heat resulting from the chemical reaction. The heat can

be obtained depending on the enthalpy of formation, ΔH^0, of the chemical reaction as follows,

$$\dot{q}_{source} = \dot{m}'''_{H_2} \left[\Delta H^0 + T \left(c_{p_{gas}} - c_{p_{solid}} \right) \right] \tag{3.7}$$

where $c_{p_{gas}}$ and $c_{p_{solid}}$ are the specific heats of the gas and solid, respectively. The energy balance Simulink model created using Equation (3.6) and Equation (3.7) is given in Figure 3.5. The overall block view of the metal hydride tank Simulink model is given below in Figure 3.6. The thermophysical properties of the MH tank are given in the Table 3.1.

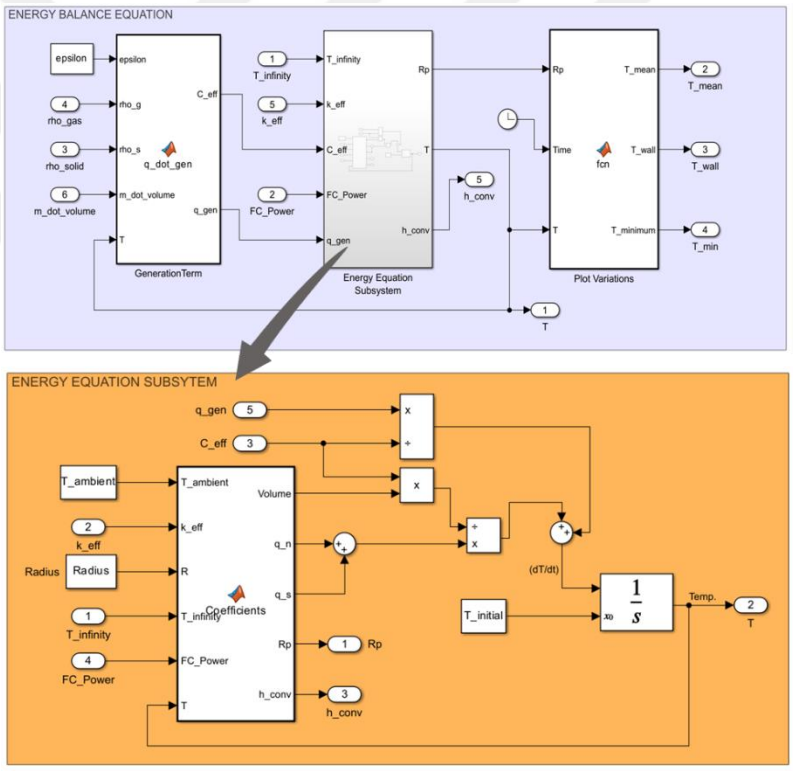

Figure 3.5 Simulink model for the energy balance equation

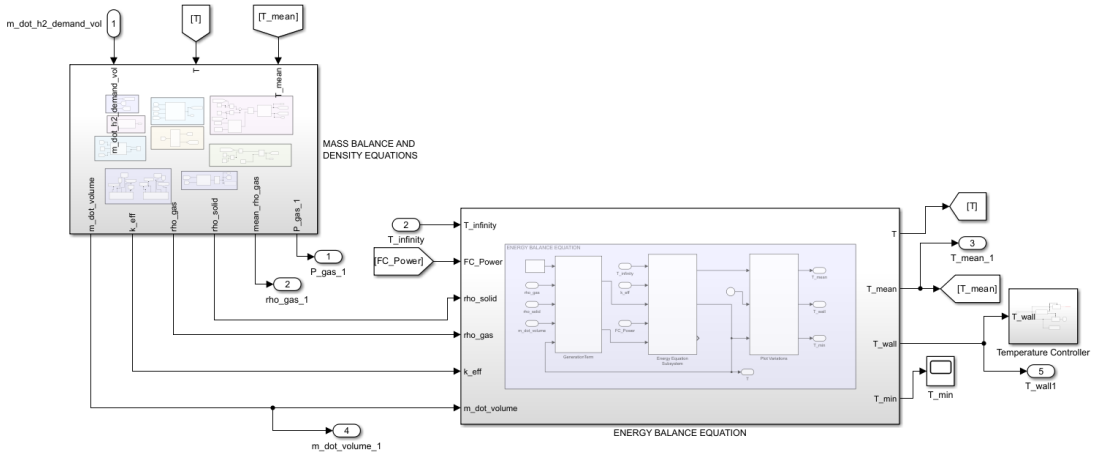

Figure 3.6 Overall Simulink model for the MH tank

Table 3.1 Thermophysical Properties of MH Tank (Tong et al., 2019)

Parameters	**Values**
Metal Density, ρ_s [kg m^{-3}]	7164
Saturated Density of MH, ρ_{ss} [kg m^{-3}]	7259
Heat Capacity of MH tank, $c_{p,MH}$ [J kg^{-1} K^{-1}]	419
Thermal Conductivity of MH tank, k_{MH} [W m^{-1} K^{-1}]	2.4
Activation Energy for Absorption, E_a [J mol^{-1}]	21,179.6
Activation Energy for Desorption, E_d [J mol^{-1}]	16,473
Reaction Constant for Absorption, C_a [1 s^{-1}]	59.187
Reaction Constant for Desorption, C_d [1 s^{-1}]	9.57
Porosity, ε [-]	0.5
Maximum Weight Fraction, $\%wt$	1.32
Enthalpy of Reaction, ΔH [J kg^{-1}]	1.537x10^{7}
Plateau Pressure Coefficient, A [-]	10.57
Plateau Pressure Coefficient, B [K]	3074.6
Operating Pressure, [bar]	10

3.2.4. Modeling of Phase Change Material

The PCM integrated model is developed by wrapping the PCM on the outer surface of the MH tank. The schematic of the PCM integrated model can be seen in Figure 3.3a, and the 3D view of the model is given in Figure 3.3b. The outer surface of the PCM is considered to be well-insulated. Parametric simulations based on the reference work of Tong et al. (2019) are used to test paraffin-type PCMs with varying melting temperatures.

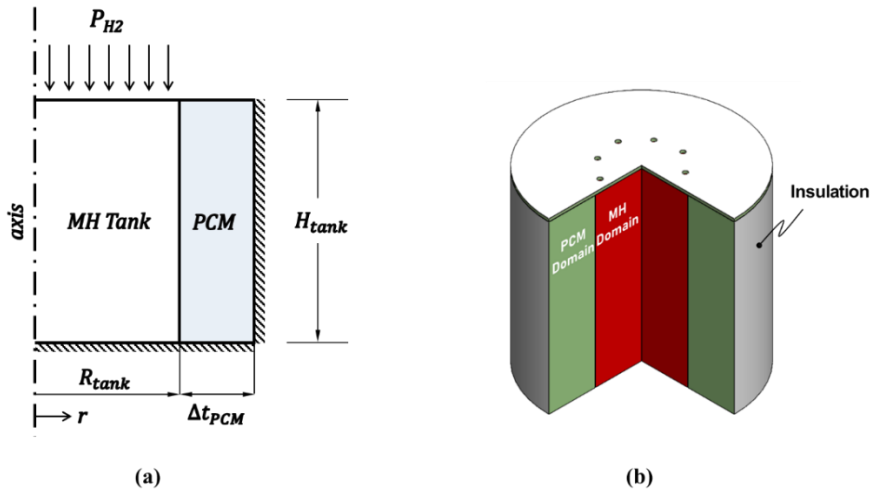

Figure 3.7 (a) Schematic of PCM integrated MH tank model, and (b) 3D view of the model (taken from Disli et al., 2023)

The temperature transforming method was used for PCM modeling. The general energy balance equation is given in Equation (3.8) on an enthalpy basis (Dincer and Ezan, 2018).

$$\frac{\partial H}{\partial t} = \frac{1}{r}\frac{\partial}{\partial r}\left(k_{en} r \frac{\partial T}{\partial r}\right) + \frac{\partial}{\partial x}\left[k_{en}\frac{\partial T}{\partial x}\right] - \frac{\partial S}{\partial t} \tag{3.8}$$

Equation (3.9) transforms the enthalpy equation into a temperature basis by assuming that the phase change process occurs in a specific temperature range. Hence, the current method considers three solid, liquid, and mushy phases. The governing equations for the PCM side are given below. After determining the temperature-enthalpy equations for all phases, the respective C and S coefficients for each region were found. Each PCM has different C and S coefficients, making their determination crucial for observing PCM behavior.

$$H(T) = C(T)T + S(T) \tag{3.9}$$

where C is the volumetric heat capacity, k_{en} is the enhanced thermal conductivity, and S is for the source term. C and S coefficients can be obtained using Equations (3.10) and (3.11);

$$C = C(T) = \begin{cases} C_s & T < T_m - \delta T_m & Solid\ Phase \\ C_m + \rho \dfrac{h_{sf}}{2\delta T_m} & T_m - \delta T_m \le T \le T_m + \delta T_m & Mushy\ Phase \\ C_l & T > T_m + \delta T_m & Liquid\ Phase \end{cases} \quad (3.10)$$

$$S = S(T)$$

$$\begin{cases} C_s(\delta T_m - T_m) & T < T_m - \delta T_m & Solid\ Phase \\ \left(C_m + \rho \dfrac{h_{sf}}{2\delta T_m}\right)(\delta T_m - T_m) & T_m - \delta T_m \le T \le T_m + \delta T_m & Mushy\ Phase \\ C_s \delta T_m - C_l T_m + \rho h_{sf} & T > T_m + \delta T_m & Liquid\ Phase \end{cases} \quad (3.11)$$

where T_m is the melting temperature, and δT_m is the mushy range. The thermal conductivity of the PCM is quite low. To accelerate the melting and freezing processes, it is necessary to enhance the thermal conductivity. Natural convection correlations within the cylindrical void of the MH tank have been used to increase the thermal conductivity of the liquid PCM. For this purpose, the ratio of the enhanced thermal conductivity, k_{en}, to the constant PCM conductivity is obtained using Nusselt correlations (Equation 3.12) (Cengel & Ghajar, 2015).

$$Nu = \frac{k_{en}}{k} = 0.386 \left(\frac{Pr}{0.861 + Pr}\right) \left(F_{cyl}\, Ra_L\right)^{\frac{1}{4}} \quad (3.12)$$

where Pr is the Prandtl number, Ra is the Rayleigh number, F_{cyl} is the correction factor. These can be obtained using Equations (3.13-3.15) (Cengel & Ghajar, 2015).

$$F_{cyl} = \frac{\left[ln\left(\frac{D_o}{D_i}\right)\right]^4}{L_c^3 \left(D_i^{-\frac{3}{5}} + D_o^{-\frac{3}{5}}\right)^5} \quad (3.13)$$

$$Ra_L = g\beta \frac{\Delta T L_c^3}{\vartheta \alpha} \quad (3.14)$$

$$Pr = \frac{\mu c_p}{k} \quad (3.15)$$

where D_o and D_i are the outer and inner diameters of the cylindrical geometry, L_c is the gap between the cylinders (characteristic length), g is the gravitational

acceleration [m/s²], β is the thermal expansion coefficient, ϑ is the kinematic viscosity, α is the thermal diffusivity, μ is the dynamic viscosity, c_p is the specific heat capacity, and k is the thermal conductivity. Thermophysical properties of the PCM are given in Table 3.2.

Table 3.2 Thermophysical properties of PCM (Tong et al., 2019)

Parameters	**Value**
PCM Density, ρ_{PCM} [kg m^{-3}]	880
Heat Capacity of PCM, $c_{p,PCM}$ [J kg^{-1} K^{-1}]	2100
Thermal Conductivity of PCM, k_{PCM} [W m^{-1} K^{-1}]	0.2
*Latent Heat of Fusion, ΔH_{PCM} [kJ kg^{-1}]	150
Melting temperature, T_m [K]	298
Dynamic Viscosity, μ [kg m^{-1} s^{-1}]	3.86x10^{-3}

** When not used in parametric analysis, the value of the parameter in the table is taken as a constant*

3.2.5. Modeling of PEM Fuel Cell Characteristics

In this study, the curves given in the 2 kW Horizon H2000 PEM fuel cell manual were used for the fuel cell model (Horizon Educational-H2000, 2024). Fuel cell specifications are given in Table 3.3. The necessary data was obtained by developing power-related correlations from the relevant curves using the curve fitting method. The polarization curve of the fuel cell is given in Figure 3.8. Figures 3.9 and 3.10 show changes in hydrogen flow rate under system power and system power under fuel cell current, respectively.

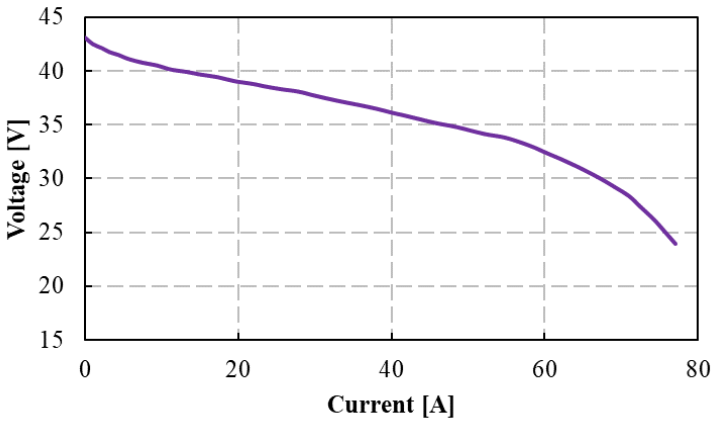

Figure 3.8 Polarization curve of the H2000 PEM fuel cell (Horizon Educational-H2000, 2024)

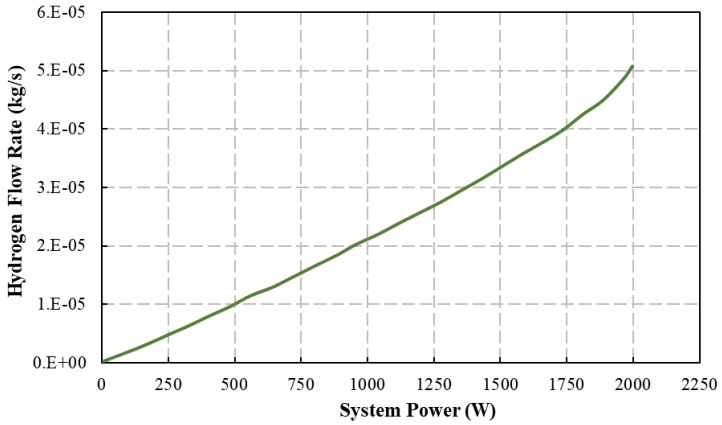

Figure 3.9 Changes in hydrogen flow rate under system power of the H2000 PEM fuel cell (Horizon Educational-H2000, 2024)

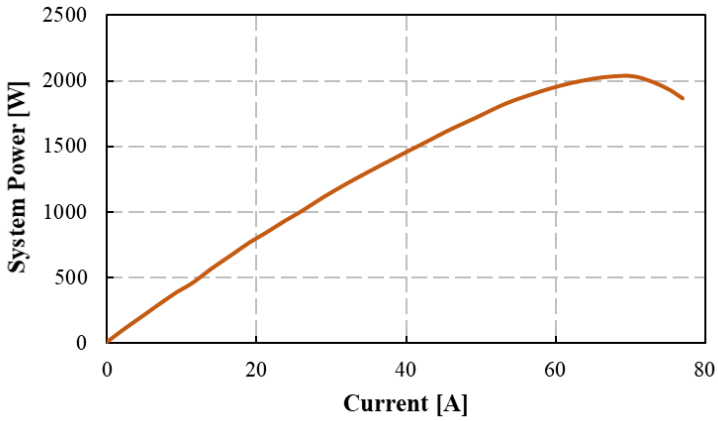

Figure 3.10 Changes in system power under fuel cell current of the H2000 PEM Fuel Cell (Horizon Educational-H2000, 2024)

Table 3.3 H2000 PEM fuel cell specifications (Horizon Educational-H2000, 2024)

Parameters	**Value**
Type of Fuel Cell	PEM
Number of Stack	48
Dimensions	30.3 cm × 35 cm × 18.3 cm
Rated Power	2000 W
H_2 Pressure at the Inlet	0.45 – 0.55 bar
Reactants	Hydrogen and Air
Maximum Stack Temperature	65 °C

3.2.6. Modeling of Fuel Cell Exhaust Air Temperature

The heat produced by the fuel cell is calculated as follows. The waste heat values calculated using Equations (3.16) and (3.17) can be substituted into Equation (3.18) to determine the fuel cell's outlet temperature, $T_{fc,out}$.

$$\dot{Q} = \dot{n}_{H_2O(l)}\bar{c}_{p,water}\left(T_{fc,out} - T_{amb}\right) + \dot{n}_{O_2,outlet}\bar{c}_{p,O_2}\left(T_{fc,out} - T_{amb}\right) + \dot{n}_{N_2,outlet}\bar{c}_{p,N_2}\left(T_{fc,out} - T_{amb}\right) \tag{3.16}$$

$$\dot{Q}_{thermal}^{waste} = I_{fc}(V_{th} - V_{cell}) \tag{3.17}$$

$$\dot{Q}_{efficiency}^{waste} = \dot{Q}_{max}(1 - (\eta_{FC})) \tag{3.18}$$

where $\dot{Q}_{thermal}^{waste}$ waste heat from the thermal voltage approach, $\dot{Q}_{efficiency}^{waste}$ waste heat from the efficiency approach, $\dot{n}_{H_2O(l)}$, $\dot{n}_{O_2,outlet}$, and $\dot{n}_{N_2,outlet}$ are the molar flow rates of liquid water, oxygen, and nitrogen expelled from the fuel cell, respectively, $\bar{c}_{p,water}$, $\bar{c}_{p,O_2}$, and $\bar{c}_{p,N_2}$ are the specific heats of water, oxygen, and nitrogen, respectively, T_{amb} is the ambient temperature, I_{fc} is the fuel cell current, V_{th} is the thermal voltage, V_{cell} is the cell voltage of the fuel cell, $\dot{Q}_{max}$ is the maximum heat that a fuel cell can generate (taken from Horizon Educational-H2000 (2024)) and η_{FC} is the efficiency of the fuel cell. The outlet molar flow rates of oxygen and nitrogen can be calculated as follows,

$$\dot{n}_{O_2,outlet} = \dot{n}_{O_2,inlet} - \frac{I_{fc}}{4 \cdot F} \tag{3.19}$$

$$\dot{n}_{N_2,outlet} = \dot{n}_{N_2,inlet} \tag{3.20}$$

where $\dot{n}_{O_2,inlet}$ and $\dot{n}_{N_2,inlet}$ are molar flow rates of oxygen and nitrogen entered from the fuel cell. These are obtained by multiplying the molar flow rate of air entering the fuel cell by the coefficients of the oxygen and nitrogen ratios in the air as follows. It is assumed that there is a mixture of 21% oxygen and 79% nitrogen in the air.

$$\dot{n}_{O_2,inlet} = 0.21\dot{n}_{air} \tag{3.21}$$

$$\dot{n}_{N_2,inlet} = 0.79\dot{n}_{air} \tag{3.22}$$

The molar flow rate of air is calculated as follows, depending on the mass flow rate of the air below, $\dot{m}_{air}$,

$$\dot{n}_{air} = \frac{\dot{m}_{air}}{MW_{air}} \tag{3.23}$$

$$\dot{m}_{air} = \rho_{air}\dot{\forall}_{air} \tag{3.24}$$

The mass flow rate of the air is calculated with Equation (3.24). In this study, the mass flow rate of the air was taken using the curves given in the fuel cell manual and the curve fitting method. When calculating the molar flow rate of air, the airflow rate at the cathode exit of the fuel cell should be used. The cathode output flow rate can be calculated as follows. MW_{air}, represents the molar weight of air and can be calculated as follows.

$$MW_{air} = x_{O_2}MW_{O_2} + x_{N_2}MW_{N_2} \tag{3.25}$$

where x_{O_2} and x_{N_2} are the stoichiometric ratios of oxygen and nitrogen, respectively, and can be calculated with the following equations.

$$x_{O_2} = \frac{\dot{n}_{O_2,outlet}}{\dot{n}_{outlet}^{cathode}} \tag{3.26}$$

$$x_{N_2} = \frac{\dot{n}_{N_2,outlet}}{\dot{n}_{outlet}^{cathode}} \tag{3.27}$$

The mass flow rate of the air taken from the manual of the fuel cell is the mass flow rate of the air entering the fuel cell. The value of the air coming out of the fuel cell and the air flow rate on the cathode side can be calculated as follows.

$$\dot{m}_{air} = \dot{n}_{outlet}^{cathode} MW_{air} \tag{3.28}$$

$$\dot{n}_{outlet}^{cathode} = \dot{n}_{O_2,outlet} + \dot{n}_{N_2,outlet} + \dot{n}_{H_2O,outlet} \tag{3.29}$$

3.2.7. Modeling of Temperature Controller

The exhaust air of the fuel cell is desired to be kept constant with an external heater. For this, the temperature controller is modeled to keep the excess air expelled from the cathode side of the fuel cell constant at a specific temperature. The heater power, $\dot{Q}_{heater}$, required to keep the exhaust air at a constant temperature can be calculated with the equation below.

$$\dot{Q}_{heater} = \dot{m}_{air} c_{p,air} \left(T_{airset} - T_{fc,out}\right) \tag{3.30}$$

where $\dot{m}_{air}$ is the flow rate of the exhaust air, $c_{p,air}$ is the specific heat of the air, T_{airset} is the air set temperature and $T_{fc,out}$ is the air temperature that is expelled from the fuel cell. The characteristic curve of the exhaust air for the 2 kW H2000 PEM fuel cell is given in Figure 3.11. The temperature correlation, depending on fuel cell power, was obtained using the curve fitting method and implemented into the model. The PID controller block in Simulink was used to control the temperature. Simulink blocks of the temperature controller are given in Figure 3.12.

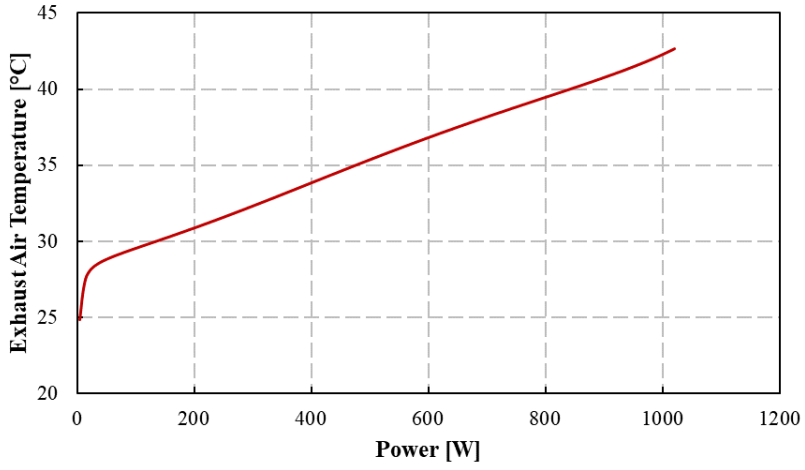

Figure 3.11 Change of excess air expelled from the cathode side of the fuel cell under power for fuel cell

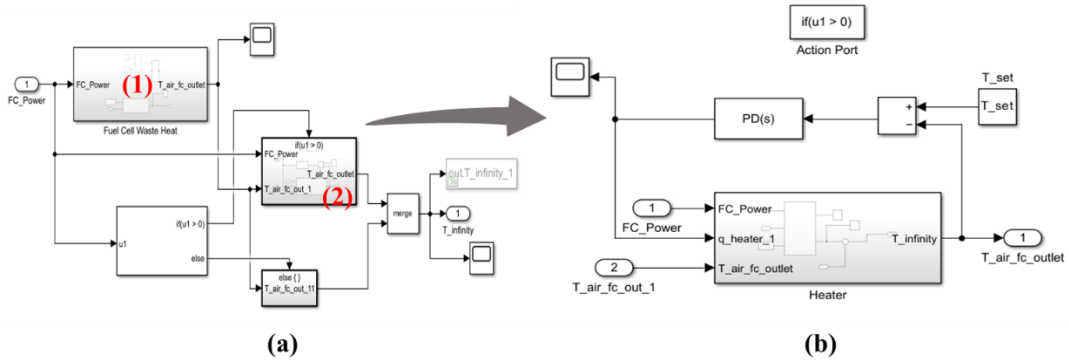

Figure 3.12 (a) Temperature controller subsystem (1-Fuel cell exhaust heat model, 2-PID controller) and (b) PID controller subsystem

3.2.8. Modeling of Hydrogen Flow Rate Controller Algorithm

A Simulink controller was used in Scenario-3 and Scenario-4 to regulate the hydrogen flow and ensure the tanks' sequential operation. Temperature and pressure conditions were defined for the controller. The algorithm for the H_2 flow controller is provided in Figure 3.13. The H_2 flow rate that should be discharged from the tanks is calculated from the vehicle's power consumption. In the algorithm, initially, the first tank opens to supply the requested hydrogen. The controller checks the second tank when the first tank's pressure falls below the limit pressure or the first tank's temperature drops below the limit temperature. For the tanks to operate safely, the limit temperature and pressure are established. If the second tank's pressure falls below the limit pressure or its temperature drops below the limit temperature, the first tank is rechecked. If the first tank's pressure and temperature are above the limit pressure and temperature, the first tank is opened; otherwise, the third tank is opened. When the third tank's pressure and temperature fall below the limit pressure and temperature, the first and second tanks are rechecked. If the pressure and temperature of either the first or second tank are above the limit pressure and temperature, the first or second tank is opened. If not, all tanks' pressures and temperatures are checked, and if they are above the minimum pressure and temperature, the tanks are opened simultaneously. If not, the simulation is stopped.

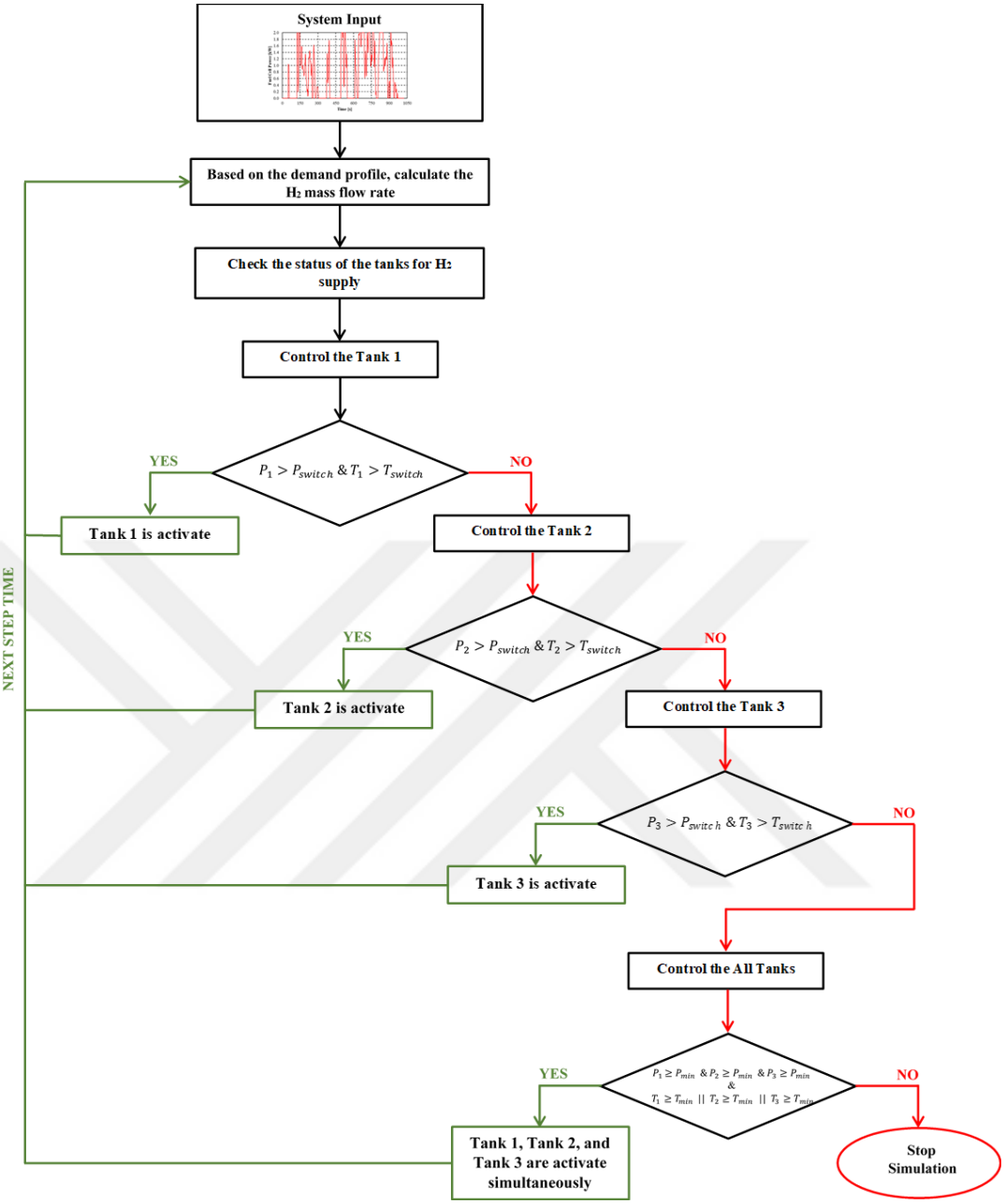

Figure 3.13 Flow chart for control algorithm for H_2 flow controller

3.3. Model Verifications

Verification studies for the absorption and desorption processes of the metal hydride tank, for which a detailed model was created, and the temperature characteristic of the excess air expelled from the cathode side of the fuel cell were carried out.

3.3.1. Verification of Metal Hydride Absorption/Desorption Behaviour

The consistency of the current absorption model was examined by reproducing the CFD model developed by Tong et al. (2019) in COMSOL on the thermal management of the metal hydrate absorption process. The consistency of the current absorption model was also examined by reproducing the desorption model developed in the same way as the absorption model of Tong et al. (2021). Figure 3.14 for the absorption model and Figure 3.15 for the desorption model compare the changes in weight fractions and average MH tank temperatures obtained from reference studies and the current models, and the results appear to be an almost perfect match.

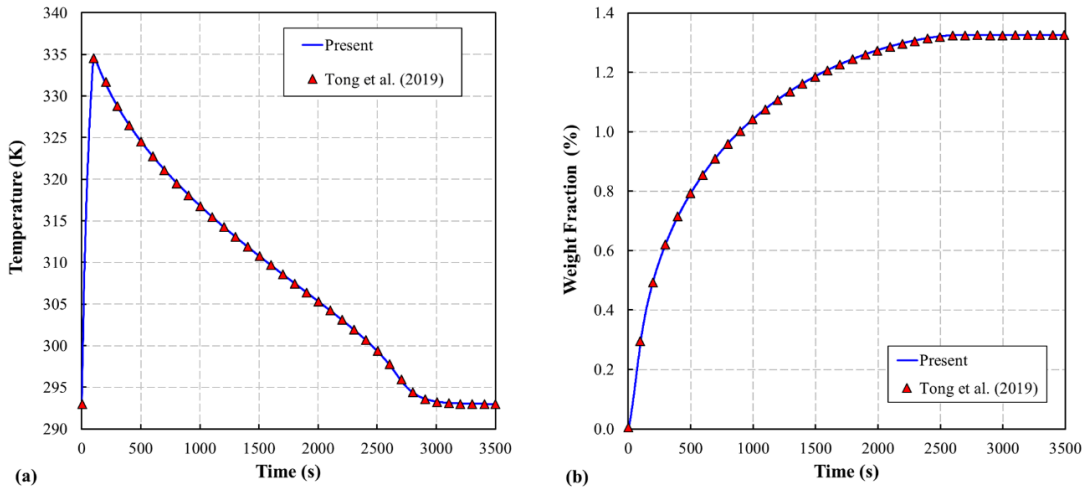

Figure 3.14 Absorption model verification with Tong et al. (Tong et al., 2019) (a) temperature and (b) weight fraction

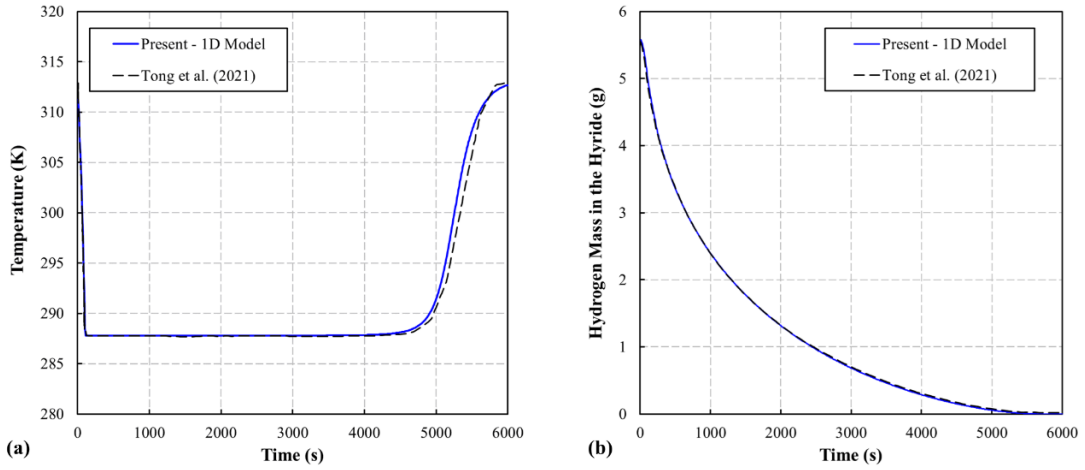

Figure 3.15 Desorption model verification with Tong et al. (2021) (a) tank temperature and (b) hydrogen mass in the hydride

3.3.2. Verification of Fuel Cell Exhaust Heat Characteristics

The temperature characteristic of the excess air discharged from the cathode of the FC has been compared with the results of a thermal model developed by Cano, Kelouwani, Agbossou, & Dubé (2014) based on their experimental findings as well as an electrochemical model and a heat transfer model to calculate the fuel cell's average stack temperature. The findings are presented in Figure 3.16. It seems that the thermal voltage method is closer to the results of the reference study, so the thermal voltage model was used in the system model to calculate the temperature of the exhaust air on the cathode side of the fuel cell. Horizon H1000XP 1 kW PEMFC was used to verify the fuel cell temperature characteristic. The characteristics of the FC are given in Table 3.4.

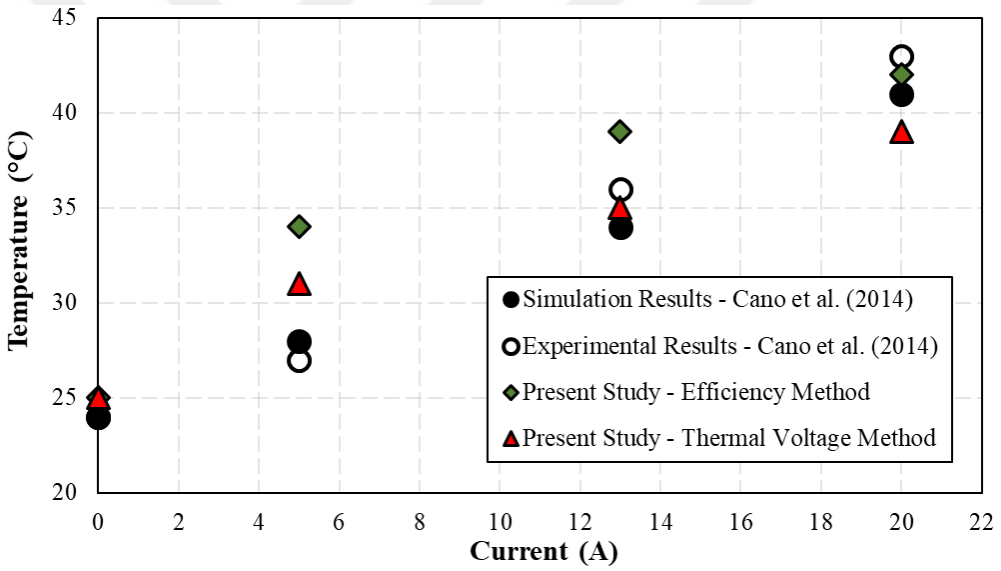

Figure 3.16 Fuel cell temperature characteristic model verification with Cano et al. (2014)

Table 3.4 H1000-XP PEM fuel cell specifications (Horizon Educational-H1000XP, 2024)

Parameters	**Value**
Type of Fuel Cell	PEM
Number of Stack	50
Dimensions	26.4 cm × 20.3 cm × 10.4 cm
Rated Power	1100 W
H_2 Pressure at the Inlet	0.45 – 0.55 bar
Reactants	Hydrogen and Air
Maximum Stack Temperature	65 °C

CHAPTER FOUR
RESULTS AND DISCUSSION

4.1. A Case Study: Stand-Alone MH/PCM Charging System

To investigate the behavior of the MH tank under passive thermal management and charging process, PCM material has been added to the tank's exterior. 540 analyses were conducted using different design and operating parameters (Table 4.1). The changes in hydride weight fraction, PCM liquid fraction, and MH tank temperature parameters were investigated under these varying parameters.

Table 4.1 The design and operating parameters used for the analyses

Design Parameters	***PCM Thickness*** Δt_{PCM}	1 cm to 5 cm 0.5 cm *interval*
	PCM Melting Temperature $T_{melting}$	27°C to 35°C 1°C *interval*
	MH Diameter R_{MH}	2,5 cm – 3 cm – 4 cm – 5 cm
Operating Parameters	***Inlet Pressure*** P_{H_2}	8 bar – 10 bar – 12 bar

As a result of the analyses, the time-dependent changes in different weight fractions, liquid fractions, MH temperature, and PCM temperature are shown in Figure 4.1 for an MH radius of 3.5 cm and an inlet pressure of 8 bar, in Figure 4.2 for an MH radius of 2.5 cm and an inlet pressure of 12 bar, and Figure 4.3 for an MH radius of 5 cm and an inlet pressure of 12 bar. It is observed that the hydride weight fraction increases as the PCM thickness increases and decreases as the PCM melting temperature increases. However, it does not change much after the PCM thickness reaches 3 cm and the melting temperature of PCM is 31°C. The maximum weight fraction is reached when the PCM thickness is 3 cm or higher. Similarly, it is noted that the MH temperature does not change much after the PCM thickness is 3 cm and the melting temperature is 31°C. It can be stated that as the PCM thickness and melting temperature increase, the PCM liquid fraction and PCM temperature decrease. As seen in Figures 4.2a and 4.3a, an increase in the hydrogen inlet pressure leads to an increase

in the weight fraction. Figures 4.2a and 4.3a indicate that the weight fraction decreases as the MH radius increases.

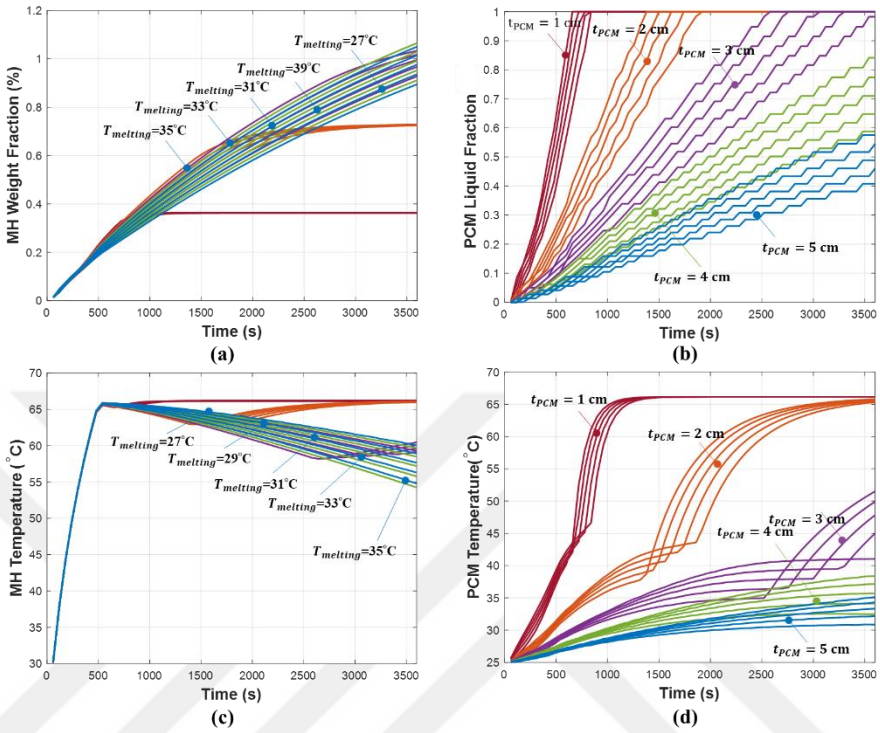

Figure 4.1 Under the MH radius of 2.5 cm and an inlet pressure of 8 bar, the time-dependent (a) hydride weight fraction, (b) PCM liquid fraction, (c) MH temperature, and (d) PCM temperature at different PCM thicknesses and melting temperatures.

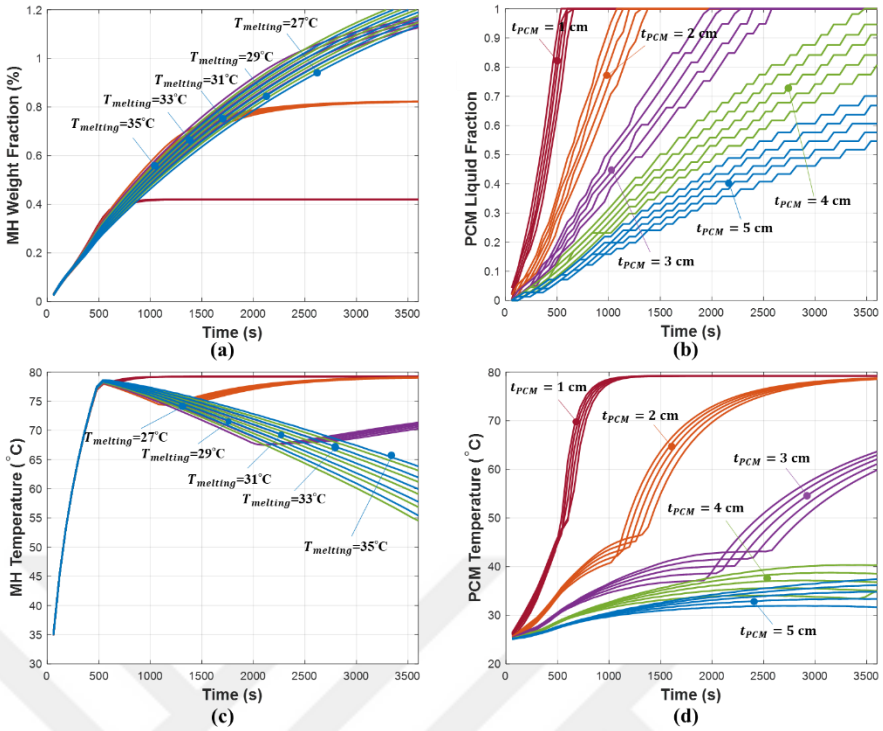

Figure 4.2 Under the MH radius of 2.5 cm and an inlet pressure of 12 bar, the time-dependent (a) hydride weight fraction, (b) PCM liquid fraction, (c) MH temperature, and (d) PCM temperature at different PCM thicknesses and melting temperatures

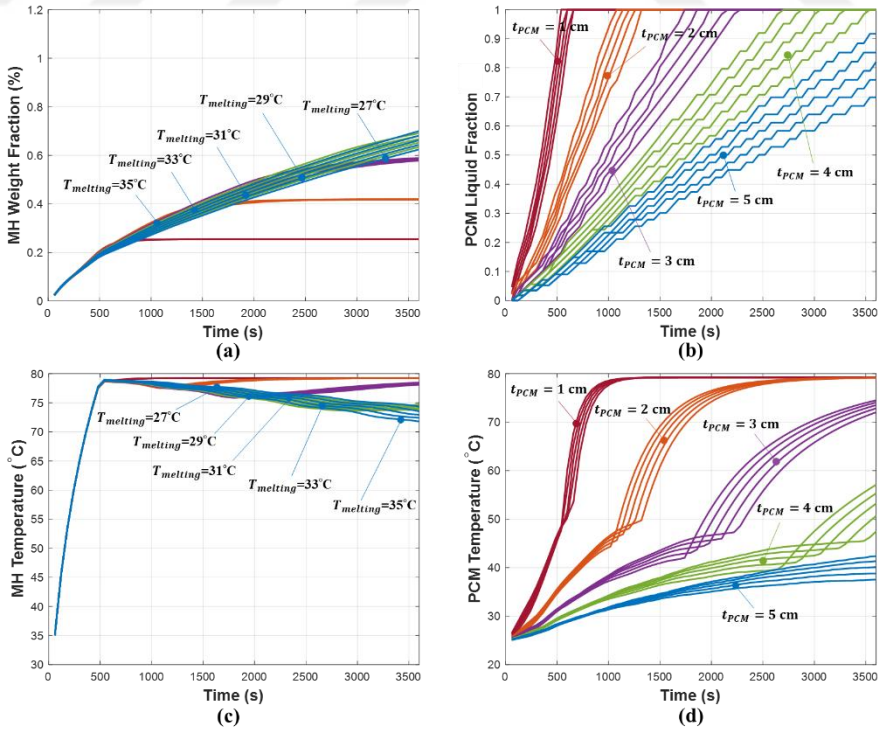

Figure 4.3 Under the MH radius of 5 cm and an inlet pressure of 12 bar, the time-dependent (a) hydride weight fraction, (b) PCM liquid fraction, (c) MH temperature, and (d) PCM temperature at different PCM thicknesses and melting temperatures

Figures 4.4 and 4.5 show the percentage of hydrogen in the tank for different inlet pressures and PCM thicknesses for MH thicknesses of 2.5 cm and 5 cm at a PCM melting temperature of 27°C. Generally, the percentage of hydrogen in the tank increases with increasing pressure and PCM thickness. For an MH radius of 2.5 cm, maximum storage is observed at a PCM thickness of 4 cm and an inlet pressure of 12 bar. It is also observed that the percentage of hydrogen in the tank is lower for an MH radius of 5 cm compared to an MH radius of 2.5 cm.

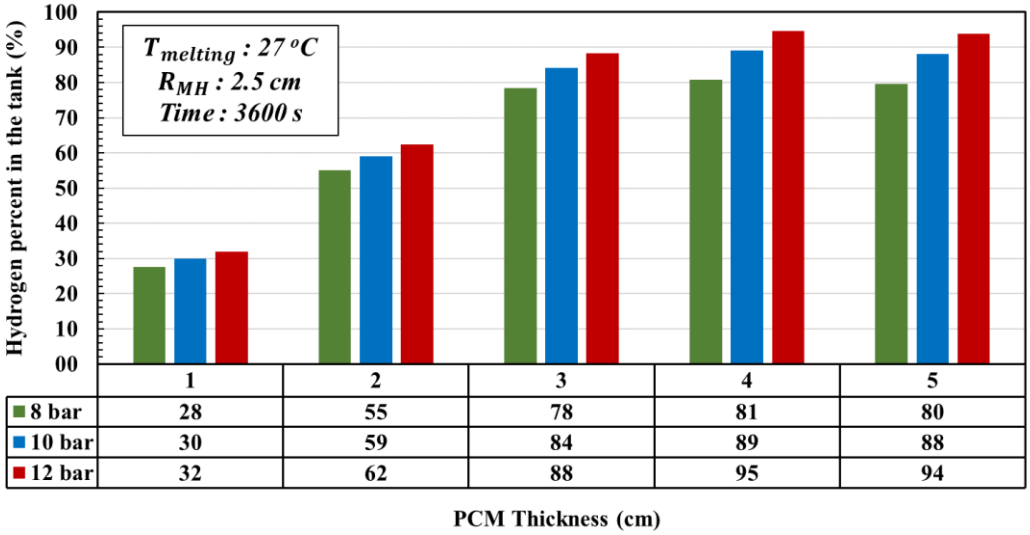

	1	2	3	4	5
8 bar	28	55	78	81	80
10 bar	30	59	84	89	88
12 bar	32	62	88	95	94

Figure 4.4 The percentage of hydrogen in the tank under different pressure and PCM thickness conditions for an MH radius of 2.5 cm.

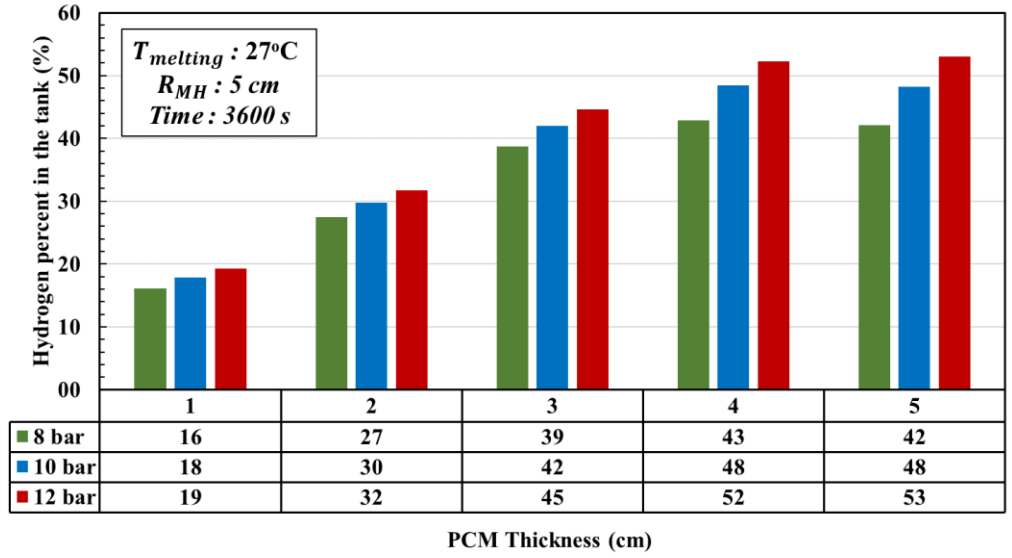

	1	2	3	4	5
8 bar	16	27	39	43	42
10 bar	18	30	42	48	48
12 bar	19	32	45	52	53

Figure 4.5 The percentage of hydrogen in the tank under different pressure and PCM thickness conditions for an MH radius of 5 cm.

Figure 4.6 depicts tank temperature, weight fraction, and PCM liquid fraction graphs at different PCM thicknesses and melting temperatures under an 8 bar inlet pressure. The tank temperature does not undergo significant changes with variations in PCM thickness and melting temperature. The weight fraction and liquid fraction vary between 0.5 and 1. The weight fraction increases with PCM thickness and melting temperature while the liquid fraction decreases. These results are consistent with the findings discussed above.

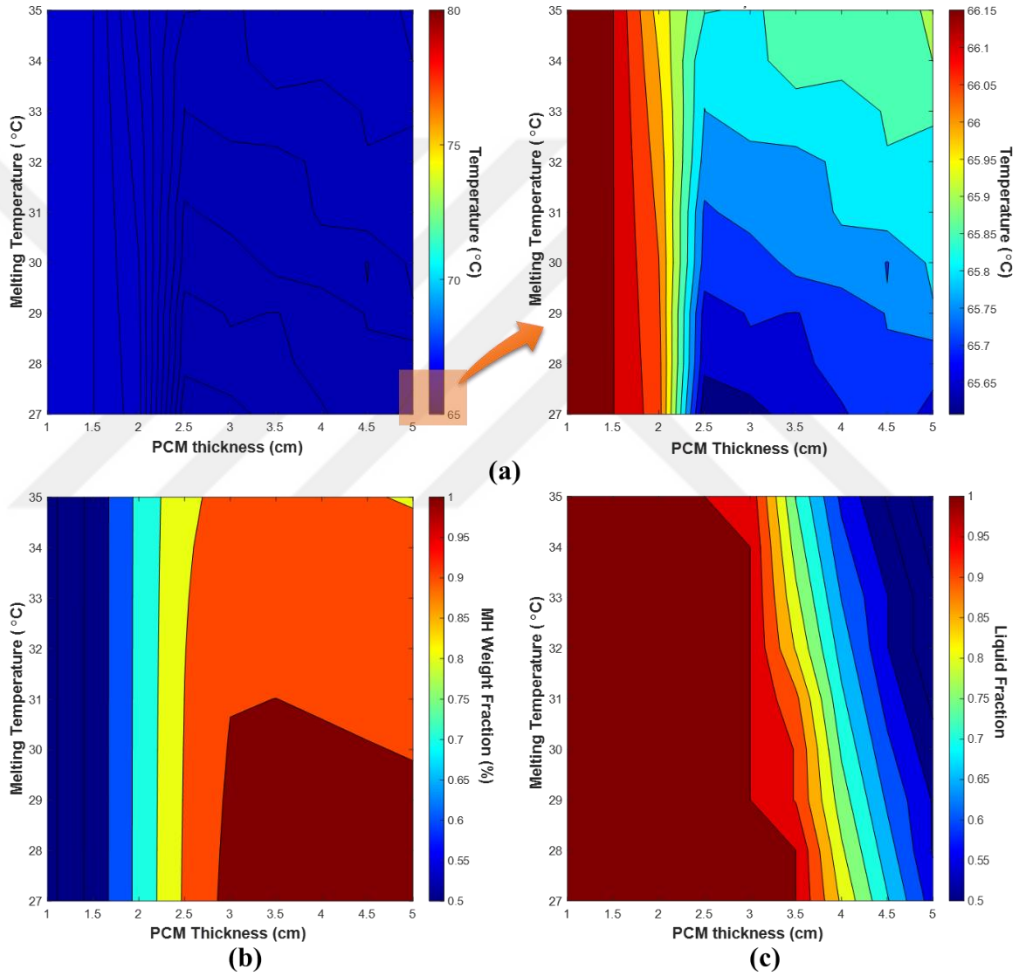

Figure 4.6 Under an 8 bar inlet pressure, the time-dependent changes in (a) tank temperature and its expanded view at different PCM thicknesses and melting temperatures, (b) hydride weight fraction, and (c) PCM liquid fraction.

Figure 4.7 presents tank temperature, weight fraction, and PCM liquid fraction graphs at different PCM thicknesses and melting temperatures under a 10-bar inlet pressure. Upon examining the graphs, similar observations can be made to those made

with the 8-bar contour graphs. Increasing the pressure causes higher temperatures. The weight fraction increases more rapidly, and the liquid fraction decreases more rapidly.

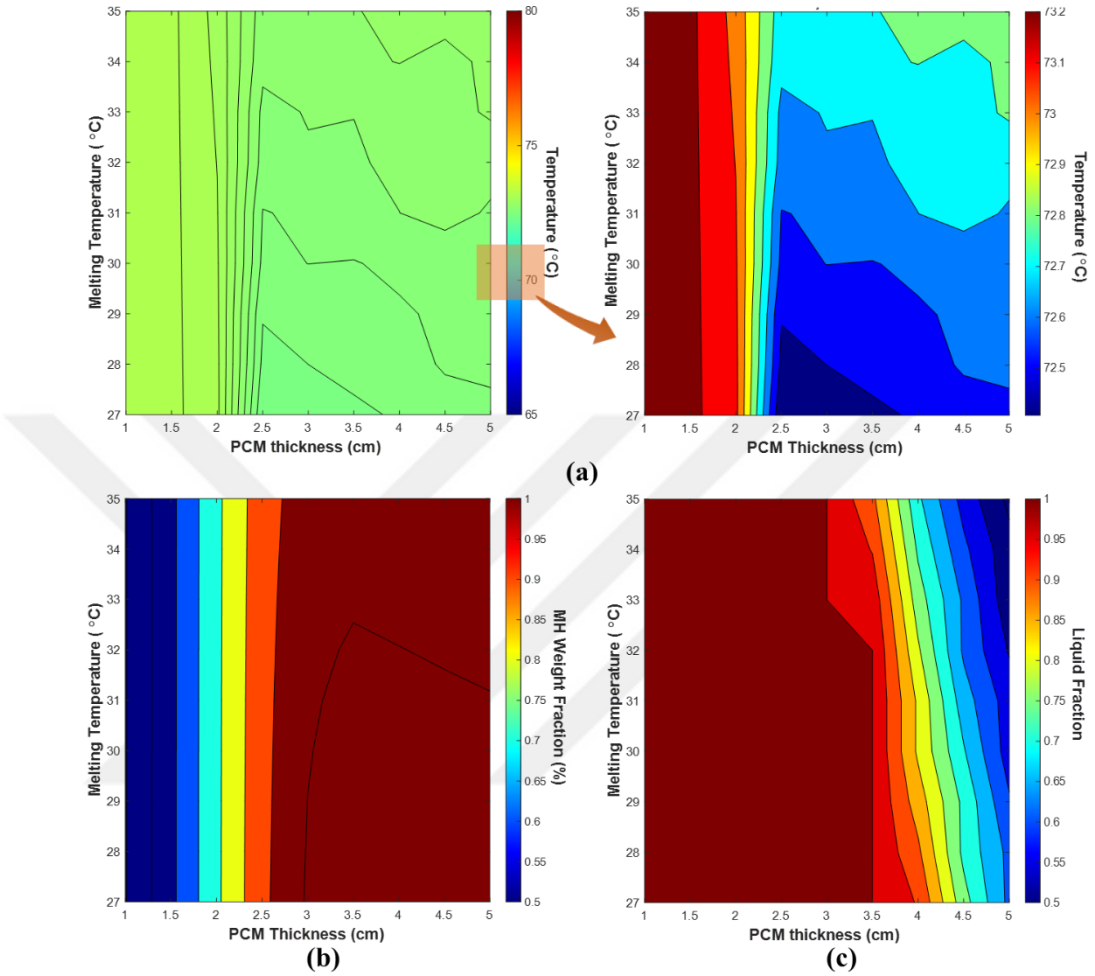

Figure 4.7 Under a 10 bar inlet pressure, the time-dependent changes in (a) tank temperature and its expanded view, (b) hydride weight fraction, and (c) PCM liquid fraction at different PCM thicknesses and melting temperatures.

The contour graphs in Figure 4.8 depict tank temperature, weight fraction, and PCM liquid fraction at different PCM thicknesses and melting temperatures under a 12-bar inlet pressure. It is evident that the tank temperature is higher compared to 8 and 10 bar pressures. The weight fraction has increased more rapidly, and the PCM liquid fraction has also decreased more rapidly.

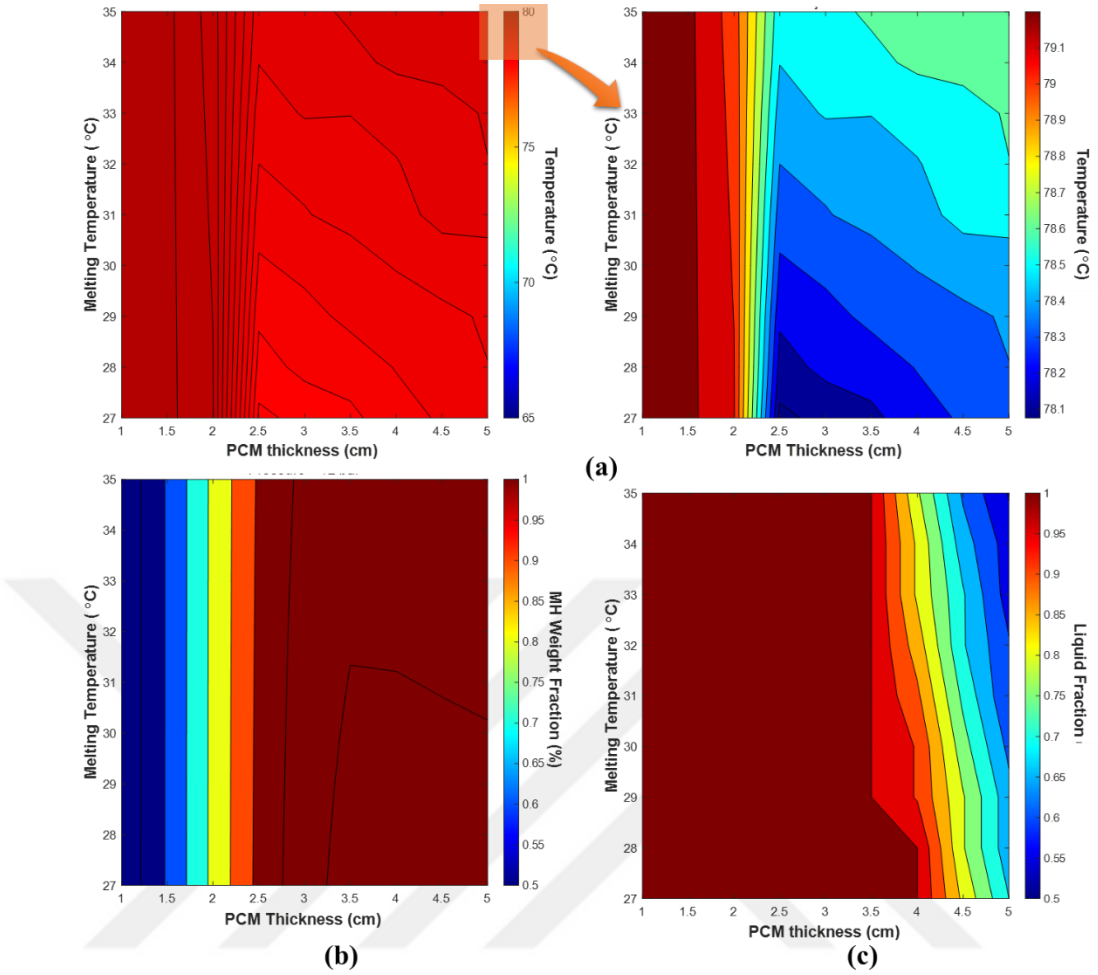

Figure 4.8 Under a 12 bar inlet pressure, the time-dependent changes in (a) tank temperature and its expanded view, (b) hydride weight fraction, and (c) PCM liquid fraction at different PCM thicknesses and melting temperatures.

In Figure 4.9, the changes in hydride weight fraction and PCM liquid fraction can be observed as a function of PCM melting temperature and PCM thickness under different pressure values. As mentioned above, it is observed that an increase in hydrogen inlet pressure results in an increase in the weight fraction and a decrease in the liquid fraction.

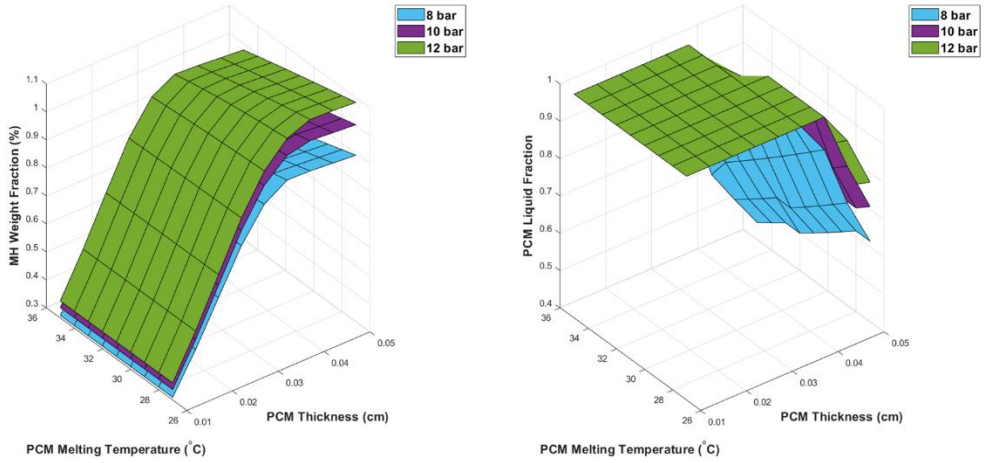

Figure 4.9 Under different pressure values, the changes in (a) hydride weight fraction and (b) PCM liquid fraction as a function of PCM melting temperature and PCM thickness

By conducting a total of 540 analyses, changes in hydride weight fraction and PCM liquid fraction were calculated for different PCM thicknesses, PCM melting temperatures (ranging from 27°C to 35°C), MH radius, and inlet pressure values. Using the MINITAB software and Response Surface Method (RMS), optimum PCM thickness and PCM temperature values for maximizing the weight fraction and liquid fraction were determined. These values for different MH tank radius and inlet pressure values are provided in Table 4.2.

Table 4.2 Optimization results for different MH radius and inlet pressures

MH Diameter (cm)	Inlet Pressure (bar)	PCM Thickness (cm)	Melting Temperature (ºC)
2.5	8	3.22	27
	10	3.26	27
	12	3.43	27
3	8	3.26	27
	10	3.46	27
	12	3.58	27
4	8	3.38	27
	10	3.63	27
	12	3.90	27
5	8	3.47	27
	10	3.78	27
	12	3.99	27

The analyses were repeated using the optimization results provided in Table 4.2. As a result of these analyses, the time-dependent changes in weight and liquid fraction are shown in Figure 4.10 for the optimum PCM thickness and PCM melting temperature values. At the end of the analysis period (3600 s), the weight and liquid fraction values are given in Table 4.3. According to these results, for the MH tank used in the analysis, it can be observed that the operating pressure yielding the highest weight fraction is 12 bar with an MH radius of 2.5 cm.

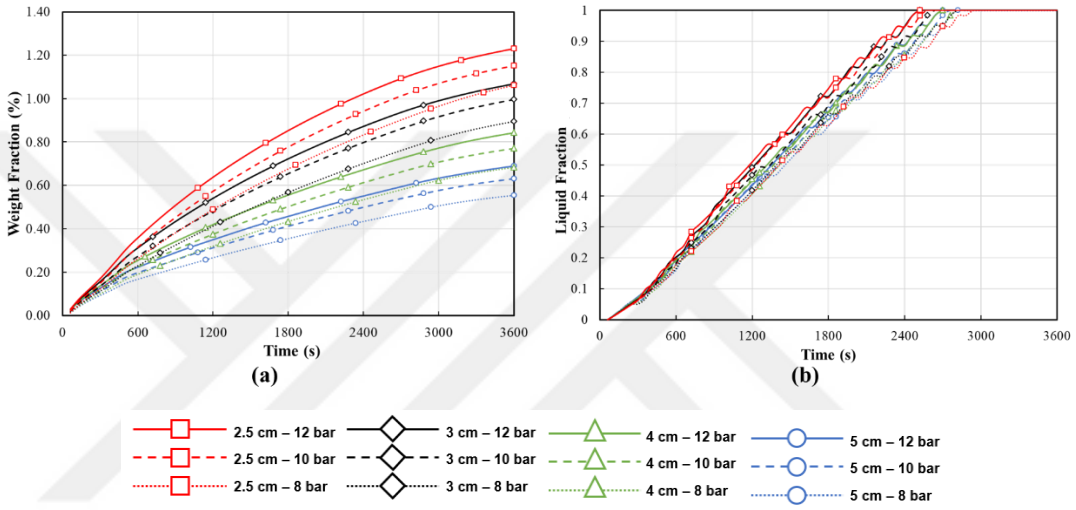

Figure 4.10 For the optimal PCM thickness and melting temperature values, the time-dependent changes in (a) weight fraction and (b) liquid fraction

Table 4.3 The values at the end of 3600 s for the optimum PCM thickness and PCM melting temperature

MH Diameter (cm)	Inlet Pressure (bar)	MH Temperature (ºC)	PCM Temperature (ºC)	Liquid Fraction	Weight Fraction (%)
2.5	8	57.75	45.36	1	1.061
	10	62.73	51.51	1	1.15
	12	63.64	51.60	1	1.22
3	8	61.005	49.18	1	0.89
	10	65.42	52.008	1	0.99
	12	68.96	54.75	1	1.06
4	8	63.23	51.51	1	0.68
	10	68.66	54.43	1	0.76
	12	72.26	54.64	1	0.84
5	8	64.06	52.23	1	0.55
	10	69.86	54.92	1	0.63
	12	74.75	57.21	1	0.69

4.2. Investigation on Thermally Coupled FC-MH System

After verification of the sub-models and the creation of the system model, parametric analyses were conducted at different ambient temperatures, with various tank geometries and different numbers of tanks. These analyses aimed to investigate the effects of these parameters on range, tank temperature, and tank pressure. These parametric analyses serve as a preliminary study to determine the conditions under which the system operates safely and efficiently.

Five different cases were used in the analyses. Case-1, Case-2, and Case-3 involved 1, 2, and 8 tanks, respectively, with the number of tanks kept constant and the stored hydrogen amount varied. Case-2, Case-4, and Case-5 maintained constant stored hydrogen amounts while conducting parametric analyses under different aspect ratios. The geometries of the cases used, and the values of stored hydrogen amounts are provided in Table 4.4.

Table 4.4 Specification of the cases

Cases	Case-1	Case-2	Case-3	Case-4	Case-5
***Diameter* [cm]**	14	10	5	15	5
***Height* [cm]**	25	25	25	11	100
***Amount of Storage H_2* [g]**	184	94	23	94	94

In the model, the driving cycle given in Figure 4.11 was used as an input, and the power values that the fuel cell and battery need to provide for the movement of a small fuel cell-battery hybrid vehicle throughout the driving cycle were calculated. The power curves are provided in Figures 4.12 and 4.13. The duration of the driving cycle is 1022 seconds, and the cycle length is 8 km. In parametric analyses, the analysis time was taken as the time obtained by repeating the driving cycle 8 times (8183 s).

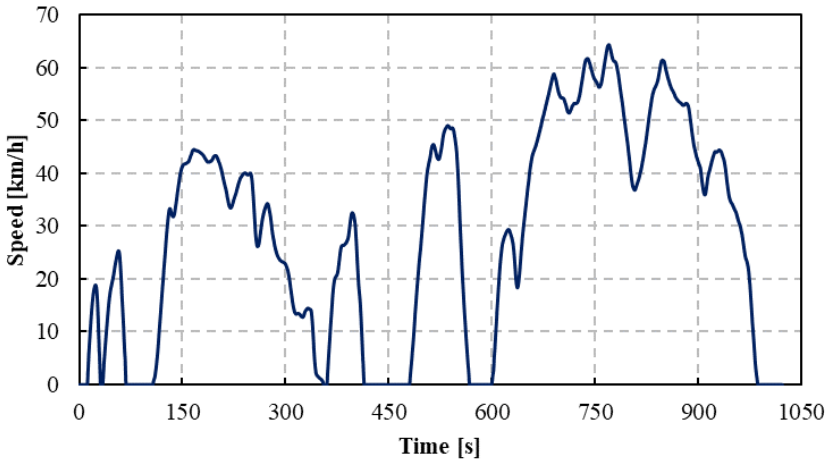

Figure 4.11 The driving cycle's speed-time graph

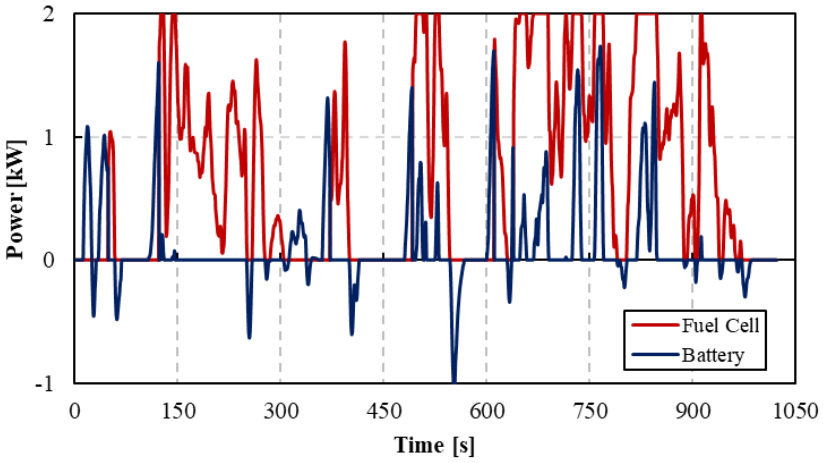

Figure 4.12 Comparative power-time graph for the fuel cell and battery

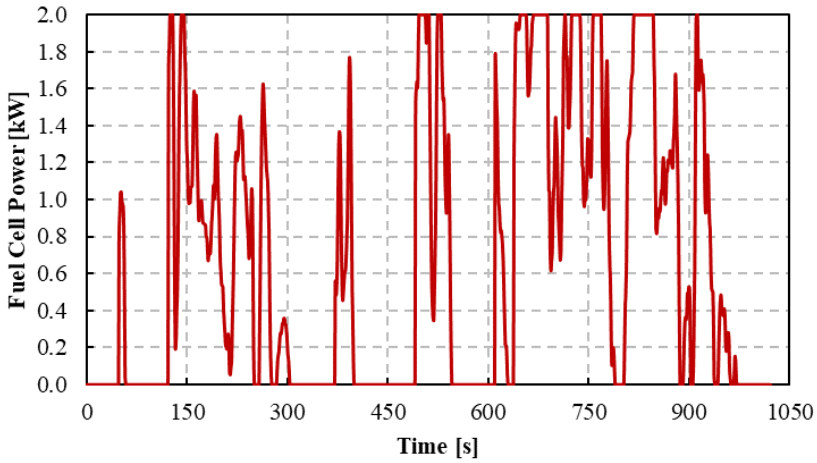

Figure 4.13 Power-time graph for the fuel cell

4.2.1. Investigation of Heat Transfer Coefficient for Different Cases

In the analysis results given in Figure 4.14, Figure 4.15, and Figure 4.16, the variation of MH tank temperature with different tank numbers and different heat transfer coefficients is presented for cases where the stored hydrogen amount remains constant with varying diameters of the tank and fixed tank height in Case-1, Case-2, and Case-3, respectively. When considering each case separately, it is observed that an increase in the heat transfer coefficient leads to a higher rate of temperature increase. In Case-3, the temperature nearly reached 25°C and attained the longest

analysis duration at a convective heat transfer coefficient of 2000 W/m²K. A smaller tank diameter results in faster heating and cooling of the tank.

When considering all cases together, it is seen that as the tank diameter decreases, the range increases. The decrease in tank pressure is observed to decrease with the rise of the heat transfer coefficient. Tank pressure indicates the presence of free hydrogen inside the tank, and a higher tank pressure signifies desorption within the tank. The reduction in tank diameter has also reduced the decrease in tank pressure, increasing the range.

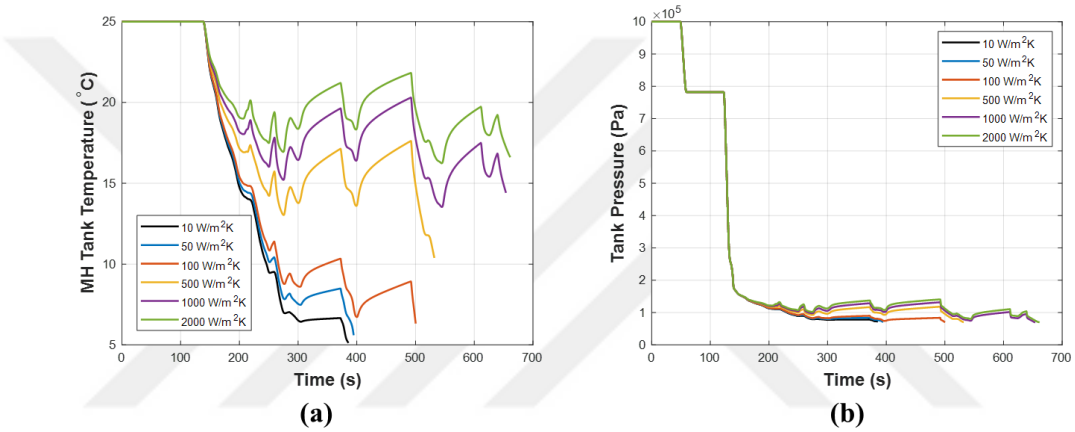

Figure 4.14 Under fixed H_2 amount, 25°C ambient temperature, and different convection coefficients for Case-1 (a) MH tank temperatures and (b) tank pressure

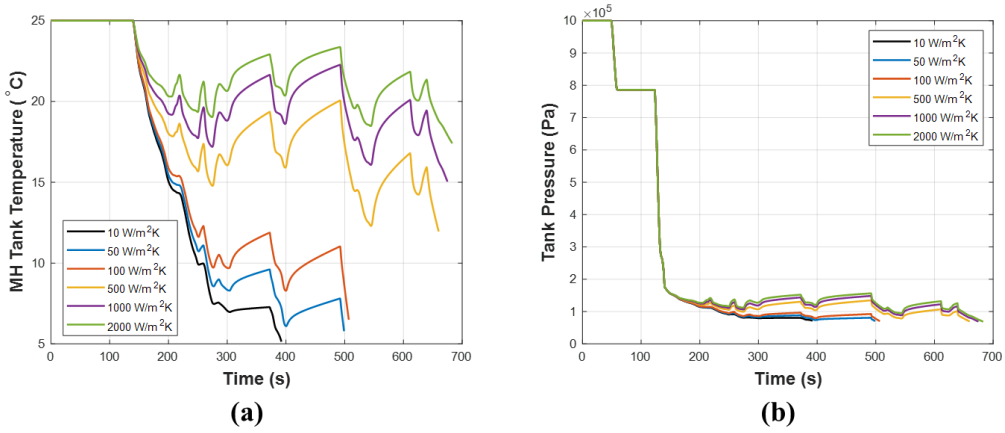

Figure 4.15 Under fixed H_2 amount, 25°C ambient temperature, and different convection coefficients for Case-2 (a) MH tank temperatures and (b) tank pressure

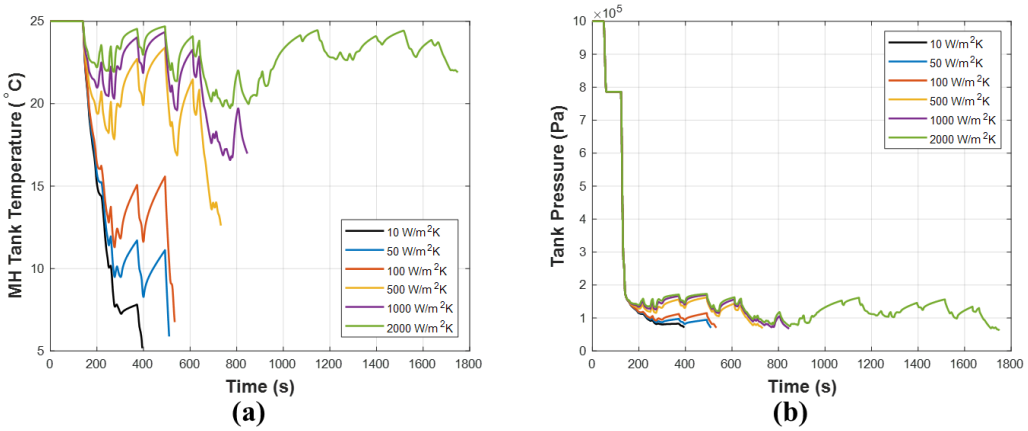

Figure 4.16 Under fixed H_2 amount, 25°C ambient temperature, and different convection coefficients for Case-3 (a) MH tank temperatures and (b) tank pressure

In the analysis conducted with tanks of different diameters and fixed tank numbers and height, while keeping the heat transfer coefficient constant, the temperature and pressure changes of the MH tank under different heat transfer coefficients and constant ambient temperatures are shown in Figure 4.17, Figure 4.18, and Figure 4.19. In the analyses for Case-1, Case-2, and Case-3, as portrayed in the figures, an increase in the heat transfer coefficient results in significant increases in temperature values.

Contrary to the earlier findings, the decrease in range as the diameter decreases is due to the constant number of tanks and the reduction in the amount of hydrogen stored in the tank as the diameter decreases. When considering each case separately, the rate of decrease in tank pressure has decreased with the rise of the heat transfer coefficient. When considering all cases together, an increase in tank diameter has reduced the rate of decrease in tank pressure, increasing range as the diameter increases.

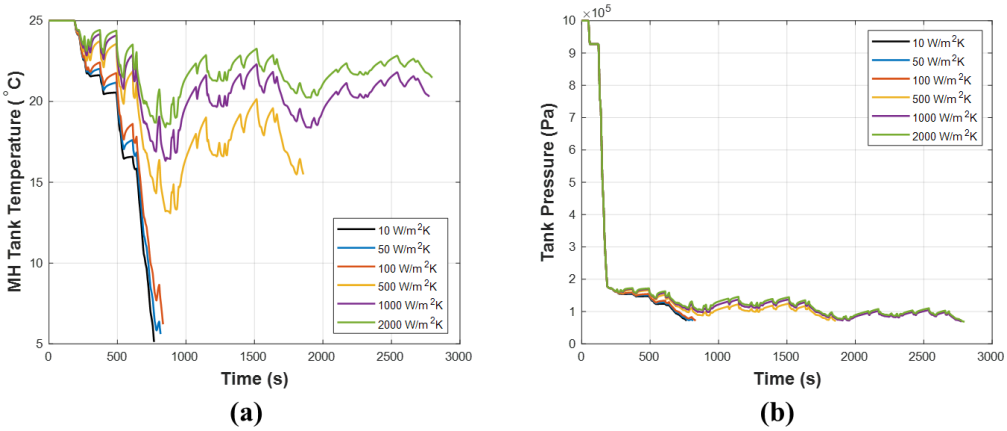

Figure 4.17 Under fixed tank number, 25 °C ambient temperature, and different convection coefficients for Case-1 (a) MH tank temperatures and (b) tank pressure

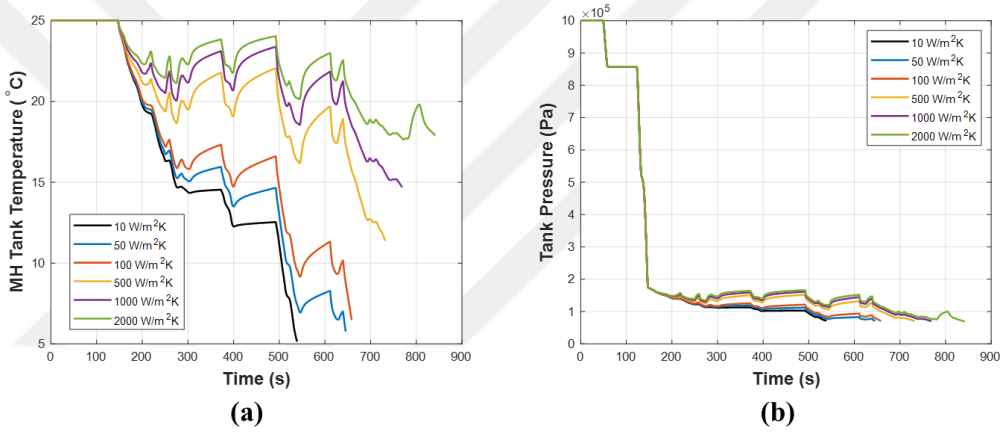

Figure 4.18 Under fixed tank number, 25 °C ambient temperature, and different convection coefficients for Case-2 (a) MH tank temperatures and (b) tank pressure

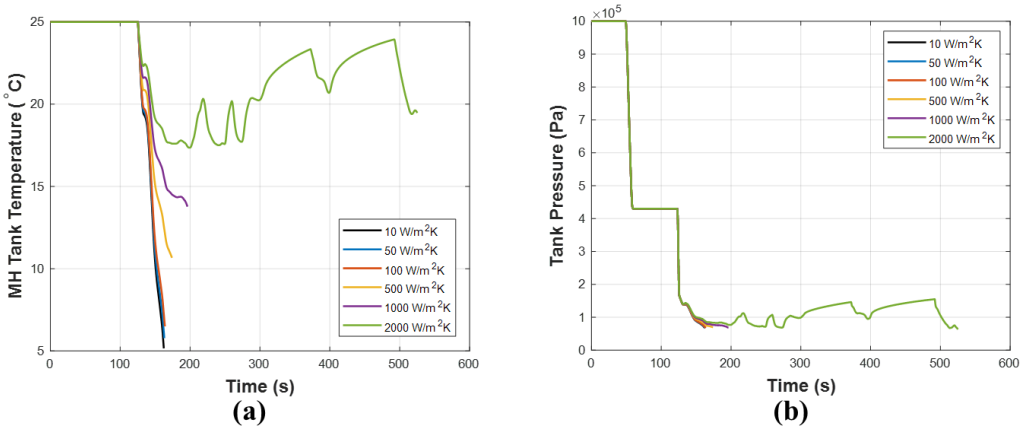

Figure 4.19 Under fixed tank number, 25 °C ambient temperature, and different convection coefficients for Case-3 (a) MH tank temperatures and (b) tank pressure

4.2.2. Investigation of Ambient Temperature for Different Cases

In the results shown in Figure 4.20, Figure 4.21, and Figure 4.22, the effect of different ambient temperatures on tank temperature and pressure was examined for Case-1, Case-2, and Case-3, with the stored hydrogen amount and heat transfer coefficient kept constant. When considering each case separately, an increase in ambient temperature results in an increase in tank temperature, a decrease in the rate of decrease in tank pressure, and an increase in range. In Case-3, with the increase in ambient temperature, the tank temperature reached 100°C, and the analysis duration extended to 8000 seconds. In comparison, the analysis durations in Case-1 and Case-2 ranged between 500 and 900 seconds. For the rate of decrease in tank pressure, Case-1 and Case-2 yielded similar results. In Case-3, the tank, starting with an initial pressure of 10 bar, was affected by the temperature increase and reached up to 15 bar around 6000 seconds. When considering all cases together, a decrease in tank diameter has significantly increased the range.

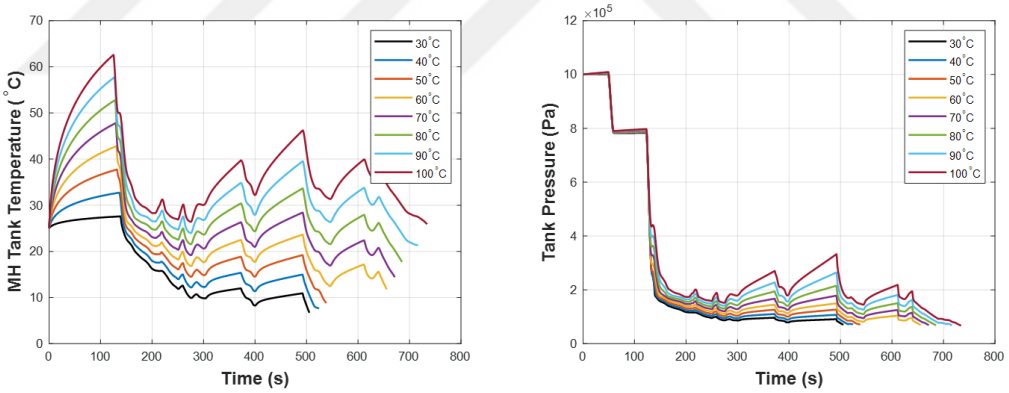

Figure 4.20 Under fixed H_2 amount, different ambient temperatures, and 100 W/m^{2}K convection coefficient for Case-3 (a) MH tank temperatures and (b) tank pressure

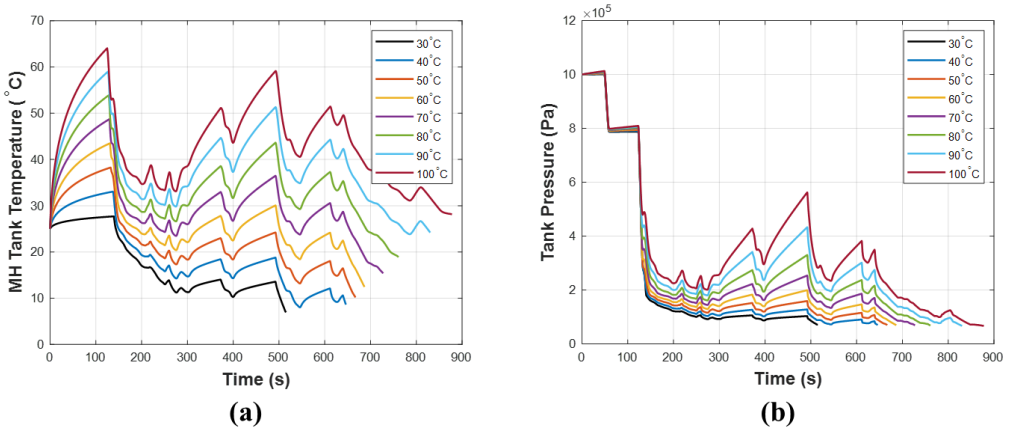

Figure 4.21 Under fixed H_2 amount, different ambient temperatures, and 100 W/m^{2}K convection coefficient for Case-3 (a) MH tank temperatures and (b) tank pressure

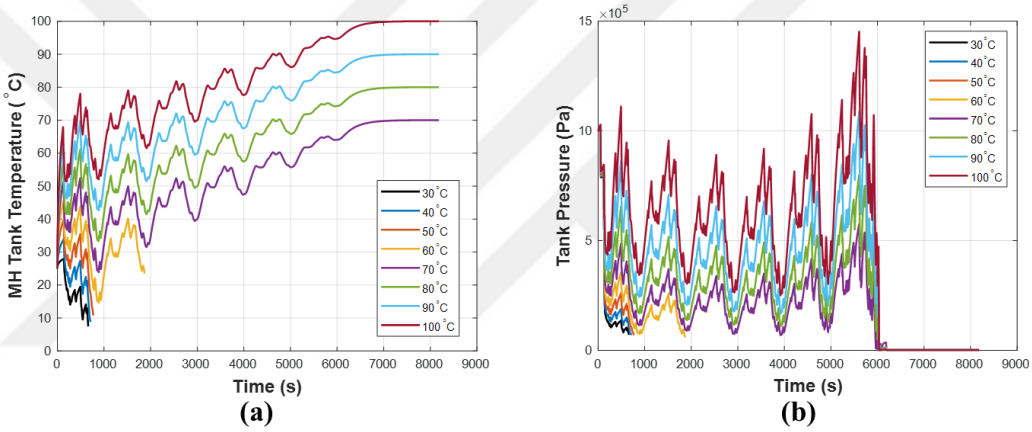

Figure 4.22 Under fixed H_2 amount, different ambient temperatures, and 100 W/m^{2}K convection coefficient for Case-3 (a) MH tank temperatures and (b) tank pressure

In Figure 4.23, Figure 4.24, and Figure 4.25, the variation of tank temperature and pressure under different ambient temperatures is presented for Case-1, Case-2, and Case-3, respectively, with the number of tanks held constant in 3 tanks. When evaluating each case separately, an increase in ambient temperature is observed to increase tank temperature and decrease the rate of decrease in tank pressure. As a result of these analyses, in Case-1, the tank temperature reached 80 degrees with the increase in ambient temperature and completed the analysis duration of 8000 seconds. It can also be observed that the rate of decrease in tank pressure was gradually slower in Case-3. Considering all cases together, since the number of tanks remains constant, a decrease in tank diameter has reduced the range.

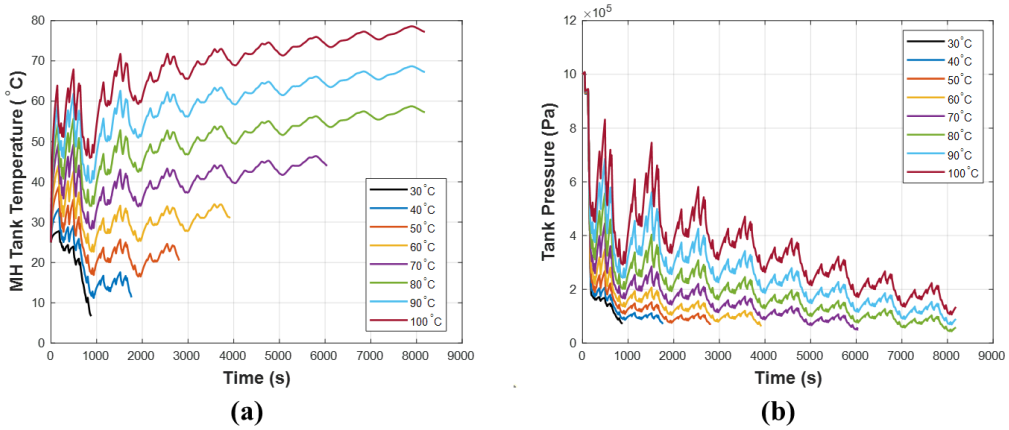

Figure 4.23 Under fixed tank number (3 tanks), different ambient temperatures, and 100 W/m^{2}K convection coefficient for Case-1 (a) MH tank temperatures and (b) tank pressure

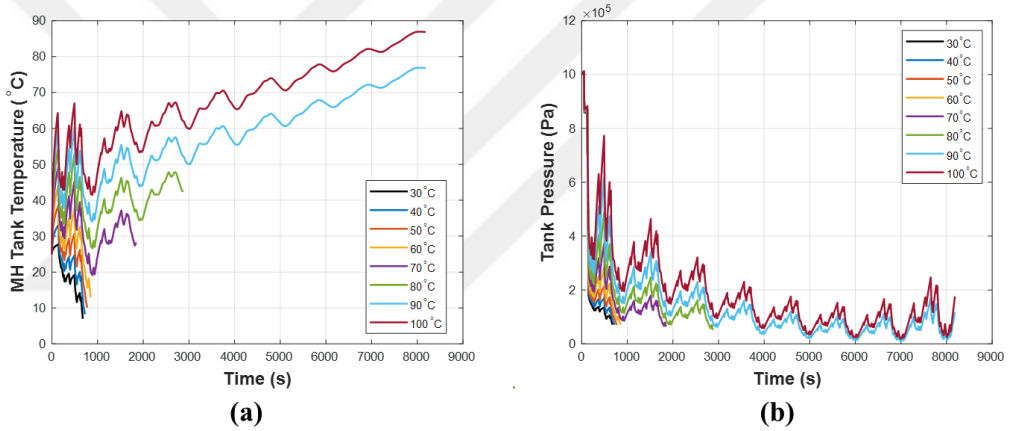

Figure 4.24 Under fixed tank number (3 tanks), different ambient temperatures, and 100 W/m^{2}K convection coefficient for Case-2 (a) MH tank temperatures and (b) tank pressure

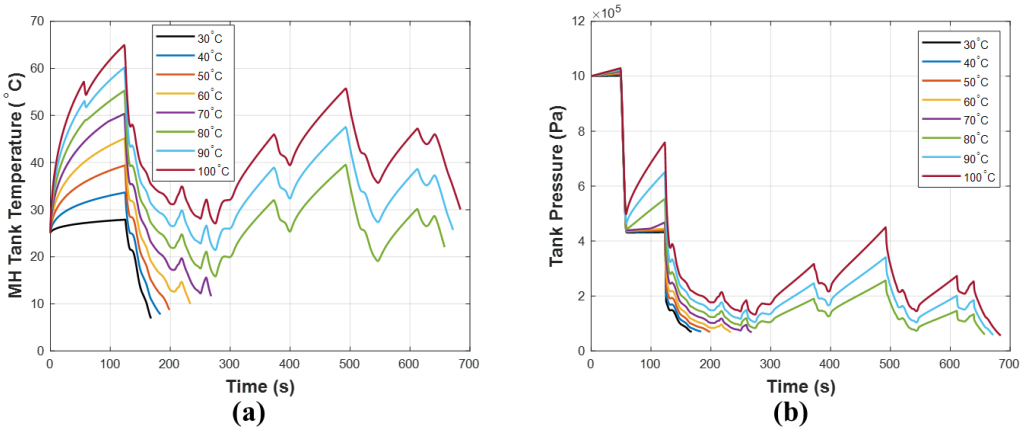

Figure 4.25 Under fixed tank number (3 tanks), different ambient temperatures, and 100 W/m^{2}K convection coefficient for Case-3 (a) MH tank temperatures and (b) tank pressure

In Figure 4.26 and Figure 4.27, the variation of tank temperatures and pressures under different ambient temperatures is shown for Case-4 and Case-5, respectively. Considering Figure 4.24 with Figure 4.26 and Figure 4.27, when examining each case separately as Case-2, Case-3, and Case-4, an increase in ambient temperature results in an increase in tank temperature, a decrease in the rate of decline in tank pressure, and consequently an increase in range. In Case-1, the average simulation duration was 800 seconds, but it showed a significant increase at an ambient temperature of 100 degrees, reaching 1800 seconds. In Case-2 and Case-3, the simulation duration reached 8000 seconds at high temperatures. The tank temperature in Case-3 reached a maximum of 100 degrees. Considering all cases together, the reduction in aspect ratio (width/height ratio) has increased the range. Simultaneously, the decrease in aspect ratio has caused an increase in tank temperature and a decrease in the rate of decline in tank pressure.

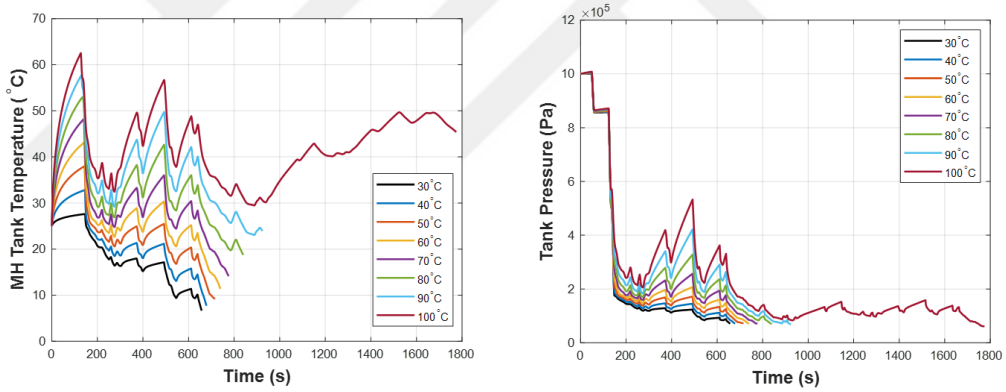

Figure 4.26 Under fixed tank number (3 tanks), different ambient temperatures, and a convection coefficient of 100 W/m^{2}K for Case-4 (a) MH tank temperatures and (a) tank pressure

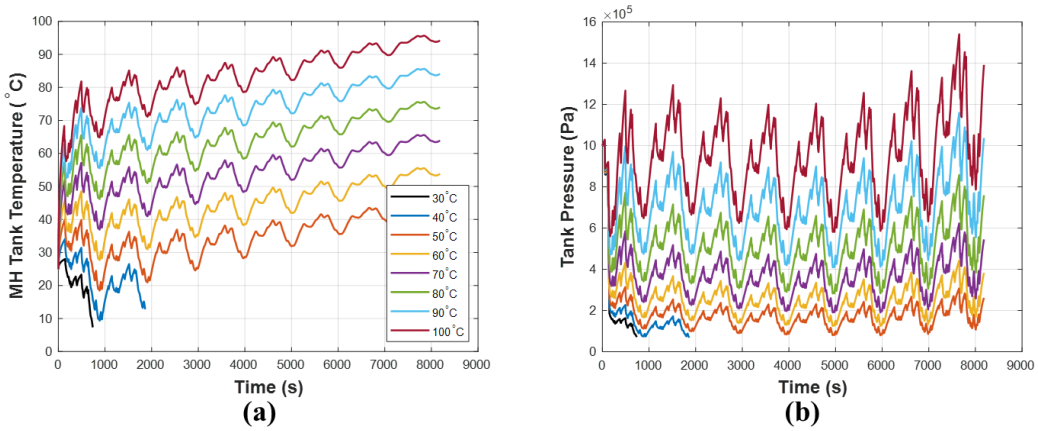

Figure 4.27 Under fixed tank number (3 tanks), different ambient temperatures, and a convection coefficient of 100 W/m^{2}K for Case-5 (a) MH tank temperatures and (a) tank pressure

4.2.3. Effect of Number of Tanks on Driving Durations

Figure 4.28 presents the results of analyses examining the effect of tank number on driving range. The analyses were conducted at 25°C ambient temperature, using Case-2 geometry, and a heat transfer coefficient of 10 W/m²K for 3, 6, 9, and 12 tanks. The simulation durations were observed to be approximately 600, 800, 1300, and 1750 seconds, respectively. Consequently, it can be seen that the simulation duration increased with the number of tanks, even though the increase was not significant.

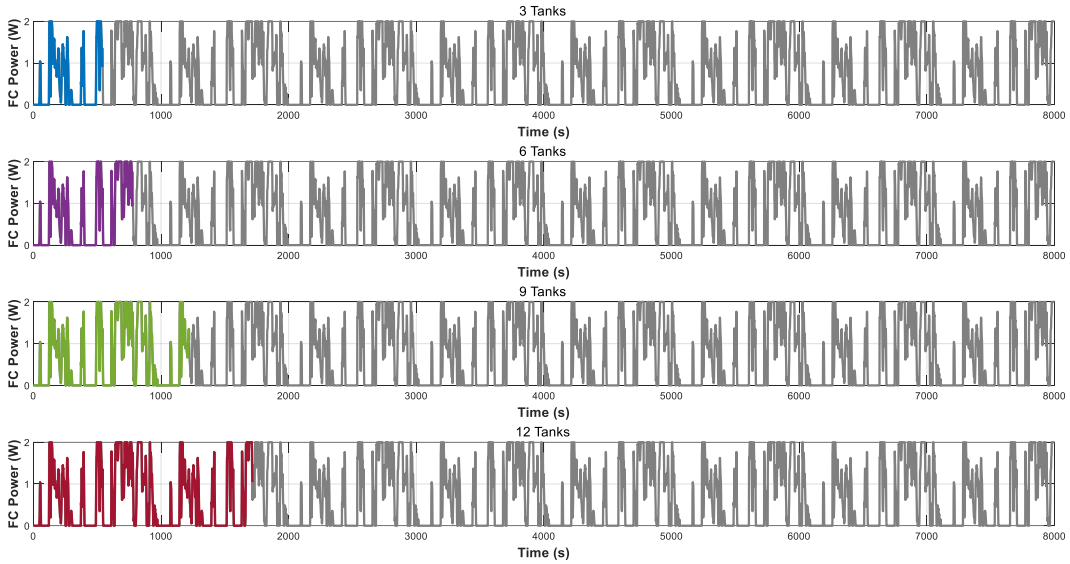

Figure 4.28 Driving duration under different tank numbers at Case-2 and 10 W/m^{2}K heat transfer coefficient

Figure 4.29 and Figure 4.30 depict analyses conducted again for Case-2, with heat transfer coefficients of 100 and 1000 W/m²K, respectively. In Figure 4.29, the analysis using 12 tanks completed the simulation duration of 8000 seconds. In Figure 4.30, where the convective heat transfer coefficient was increased, the simulation duration of 8000 seconds was completed with 9 tanks. These results indicate that an increase in the convective heat transfer coefficient led to an increase in the analysis duration.

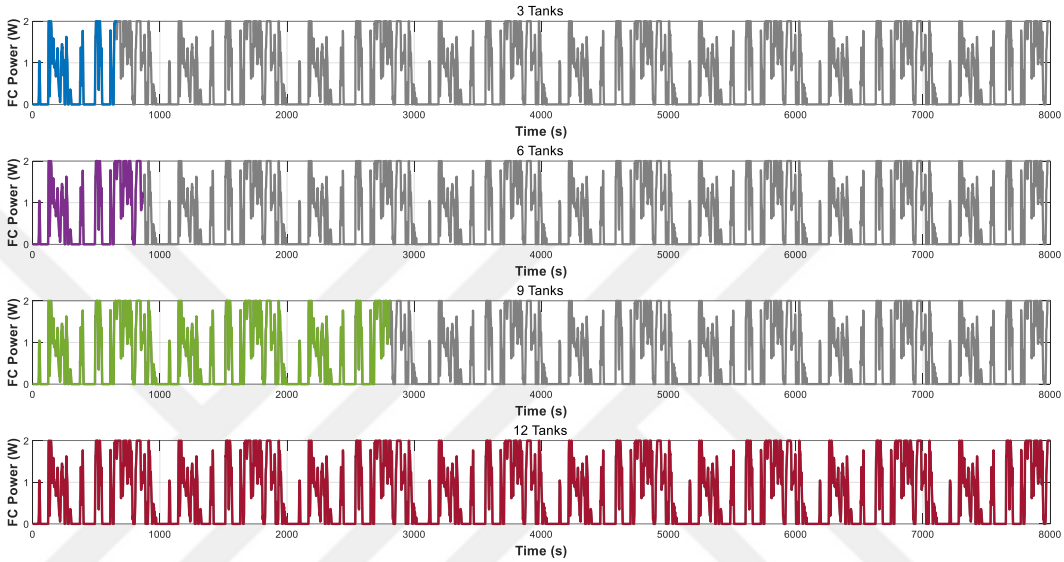

Figure 4.29 Driving duration under different tank numbers at Case-2 and 100 W/m²K heat transfer coefficient

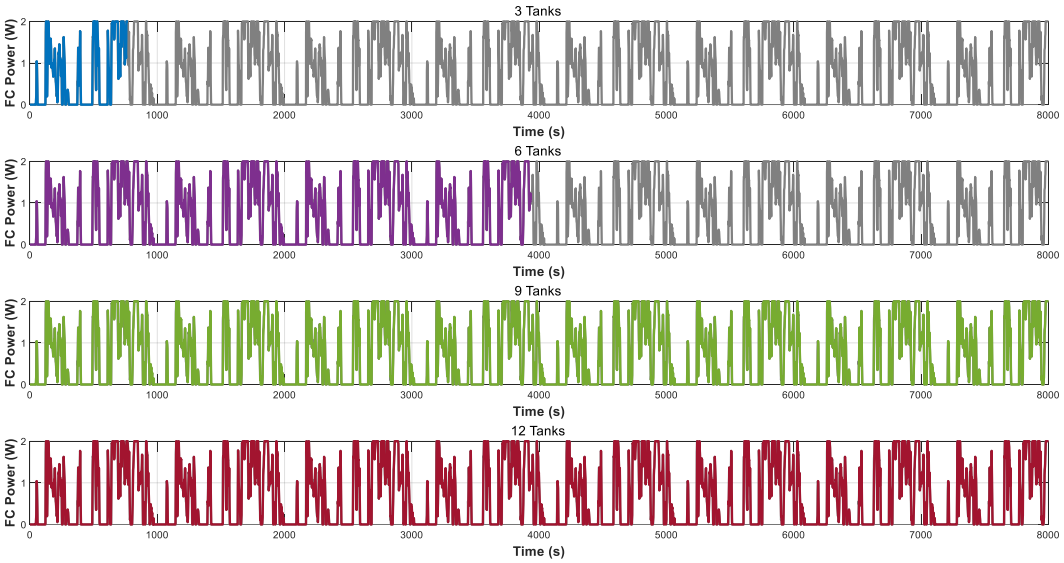

Figure 4.30 Driving duration under different tank numbers at Case-2 and 1000 W/m²K heat transfer coefficient

4.2.4. Effect of Fuel Cell Exhaust Heat

In this section, Scenario-1 and Scenario-2 were compared to examine the impact of directing the exhaust heat from the fuel cell to the tanks on the range. In Figure 4.31, the analysis was conducted at an ambient temperature of 25°C with nine tanks, and the geometry of Case-2 shows the increase in the range of Scenario-2. In Scenario-1, the simulation lasted approximately 1200 s, while in Scenario-2, it took about 1550 seconds. Examining the difference between the two scenarios, a discrepancy of 350 seconds can be observed. Consequently, it can be stated that the effect of directing the waste heat from the fuel cell to the tanks on the analysis time is not significant.

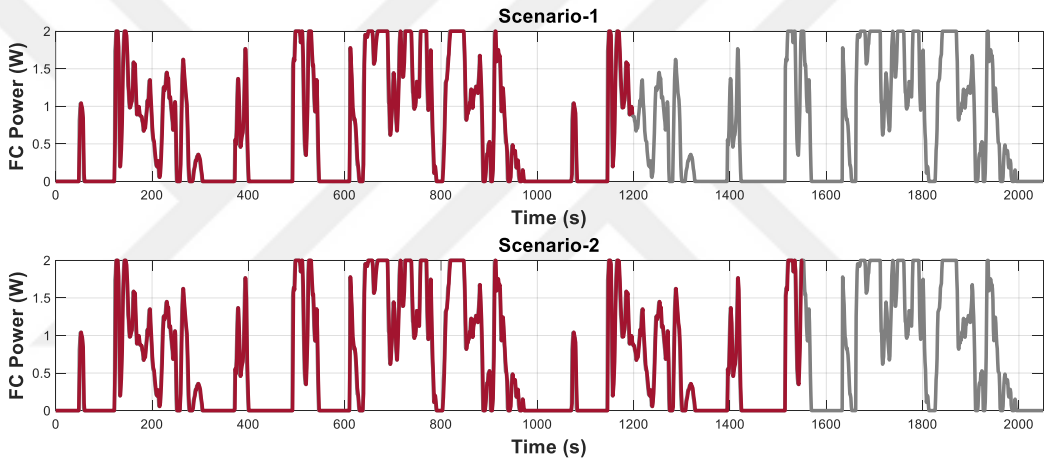

Figure 4.31 Comparative results between Scenario-1 and Scenario-2 at 25°C ambient temperature and 9 tanks

In Figure 4.32, the changes in tank temperature and tank pressure under the above conditions are given comparatively for Scenario-1 and Scenario-2. With the effect of the exhaust heat of the fuel cell, the tank temperature of Scenario-2 is higher than Scenario-1, and the rate of decrease in tank pressure of Scenario-2 is slower. In Scenario-2, the tank temperature reached approximately 27°C and remained at higher temperatures throughout the analysis compared to the ones achieved in Scenario-1. Although the rate of the tank pressure reaching 0.5 bar was slower in Scenario-2, the graph indicates that there is not much difference in pressure changes between Scenario-1 and Scenario-2.

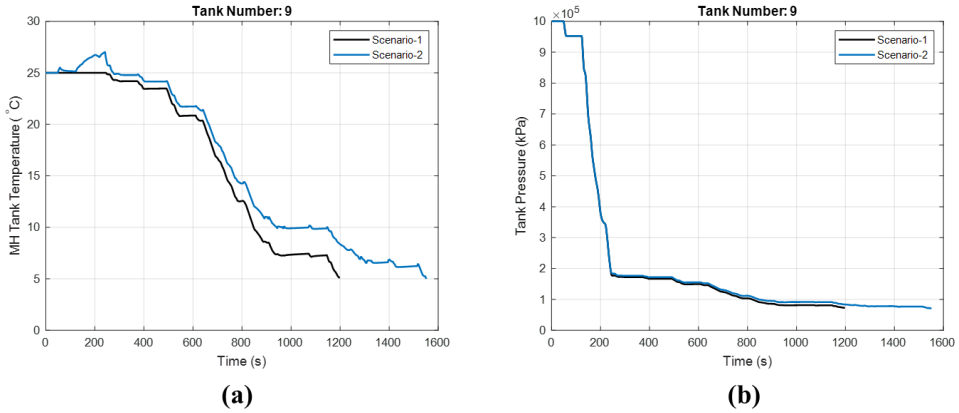

Figure 4.32 Comparative results between Scenario-1 and Scenario-2 (a) MH tank temperatures and (b) tank pressures at 25°C ambient temperature and 9 tanks

4.2.5. Effect of PID Temperature Controller and Different Air Set Temperature

In Figure 4.33 and Figure 4.34, the effect of air-set temperature changes on tank temperature and tank pressure can be observed at 25°C ambient temperature with 3 and 12 tanks, respectively. In general, an increase in air set temperature has led to an increase in tank temperature. The rate of decrease in tank pressure has decreased with an increase in air set temperature. In the analyses where 3 tanks were used, with the increase in air set temperature, the tank temperature reached a maximum of 30°C, and the analysis duration was approximately 650 s for all air set temperatures. There was no significant slowdown in the rate of decrease in tank pressure. In the analyses where 12 tanks were used, the increase in tank temperature approached 39°C. Unlike the analyses with 3 tanks, a significant increase in analysis duration from 2500 s to 8000 s was observed with the increase in air set temperature. A notable slowdown in the rate of decrease in tank pressure is evident in Figure 4.34. In this case, it is seen that, in addition to the effect of air set temperatures, the increase in the number of tanks also has a positive effect on the increase in analysis duration.

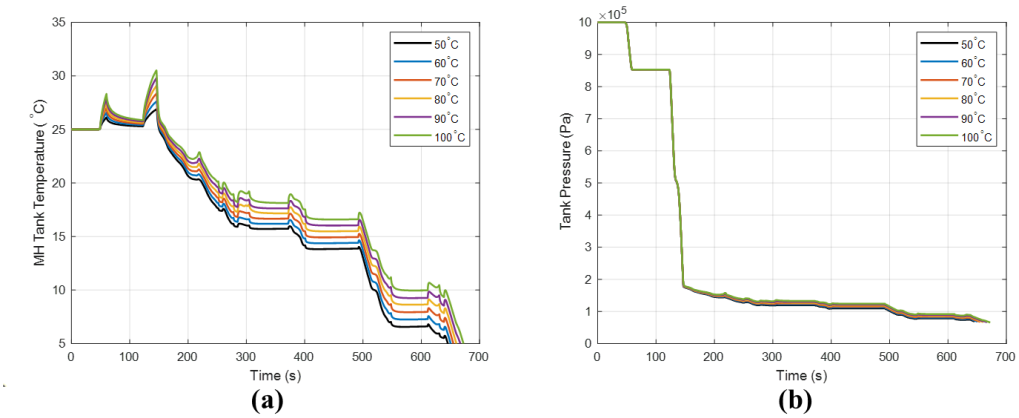

Figure 4.33 Change of (a) MH tank temperature and (b) tank pressure under different air set temperatures at 25°C ambient temperature and 3 tank number

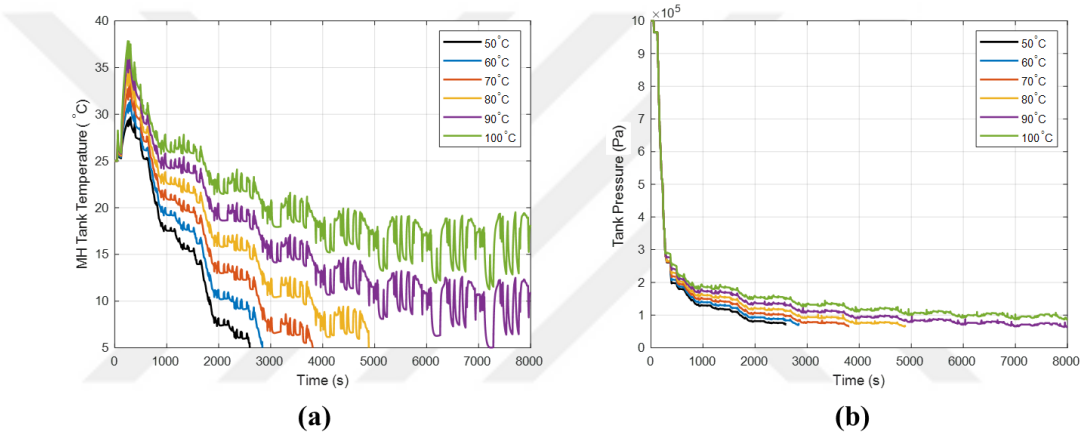

Figure 4.34 Change of (a) MH tank temperature and (b) tank pressure under different air set temperatures at 25°C ambient temperature and 12 tank number

Figure 4.35 shows the variations of the excess air expelled from the fuel cell cathode under a PID controller at different air set temperatures. The PID controller attempts to maintain the fuel cell exhaust air at set temperatures. As observed in the figure, the PID controller successfully keeps the exhaust air at the set temperatures with minor deviations.

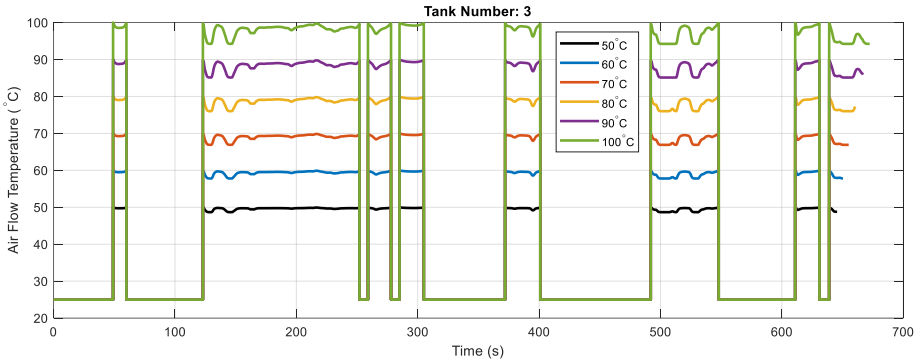

Figure 4.35 Changes of fuel cell exhaust air temperature with temperature controller under different air set temperatures and 3 tank numbers at 25°C ambient temperature

In Figure 4.36(a), the variation of fuel cell exhaust air under a PID controller set to 50°C is shown during the analysis period. In Figure 4.36(b), the change in the power required by the external heater to maintain the exhaust air of the fuel cell at 50°C is depicted during the analysis period. It is observed that the required power of the heater reaches up to 2 kW. In this case, a system using Scenario-2 would need to add a heater with a minimum power of 2 kW. This additional component would increase the vehicle weight and make it inefficient to add a 2 kW heater to a system that already uses a 2 kW fuel cell.

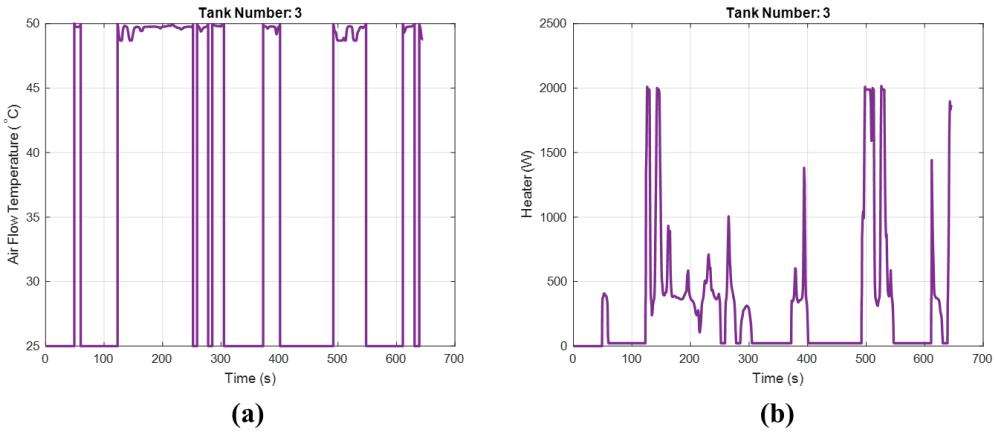

Figure 4.36 Under PID controller at air set temperature of 50°C and 3 number of tanks, (a) fuel cell exhaust air temperature and (b) power required by the heater (T_{amb}=25°C)

4.2.6. Comparisons of the Scenarios

The scenarios that were discussed in the second chapter and schematically shown in Figure 2.1 are compared in this section. The geometry of Case-2 is used for the comparison, and the number of tanks is set to 3. In Scenario-2 and Scenario-4, where the metal hydride tank is thermally coupled, the heat transfer coefficient of the air passing around the tanks is assumed to be 20 W/m²K when the fuel cell is operating and 5 W/m²K when it is not. The ambient temperature is taken as 25°C in Scenario-1 and Scenario-3. In Scenario-2 and Scenario-4, when the temperature controller is used, the air set temperature is 50°C; otherwise, it is assumed to be variable based on the temperature characteristics of the fuel cell. Table 4.5 provides the varying operating parameters for the scenarios.

Table 4.5 Operating parameters for different scenarios

Scenarios	**Scenario-1**	**Scenario-2**	**Scenario-2 *with PID***	**Scenario-3**	**Scenario-4**	**Scenario-4 *with PID***
Heat Transfer Coefficient [W/m^{2}K]	5	***When FC Power on*** 20 W/m^{2}K ***When FC Power off*** 5 W/m^{2}K	***When FC Power on*** 20 W/m^{2}K ***When FC Power off*** 5 W/m^{2}K	5	***When FC Power on*** 20 W/m^{2}K ***When FC Power off*** 5 W/m^{2}K	***When FC Power on*** 20 W/m^{2}K ***When FC Power off*** 5 W/m^{2}K
Ambient Temperature [°C]	25	Variable depends on FC Power	Air Set Temperature	25	Variable depends on FC Power	Air Set Temperature
H_2 Flow Controller	×	×	×	✓	✓	✓

It can be observed that hydrogen consumption significantly increases in scenarios where the hydrogen flow controller is used in Figure 4.37. In the scenarios, 5.75, 6.21, 6.54, 17.64, 21.4, and 24.65 grams of hydrogen were consumed, respectively. The figure shows almost no difference between Scenario-1 and Scenario-2, indicating that simply directing the air discharged from the fuel cell to the tanks does not significantly impact the system's range. In Scenario-2, there was an 8% increase in hydrogen

consumption compared to the amount consumed in Scenario-1. There is only a 5 percent increase in hydrogen consumption occurred when comparing Scenario-2 with and without the PID temperature controller. For these analyses, the air set temperature was assumed to be 50°C. Parametric analyses have shown that the system operates at higher air set temperatures for longer periods. However, since the increase in temperature would also raise the power needed by the external heater represented by the PID controller, using the PID controller in this scenario was not found to be efficient. When comparing Scenario-4 with Scenario-4 with PID, there is a 15% increase in hydrogen consumption, but it is not enough to significantly improve the system efficiency. In Scenario-4, there was a 272% increase in hydrogen consumption compared to Scenario-1. Figure 4.38 also compares the driving times of different scenarios and the driving durations of the scenarios are 536.43, 624.94, 645.55, 1213.14, 1555.71, and 1722.41 s, respectively. When comparing Scenario-1 and Scenario-2, a 16% difference is observed. Scenario-2 using PID shows a 20% increase compared to Scenario-1. There is not much increase in driving durations between Scenario-1, Scenario-2, and Scenario-2 with the temperature controller. The increase in driving durations of Scenario-4 and Scenario-4 with PID was 190% and 221%, respectively, compared to Scenario-1. Consistent with hydrogen consumption, scenarios with the hydrogen controller have longer driving times.

When looking at the percentage increases, the comparison between Scenario-1 and Scenario-2 shows that the 8% difference in hydrogen consumption is smaller than the 16% difference observed in driving time. Similarly, when comparing Scenario-1 and Scenario-4, there is a 272% increase in hydrogen consumption, whereas the difference in driving time is 190%. Although hydrogen consumption and driving time both exhibit a linear increase within themselves, the differences in these increases when compared may be due to the variable characteristic of the driving cycle.

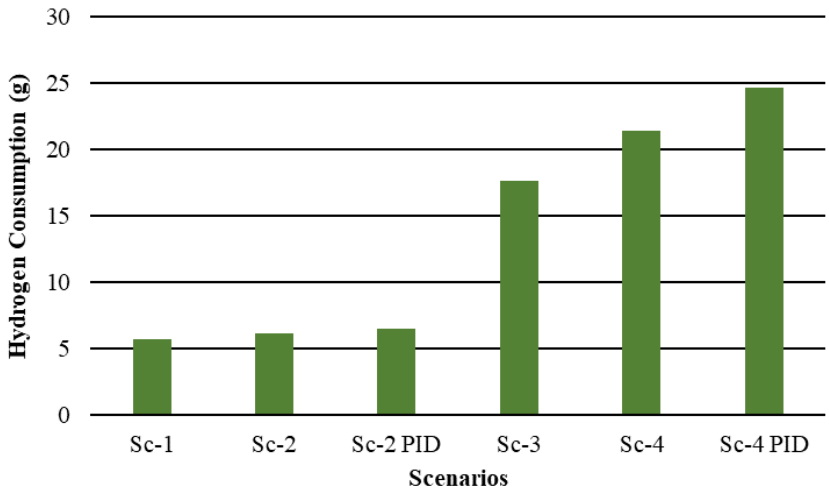

Figure 4.37 Comparison of the amounts of hydrogen used by different scenarios

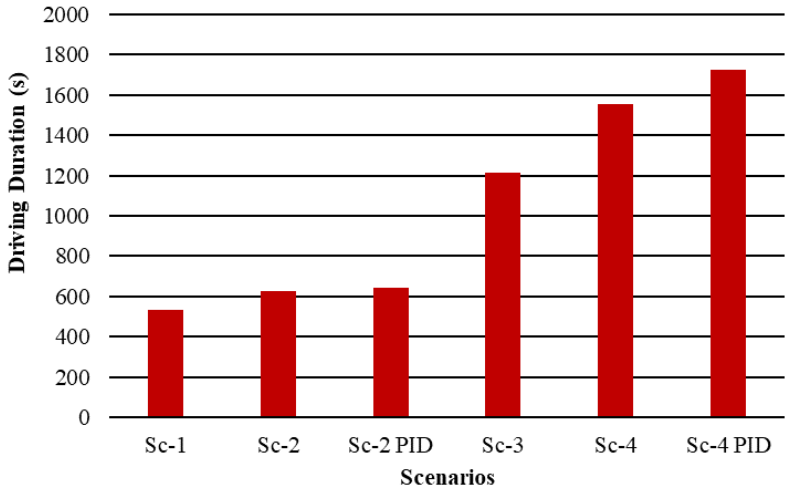

Figure 4.38 Comparison of driving durations of different scenarios

In Figure 4.39, the driving durations of Scenario-1, Scenario-2, Scenario-3, and Scenario-4 are given comparatively respectively. The reason for the small deviations in Scenario-3 and Scenario-4 is that the analyses were solved using the variable-time step solver. As seen in the figure, the analysis durations in Scenario-1 and Scenario-2 were approximately 550 and 620 s, respectively. The Scenario-3 analysis lasted about 1200 s, and Scenario-4 continued for 1550 s. While the results of Scenario-1 and Scenario-2 are very close to each other, there has been a significant increase in the durations of Scenario-3 and Scenario-4 with the effect of the hydrogen flow controller.

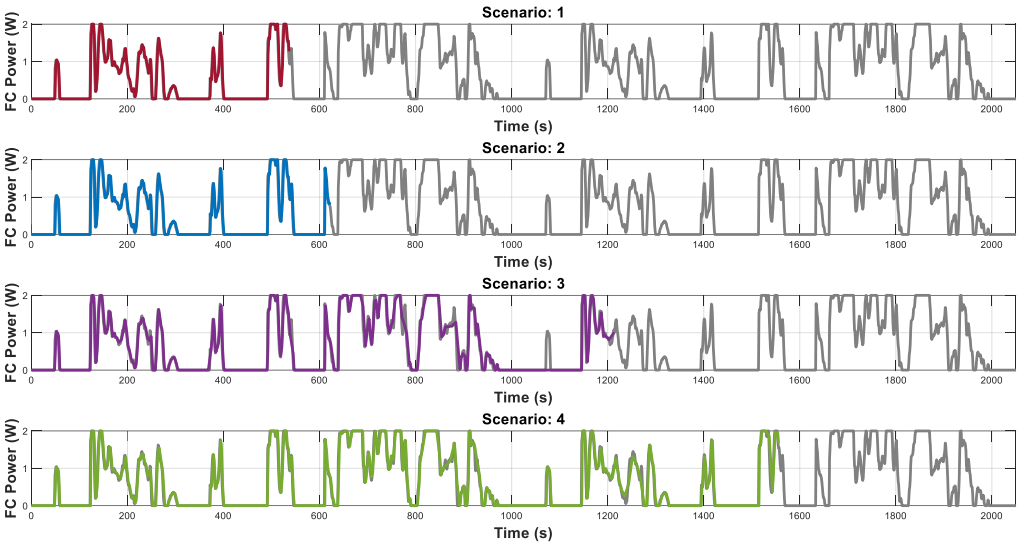

Figure 4.39 Comparison of driving durations for Sc-1, Sc-2, Sc-3, and Sc-4

CHAPTER FIVE
CONCLUSIONS

In this thesis, a 1D axisymmetric mathematical model for the MH tank was developed in MATLAB software and verified from literature data for the absorption and desorption process. In the case study for the MH/PCM tank system, to study the storage percentage and tank temperature of the MH tank, which stores hydrogen chemically, under passive thermal management, a PCM was wrapped around the outside of the model and mathematically modeled and parametric analyses were conducted. Paraffin was selected as the phase-changing material for $LaNi_5$. The optimum PCM thickness and melting temperature values are obtained using the Minitab program when the weight fraction and liquid fraction are maximum for different MH tank diameters and inlet pressure values. As a result, it is found that the weight fraction increases with the increase of the inlet pressure; on the contrary, the weight fraction decreases as the MH radius increases. Changing the inlet pressure and the MH radius does not specifically affect the liquid fraction.

In the second part of the thesis, a thermally coupled FC-MH tank system was developed to investigate system performance under various scenarios. Scenarios can be listed as Scenario-1 without thermal coupling and controller, Scenario-2 with thermal coupling and without a controller, Scenario-3 without thermal coupling and with controller, and Scenario-4 with thermal coupling and controller. The mathematical model of the MH tank system was re-modeled in the Simulink environment, with the fuel cell required to produce power as input to the system. The power characteristics of the fuel cell were based on its use in a lightweight hybrid vehicle with battery-fuel cell integration, utilizing a specific driving cycle. A model was created and validated against the literature to determine the exhaust air temperature at the fuel cell's cathode outlet. To maintain the exhaust air temperature at a specified level, a temperature controller was designed using a PID block in Simulink. This temperature controller represents an external heater added to the system that heats the fuel cell's exhaust air. Finally, an algorithm was developed for the hydrogen flow controller to ensure sequential operation of the tanks. Using these models, parametric analyses were conducted under different scenarios (Case-1, Case-

2, Case-3, Case-4, & Case-5). Subsequently, these scenarios were compared against each other. The results obtained can be summarized as follows:

- As a result of parametric analyses, it can be stated that an increase in the convective heat transfer coefficient around the tanks leads to an increase in analysis time and tank temperature. At the same time, the rate of pressure drop in the tank slows down. Parametric analyses conducted under different ambient temperatures indicate that as ambient temperature increases, there is an increase in analysis time and tank temperature. However, excessive temperature increases under optimal operating conditions can potentially damage the tank material. The rate of pressure drop in the tank also slows down with increasing ambient temperature.
- Analysis conducted at constant tank height and varying tank diameters reveals that when the stored hydrogen quantity remains constant, a decrease in tank diameter increases analysis time and tank temperature. Additionally, the rate of pressure drop in the tank decreases as the tank diameter decreases.
- At the constant tank height and with varying tank diameters while keeping the number of tanks constant, analyses show that as the tank diameter decreases, there is a corresponding decrease in tank volume and, thus stored hydrogen quantity. This reduction negatively impacts analysis time and tank temperature.
- Analyses conducted by varying the aspect ratio show that scenarios with smaller tank diameters result in longer analysis times. When comparing these scenarios, it is observed that tanks with smaller diameters heat up more quickly compared to tanks with larger diameters. Furthermore, using multiple smaller-diameter tanks has been found to be more efficient in these analyses.
- Analysis comparing all scenarios indicates that directing only the exhaust heat from the fuel cell to the tanks is not sufficient to increase the analysis time significantly.
- In Scenario-2 where the temperature controller is added, analyses conducted under different ambient temperatures show that as the ambient temperature increases, there is an increase in analysis time and tank temperature, along with a decrease in the rate of pressure drop in the tank. However, it has been observed that the temperature controller has minimal effect at lower ambient temperatures. Additionally, adding an external heater to the system would increase vehicle weight

and require more power than what the fuel cell generates. Therefore, using an external heater as the temperature controller was not found to be efficient for this system.

- Analysis comparing all scenarios reveals that Scenario-3 and Scenario-4, where the hydrogen flow controller is used, are significantly more efficient than the other scenarios. There is nearly no difference in analysis times between Scenario-1 and Scenario-2, while Scenario-3 and Scenario-4 show a much greater difference compared to Scenario-1 and Scenario-2. A 272% increase in hydrogen consumption was observed in Scenario-4 compared to Scenario-1. This highlights the impact of directing the fuel cell's exhaust air to the tanks using the hydrogen flow controller.

Considering all these results, in the design of a thermally integrated FC-MH system, alternatives such as directing the exhaust heat from the fuel cell first to a liquid coolant and then transferring it to the tanks or employing passive thermal management methods on the tanks to enhance heat transfer can be evaluated rather than directly routing the exhaust heat to the tanks. These approaches can potentially increase heat transfer efficiency, optimize system weight, and address power requirements. Each method should be assessed based on its advantages and disadvantages to ensure the design achieves optimal performance, reliability, and cost-effectiveness. The metal material used in the thesis is not a commercial material. Analyses should be performed with commercially used metals to examine the usability of the system.

In the future, a case study will be conducted for both absorption and desorption processes to select suitable PCM materials for the tanks in the system. Instead of PCM, fin usage will be incorporated into the model for performance analyses of the tanks. The efficiency of scenarios for the FC-MH tank system will be calculated and compared, and various scenarios created using different passive thermal management methods will be compared. An algorithm for the hydrogen flow controller will be developed to increase its efficiency.

REFERENCES

Aceves SM, Espinosa-Loza F, Ledesma-Orozco E, Ross TO, Weisberg AH, Brunner TC, vd. (2010). High-density automotive hydrogen storage with cryogenic capable pressure vessels. *International Journal of Hydrogen Energy*, 35, 1219–26.

Afzal M, Sharma N, Gupta N, Sharma P. (2022). Transient simulation studies on a metal hydride based hydrogen storage reactor with longitudinal fins. *Journal of Energy Storage*, 51, 104426.

Afzal M, Sharma P. (2021). Design and computational analysis of a metal hydride hydrogen storage system with hexagonal honeycomb based heat transfer enhancements-part A. *International Journal of Hydrogen Energy*, 46, 13116–30.

Ahluwalia R. (2007). Sodium alanate hydrogen storage system for automotive fuel cells. *International Journal of Hydrogen Energy*, 32, 1251–61.

Ahluwalia RK, Peng JK. (2009). Automotive hydrogen storage system using cryo-adsorption on activated carbon. *International Journal of Hydrogen Energy*, 34, 5476–87.

Ahluwalia RK, Peng JK. (2008). Dynamics of cryogenic hydrogen storage in insulated pressure vessels for automotive applications. *International Journal of Hydrogen Energy*, 33, 4622–33.

Alqahtani T, Bamasag A, Mellouli S, Askri F, Phelan PE. (2020). Cyclic behaviors of a novel design of a metal hydride reactor encircled by cascaded phase change materials. *International Journal of Hydrogen Energy*, 45, 32285–97.

Askri F, Bensalah M, Jemni A, Bennasrallah S. (2009). Optimization of hydrogen storage in metal-hydride tanks. *International Journal of Hydrogen Energy*, 34, 897–905.

Bai X-S, Yang W-W, Tang X-Y, Dai Z-Q, Yang F-S. (2022). Parametric optimization of coupled fin-metal foam metal hydride bed towards enhanced hydrogen

absorption performance of metal hydride hydrogen storage device. *Energy*, 243, 123044.

Bai X-S, Yang W-W, Tang X-Y, Yang F-S, Jiao Y-H, Yang Y. (2021). Optimization of tree-shaped fin structures towards enhanced absorption performance of metal hydride hydrogen storage device: A numerical study. *Energy*, 220, 119738.

Bai X-S, Yang W-W, Zhang W-Y, Yang F-S, Tang X-Y. (2020). Hydrogen absorption performance of a novel cylindrical MH reactor with combined loop-type finned tube and cooling jacket heat exchanger. *International Journal of Hydrogen Energy*, 45, 28100–15.

Borzenko V, Eronin A. (2016). The use of air as heating agent in hydrogen metal hydride storage coupled with PEM fuel cell. *International Journal of Hydrogen Energy*, 41, 23120–4.

Busqué R, Torres R, Grau J, Roda V, Husar A. (2017). Effect of metal hydride properties in hydrogen absorption through 2D-axisymmetric modeling and experimental testing in storage canisters. *International Journal of Hydrogen Energy*, 42, 19114–25.

Bvumbe TJ, Bujlo P, Tolj I, Mouton K, Swart G, Pasupathi S, vd. (2016). Review on management, mechanisms and modelling of thermal processes in PEMFC. *Hydrogen and Fuel Cells*, 1, 1–20.

Bénard P, Chahine R. (2001). Modeling of adsorption storage of hydrogen on activated carbons. *International Journal of Non-Linear Mechanics*, 36, 849–55.

Cano, M. H., Kelouwani, S., Agbossou, K., & Dubé, Y. (2014). Free air breathing proton exchange membrane fuel cell: Thermal behavior characterization near freezing temperature. *Journal of Power Sources,* 246, 650-658.

Cengel, Y., & Ghajar, A. (2015). Heat and Mass Transfer (Fifth Edit). McGraw-Hill Education.

Chabane D, Ibrahim M, Harel F, Djerdir A, Candusso D, Elkedim O. (2019). Energy management of a thermally coupled fuel cell system and metal hydride tank. *International Journal of Hydrogen Energy*, 44, 27553–63.

Colpan CO, Nalbant Y, Ercelik M. (2018). *Fundamentals of Fuel Cell Technologies* (1107–30). Comprehensive Energy Systems, Elsevier.

Corgnale C, Hardy B, Chahine R, Cossement D. (2018). Hydrogen desorption using honeycomb finned heat exchangers integrated in adsorbent storage systems. *Applied Energy*, 213, 426–34.

Da Rosa A V., Ordóñez JC. (2021). *Fundamentals of Renewable Energy Processes* (Fourth) (478–94). Katey Birtcher: Academic Press.

Davids MW, Tolj I, Jao T-C, Lototskyy M, Pasupathi S, Sita C. (2016). Development of a Portable Polymer Electrolyte Membrane Fuel Cell System Using Metal Hydride as the Hydrogen Storage Medium. *ECS Transactions*, 75, 553–62.

Delhomme B, Lanzini A, Ortigoza-Villalba GA, Nachev S, de Rango P, Santarelli M, vd. (2013). Coupling and thermal integration of a solid oxide fuel cell with a magnesium hydride tank. *International Journal of Hydrogen Energy*, 38, 4740–7.

Dieterich M, Pohlmann C, Bürger I, Linder M, Röntzsch L. (2015). Long-term cycle stability of metal hydride-graphite composites. *International Journal of Hydrogen Energy*, 40, 16375–82.

Dincer, I., & Ezan, M. A. (2018). *Heat Storage: A Unique Solution For Energy Systems*. Springer International Publishing.

Dincer, I., Ezan, M.A., (2023), *Alternatif Enerji Kaynakları ve Doğalgaz Lojistiği Raporu* (49-65). Ankara: Türkiye Bilimler Akademisi.

El Mghari H, Huot J, Tong L, Xiao J. (2020). Selection of phase change materials, metal foams and geometries for improving metal hydride performance. *International Journal of Hydrogen Energy*, 45, 14922–39.

El Mghari H, Huot J, Xiao J. (2019). Analysis of hydrogen storage performance of metal hydride reactor with phase change materials. International Journal of Hydrogen *Energy*, 44, 28893–908.

Ferekh S, Gwak G, Kyoung S, Kang H, Chang M, Yun S, vd. (2015). Numerical comparison of heat-fin- and metal-foam-based hydrogen storage beds during hydrogen charging process. *International Journal of Hydrogen Energy*, 40, 14540–50.

Førde T, Eriksen J, Pettersen AG, Vie PJS, Ulleberg Ø. (2009). Thermal integration of a metal hydride storage unit and a PEM fuel cell stack. *International Journal of Hydrogen Energy*, 34, 6730–9.

Galli S, De Francesco M, Monteleone G, Oronzio R, Pozio A. (2010). Development of a compact hydrogen generator from sodium borohydride. *International Journal of Hydrogen Energy*, 35, 7344–9.

Giap V-T, Lee YD, Kim YS, Ahn KY. (2020). A novel electrical energy storage system based on a reversible solid oxide fuel cell coupled with metal hydrides and waste steam. *Applied Energy*, 262, 114522.

Gonzatti F, Nizolli V, Ferrigolo FZ, Farret FA, de Mello MAS. (2016). Experimental Hydrogen Plant with Metal Hydrides to Store and Generate Electrical Power. *International Journal of Emerging Electric Power Systems*, 17, 59–67.

Gupta S, Sharma VK. (2021). Design and analysis of metal hydride reactor embedded with internal copper fins and external water cooling. *International Journal of Energy Research*, 45, 1836–56.

Hassan, I. A., Ramadan, H. S., Saleh, M. A., & Hissel, D. (2021). Hydrogen Storage Technologies For Stationary And Mobile Applications: Review, Analysis And Perspectives. *Renewable And Sustainable Energy Reviews*, 149, 111311

Horizon Educational-H2000. (2024). *H-2000 PEM Fuel Cell - 2kW*. Retrieved July 13, 2024, from https://www.horizoneducational.com/h-2000-pem-fuel-cell-2kw/p1357

Horizon Educational-H100XP. (2024). *H-1000XP PEM Fuel Cell - 1kW.* Retrieved *July 13, 2024, from https://www.horizoneducational.com/h-1000-xp-fuel-cell-stack/p1407*

H2Planet. (2024). *MyH2 900.* Retrieved July 13, 2024, from https://www.h2planet.eu/en/detail/MyH2900

Ishaq, H., Dincer, I., & Crawford, C. (2022). A review on hydrogen production and utilization: Challenges and opportunities. *International Journal of Hydrogen Energy*, 47(62), 26238-26264.

Johnson TA, Jorgensen SW, Dedrick DE. (2011). Performance of a full-scale hydrogen-storage tank based on complex hydrides. *Faraday Discussions*, 151, 327.

Karmakar A, Mallik A, Gupta N, Sharma P. (2020). ScienceDirect Studies on 10kg alloy mass metal hydride based reactor for hydrogen storage. *International Journal of Hydrogen Energy*, 46, 5495–506.

Krishna KV, Pandey V, Maiya MP. (2022). Bio-inspired leaf-vein type fins for performance enhancement of metal hydride reactors. *International Journal of Hydrogen Energy*, 47, 23694–709.

Kumar K, Alam M, Rakshit D, Dutta V. (2019). Operational characteristics of metal hydride energy storage system in microgrid. *Energy Conversion and Management*, 187, 176–90.

Kumar S, Raju M, Senthil Kumar V. (2012). System simulation models for on-board hydrogen storage systems. *International Journal of Hydrogen Energy*, 37 , 2862–73.

Lewis SD, Chippar P. (2021). Analysis of Heat and Mass Transfer During Charging and Discharging in a Metal Hydride - Phase Change Material Reactor. *Journal of Energy Storage*, 33, 102108.

Ley M, Meggouh M, Moury R, Peinecke K, (2015). Felderhoff M. Development of Hydrogen Storage Tank Systems Based on Complex Metal Hydrides. *Materials*, 8, 5891–921.

Liu Z, Li Y, Bu Q, Guzy CJ, Li Q, Chen W, vd. (2016). Novel fuel cell stack with coupled metal hydride containers. *Journal of Power Sources*, 328, 329–35.

Lozano GA, Eigen N, Keller C, Dornheim M, Bormann R. (2009). Effects of heat transfer on the sorption kinetics of complex hydride reacting systems. *International Journal of Hydrogen Energy*, 34, 1896–903.

MacDonald BD, Rowe AM. (2006). A thermally coupled metal hydride hydrogen storage and fuel cell system. Journal of Power Sources, 161, 346–55.

Mellouli S, Askri F, Abhilash E, Ben Nasrallah S. (2017). Impact of using a heat transfer fluid pipe in a metal hydride-phase change material tank. *Applied Thermal Engineering*, 113, 554–65.

Minko KB, Artemov VI, Yan'kov GG. (2015). Numerical study of hydrogen purification using metal hydride reactor with aluminium foam. *Applied Thermal Engineering*, 76, 175–84.

Nasrallah, S. (1997). Heat and mass transfer models in metal-hydrogen reactor. International Journal of Hydrogen Energy, 22(1), 67–76.

Nguyen HQ, Shabani B. (2020). Proton exchange membrane fuel cells heat recovery opportunities for combined heating/cooling and power applications. *Energy Conversion and Management*, 204, 112328.

Nguyen HQ, Shabani B. (2021). Review of metal hydride hydrogen storage thermal management for use in the fuel cell systems. *International Journal of Hydrogen Energy*, 46, 31699–726.

Nyamsi SN, Yang F, Zhang Z. (2012). An optimization study on the finned tube heat exchanger used in hydride hydrogen storage system – analytical method and numerical simulation. *International Journal of Hydrogen Energy*, 37, 16078–92.

Omrani R, Nguyen HQ, Shabani B. (2020). Thermal coupling of an open-cathode proton exchange membrane fuel cell with metal hydride canisters: An experimental study. *International Journal of Hydrogen Energy*, 45, 28940–50.

Pourpoint TL, Velagapudi V, Mudawar I, Zheng Y, Fisher TS. (2010). Active cooling of a metal hydride system for hydrogen storage. *International Journal of Heat and Mass Transfer*, 53, 1326–32.

Rabienataj Darzi A., Hassanzadeh Afrouzi H, Alizadeh E, Shokri V, Farhadi M. (2017). Numerical Simulation of Heat and Mass Transfer during Absorption of Hydrogen in Metal Hydride Tank. *Heat Transfer-Asian Research*, 46, 75–90.

Raju M, Khaitan S. (2011) Charging dynamics of metal hydride hydrogen storage bed for small wind hybrid systems. *International Journal of Hydrogen Energy*, 36, 10797–807.

Raju M, Kumar S. (2012). Optimization of heat exchanger designs in metal hydride based hydrogen storage systems. *International Journal of Hydrogen Energy*, 37, 2767–78.

Raju M, Kumar S. (2011). System simulation modeling and heat transfer in sodium alanate based hydrogen storage systems. *International Journal of Hydrogen Energy*, 36, 1578–91.

Shabani B, Andrews J. (2011). An experimental investigation of a PEM fuel cell to supply both heat and power in a solar-hydrogen RAPS system. *International Journal of Hydrogen Energy*, 36, 5442–52.

Shao H. (2017). Heat Modeling and Material Development of Mg-Based Nanomaterials Combined with Solid Oxide Fuel Cell for Stationary Energy Storage. *Energies*, 10, 1767.

Singh A, Maiya MP, Srinivasa Murthy S. (2017). Experiments on solid state hydrogen storage device with a finned tube heat exchanger. *International Journal of Hydrogen Energy*, 42, 15226–35.

Tetuko AP, Shabani B, Andrews J. (2016). Thermal coupling of PEM fuel cell and metal hydride hydrogen storage using heat pipes. *International Journal of Hydrogen Energy*, 41, 4264–77.

Tetuko AP, Shabani B, Omrani R, Paul B, Andrews J. (2018). Study of a thermal bridging approach using heat pipes for simultaneous fuel cell cooling and metal hydride hydrogen discharge rate enhancement. *Journal of Power Sources*, 397, 177–88.

Tong L, Xiao J, Yang T, Bénard P, Chahine R. (2019). Complete and reduced models for metal hydride reactor with coiled-tube heat exchanger. *International Journal of Hydrogen Energy*, 44, 15907–16.

Tong L, Yuan Y, Yang T, Bénard P, Yuan C, Xiao J. (2021). Hydrogen release from a metal hydride tank with phase change material jacket and coiled-tube heat exchanger. *International Journal of Hydrogen Energy*, 46, 32135–48.

Urbanczyk R, Peil S, Bathen D, Heßke C, Burfeind J, Hauschild K, vd. (2011). HT-PEM Fuel Cell System with Integrated Complex Metal Hydride Storage Tank. *Fuel Cells*, 11, 911–20.

Urunkar RU, Patil SD. (2021). Enhancement of heat and mass transfer characteristics of metal hydride reactor for hydrogen storage using various nanofluids. *International Journal of Hydrogen Energy*, 46, 19486–97.

Valenti G. (2016). Hydrogen liquefaction and liquid hydrogen storage. *Compendium of Hydrogen Energy* ,27–51.

Woodfield PL, Monde M, Takano T. (2008). Heat Transfer Characteristics for Practical Hydrogen Pressure Vessels Being Filled at High Pressure. *Journal of Thermal Science and Technology*, 3, 241–53.

Yao J, Zhu P, Guo L, Duan L, Zhang Z, Kurko S, vd. (2020). A continuous hydrogen absorption/desorption model for metal hydride reactor coupled with PCM as heat management and its application in the fuel cell power system. *International Journal of Hydrogen Energy*, 45, 28087–99.

Yiotis AG, Kainourgiakis ME, Kosmidis LI, Charalambopoulou GC, Stubos AK. (2014). Thermal coupling potential of Solid Oxide Fuel Cells with metal hydride tanks: Thermodynamic and design considerations towards integrated systems. *Journal of Power Sources*, 269, 440–50.

Yue, M., Lambert, H., Pahon, E., Roche, R., Jemei, S., & Hissel, D. (2021). Hydrogen energy systems: A critical review of technologies, applications, trends and challenges. *Renewable and Sustainable Energy Reviews*, 146, 111180.

Zhu D, Ait-Amirat Y, N'Diaye A, Djerdir A. (2019). Active thermal management between proton exchange membrane fuel cell and metal hydride hydrogen storage tank considering long-term operation. *Energy Conversion and Management*, 202, 112187.

Zhu Z, Bao Z, Wu D. (2022). Optimization of the content distribution of expanded natural graphite in a multilayer metal hydride bed for thermochemical heat storage. *Applied Thermal Engineering*, 216, 119115.

APPENDICES

Appendix-1: Nomenclature

Symbols	Name	Unit
A	Plateau Pressure Coefficient	[-]
B	Plateau Pressure Coefficient	[K^{-1}]
C	Volumetric Heat Capacity	[J m^{-3} K^{-1}]
C_a	Reaction Constant for Absorption	[s^{-1}]
C_d	Reaction Constant for Desorption	[s^{-1}]
c_p	Specific Heat	[kJ kg^{-1} K^{-1}]
E	Activation Energy	[J mol^{-1}]
F	Faraday Constant	[C mol^{-1}]
F_{cyl}	Correction Factor	[-]
h	Convective heat transfer Coefficient	[W m^{-2} K^{-1}]
I	Current	[A]
k	Thermal Conductivity	[W m^{-1} K^{-1}]
L_c	Characteristic Length	[m]
$\dot{m}$	Mass Flow Rate	[kg s^{-1}]
MW	Molar Weight	[g mol^{-1}]
$\dot{n}$	Molar Flow Rate	[mol s^{-1}]
P	Pressure	[Pa]
Pr	The Prandtl Number	[-]
$\dot{Q}$	Heat Tranfer Rate	[W]
$\dot{q}_{source}$	Heat Source from a Chemical Reaction	[W m^{-3}]
R	Universal Gas Constant	[kJ $kmol^{-1}$ K^{-1}]
r	Radial Coordinates	[m]
Ra	The Rayleigh Number	[-]
T	Temperature	[K]
t	Time	[s]
V	Voltage	[V]
wt	Weight Fraction	[-]

x	Stoichiometric Ratio	[-]

Greek Letters

α	The Thermal Diffusivity	[m^2 s^{-1}]
β	Thermal Expansion Coefficient	[K^{-1}]
ε	Porosity	[-]
η	Efficiency	[-]
ϑ	Kinematic Viscosity	[m^2 s^{-1}]
μ	Dynamic Viscosity	[Pa s^{-1}]
ρ	Density	[kg m^{-3}]
δT_m	Mushy Range	[K]
ΔH^0	Enthalpy of Formation	[kJ kg^{-1}]

Letter-like Symbols

$\dot{\forall}$	Volumetric Flow Rate	[m^3 s^{-1}]

Subtitles

a	Absorption
amb	Ambient
air	Air
air, set	Air Set
$cell$	Cell
d	Desorption
eff	Effective
$empty$	Empty Phase
en	Enhanced
eq	Equilibrium
gas	Gas Phase
$heater$	Heater
m	Melting Phase of PCM
out	Outlet
$solid$	Solid Phase

$source$	Source Term
ss	Saturated State
ref	Reference
$water$	Water Phase
H_2	Hydrogen
H_2O	Water
N_2	Nitrogen
O_2	Oxygen

Upper Titles

$cathode$	Cathode Side of Fuel Cell
sat	Saturated
$waste$	Waste

Abbreviations

AFC	Alkaline Fuel Cell
DMFC	Direct Methanol Fuel Cell
FC	Fuel Cell
HHV	Higher Heating Value
LHV	Lower Heating Value
MCFC	Molten Carbonate Fuel Cell
MH	Metal Hydride
PAFC	Phosphoric Acid Fuel Cell
PCM	Phase Change Material
PEMFC	Proton Exchange Membrane Fuel Cell
SOFC	Solid Oxide Fuel Cell